

OPTICAL MANIPULATION AND IMAGING OF ASSEMBLIES OF TOPOLOGICAL  
DEFECTS AND COLLOIDS IN LIQUID CRYSTALS

by

RAHUL P. TRIVEDI

B.E., Bombay University, India, 2005

M.S., University of Colorado at Boulder, 2007

A thesis submitted to the

Faculty of the Graduate School of the

University of Colorado in partial fulfillment

of the requirement for the degree of

Doctor of Philosophy

Department of Electrical, Computer, and Energy Engineering

2012

This thesis entitled:

Optical Manipulation and Imaging of Assemblies of Topological Defects and Colloids  
in Liquid Crystals

written by Rahul P. Trivedi

has been approved for the Department of Electrical, Computer, and Energy  
Engineering

---

Ivan I. Smalyukh

---

Noel A. Clark

---

Wounjhang Park

---

Rafael Piestun

---

David M. Walba

Date \_\_\_\_\_

The final copy of this thesis has been examined by the signatories, and we find that both the content and the form meet acceptable presentation standards of scholarly work in the above mentioned discipline.

Trivedi, Rahul P. (Ph.D., Electrical, Computer, and Energy Engineering)

Optical Manipulation and Imaging of Assemblies of Topological Defects and Colloids in Liquid Crystals.

Thesis directed by Assistant Professor Ivan I. Smalyukh

Liquid Crystals (LCs) have proven to be important for electro-optic device applications such as displays, spatial light modulators, non-mechanical beam-steerers, etc. Owing to their unique mechanical, electrical, and optical properties, they are also being explored for wide array of advanced technological applications such as biosensors, tunable lenses, distributed feedback lasers, muscle-like actuators, etc. The thesis explores LC media from the standpoint of controlling their elastic and optical properties by generating and manipulating assemblies of defects and colloidal particles. To achieve the goal of optically manipulating these configurations comprising defects and particles at microscale with an unprecedented control, and then to visualize the resultant molecular director patterns, requires development of powerful optical system. The thesis discusses design and implementation of such an integrated system capable of 3D holographic optical manipulation and multi-modal 3D imaging (in nonlinear optical modes like multiphoton fluorescence, coherent anti-Stokes Raman scattering, etc.) and how they are used to extensively study a vast number of LC based systems.

Understanding of LCs and topological defects go hand in hand. Appreciation of defects leads to their precise control, which in turn can lead to applications. The thesis describes discovery of optically generated stable, quasiparticle-like, localized

defect structures in a LC cell, that we call “Torons”. Torons enable twist of molecules in three dimensions and resemble both Skyrmion-like and Hopf fibration features. Under different conditions of generation, we optically realize an intriguing variety of novel solitonic defect structures comprising rather complicated configurations of point and line topological defects.

Introducing colloidal particles to LC systems imparts to these hybrid material system a fascinating degree of richness of properties on account of colloidal assemblies supported by networks of LC defects as well as variety of localized defects supported by colloidal particles. To fully understand and exploit the resultant interactions involving colloids and defects in LC systems to achieve the full potential of their practical applications, it is required that these be explored on the level of individual particles and defects. We explore a multitude of interactions mediated by defects over different length scales and demonstrate for the first time, creation of several types of colloidal assemblies such as sparse colloidal structures and three-dimensional defect-bound colloidal structures.

## **Dedication**

*To my parents.*

## ACKNOWLEDGEMENTS

It is because of the help and support of many throughout my graduate studies, that I have been able accomplish this task successfully. I wish to express my thanks to every one of them and sincerely apologize to those whose names may have been inadvertently omitted. The encouragement from my parents, my late grandparents and my sister has been a constant source of support for pursuance of my PhD and I thank them from the bottom of my heart.

I express deep gratitude towards my advisor, Prof. Ivan Smalyukh, who has helped me throughout my PhD in training me to perform experimental research, and in making my technical communications skills more effective in writing research articles and giving presentations. He has provided invaluable insights invaluable in identifying interesting and challenging experiments, conducting them successfully and interpreting the results. I also wish to thank many professors for providing valuable assistance throughout my graduate studies: Professors Garret Moddel, Noel Clark, Rafael Piestun, Won Park, David Walba, and Thomas Schibli.

My lab-mates and friends have been an integral part of my graduate life and have been a great company both inside and outside the lab. I thank them (in alphabetical order): Angel, Anubhav, Bohdan, Chanchal, Chris, Clayton, Dhaval, Gunjan, Heather, Nikhil, Paul, Rahul, Rajesh, Sachit, Taewoo, Tyler, Vinay, Xi, Yigit, and Zoom.

Everyone mentioned here and many more have been instrumental in completion of my PhD and here's a big thanks to all of them!

## Table of Contents

<b>1</b>	<b>Introduction .....</b>	<b>1</b>
1.1	Motivation .....	1
1.2	Optical Manipulation in Liquid Crystals .....	5
1.3	Imaging of Liquid Crystals .....	6
1.4	Thesis Overview .....	13
<b>2</b>	<b>Experimental Techniques .....</b>	<b>15</b>
2.1	Introduction .....	15
2.2	Holographic Optical Trapping (HOT) .....	16
2.3	Multimodal Nonlinear Optical Polarizing Microscopy (MNOPM) .....	17
2.4	Imaging With MNOPM .....	20
2.5	Applications of HOT+MNOPM: Illustrative Examples .....	24
2.6	HOT + MNOPM: Discussion .....	31
2.7	Summary .....	35
2.8	Appendix I: Material Preparation .....	35
2.9	Appendix II: Material Properties .....	37
2.10	Appendix III: Classification of Defects in Cholesteric Liquid Crystals .....	38
<b>3</b>	<b>Optical Generation of Defects .....</b>	<b>40</b>
3.1	Introduction .....	40
3.2	Structure of Torons .....	42
3.3	Controlled Generation of Torons .....	46
3.4	Other Localized Excitations: Toron Cousin Structures .....	49
3.5	Summary .....	55
3.6	Appendix I: Cholesteric Fingers .....	58
<b>4</b>	<b>Interactions and Patterning of Colloids and Defects .....</b>	<b>61</b>
4.1	Introduction .....	61
4.2	Defect-mediated Colloidal Interactions .....	63
4.3	Defect-arbitrated Colloidal Patterning .....	68
4.4	Summary .....	73
4.5	Appendix I: Analytical Estimates .....	75
4.6	Appendix II: Experimental Estimation of Defect Core Energy.....	76
<b>5</b>	<b>Assemblies of Particles in Cholesteric Matrix .....</b>	<b>82</b>
5.1	Introduction .....	82
5.2	Structure of Defects Around Particles .....	84
5.3	Elastically- and Defect-bound Assemblies.....	85
5.4	Summary .....	92
<b>6</b>	<b>Outlook and Conclusions .....</b>	<b>94</b>
	<b>Bibliography .....</b>	<b>99</b>

## List of Figures

**Fig. 1.1.** Liquid Crystals: Larger than displays. Liquid crystals are being explored to have a wide-ranging importance in applications such as (a) bio-sensors that would give an optical indication upon sensing a particular species, (b) lasers that can be tuned by stretching the material. (c) They are also important from biochemical standpoint, we see very short DNA molecules form LC phases.

**Fig. 1.2.** Liquid Crystal Colloids. Introducing colloids to LCs assigns novel properties to the mixture. (a) A nematic LC dispersed with colloids forms a defect-supported gel (b) In cholesteric LCs, particle-supported defect networks have shown to significantly enhance bulk elastic constants of the composite. (c) LCs (blue phase shown) can also prove to be a template for 3D assembly of colloids.

**Fig. 1.3.** Energy Diagram for multiphoton processes. (a) Comparing two- and three-photon fluorescence process with single photon fluorescence. (b) Second- and third-harmonic generation process.

**Fig. 1.4.** Energy Diagram for CARS. Three photons, a pump ( $\omega_p$ ), Stokes ( $\omega_s$ ), and probe ( $\omega_p$ ) combine to give a short wavelength anti-Stokes photon ( $\omega_{as}=2\omega_p-\omega_s$ ).

**Fig. 2.1.** Schematic diagram of the holographic optical tweezers setup.  $L_1$  ( $f_1=100\text{mm}$ ),  $L_2$  ( $f_2=250\text{mm}$ ),  $L_3$  ( $f_3=850\text{mm}$ ), and  $L_4$  ( $f_4=400\text{mm}$ ) are plano-convex lens with anti reflection coating for 1064nm;  $M_1$ ,  $M_2$ ,  $M_3$ ,  $M_4$ , and  $M_5$  are silver-coated mirrors; GLP is a Glan-laser polarizer for 1064nm; HW is a half waveplate; SLM is the LC Spatial light modulator; CS is the cover slip; PM is the Power meter; QW is a Quarter wave plate; P is the Polarizer; DM is the dichroic mirror; MO is the Microscope Objective.

**Fig. 2.2.** Schematic diagram of the MNOPM setup. The inset shows spectra (note that intensity scales are different) at marked positions in the setup: (A) after the PCF, (B) pump/probe pulse at 780nm, and (C) broadband Stokes pulse after the beam combiner. AL: achromatic lenses, BPF: band pass filter, BS: beam splitter, CL: collecting lens, DM: dichroic mirror, FI: Faraday Isolator, FM: flip mirror, GLP: Glan laser polarizer, HWP: broadband half wave plate, LPF: long pass filter, OL: objective lens, PCF: photonic crystal fiber, PMT: photon multiplier tube, RP: rotating polarizer, SPF: short pass filter, TNPR: twisted nematic polarization rotator.

**Fig. 2.3.** Schematic diagram of the integrated MNOPM and HOT optical setup built around an inverted microscope. The components of MNOPM: HWP: half wave-plate, GLP: Glan-laser polarizer, PCF: photonic crystal fiber, AL: aspheric lens, BS: beam-splitter, BC: beam combiner, FM: folding mirror, PMT: photo-multiplier tube, DM:

dichroic mirror, OL: objective lens. The components of the HOT: SLM: spatial light modulator, L1, L2, L3, L4: plano-convex lenses, DM-IR: dichroic mirror for the IR trapping laser.

**Fig. 2.4.** Cross-sectional images of a cholesteric LC with 10 $\mu$ m pitch. (a) 2PF image of BTBP doped cholesteric for excitation at 980nm and detection with 535/50nm BPF. (b) Schematics of  $\mathbf{n}(\mathbf{r})$  in a planar cholesteric cell. (c) 2PF spectrum of the BTBP-doped cholesteric LC and 3PF and broadband CARS spectra of an unlabeled cholesteric LC. Images of labeling-free cholesteric LC obtained using (d) 3PF with 870nm excitation and detection with a 417/60nm BPF and (e) CARS-PM with excitation of 780nm pump/probe and a broadband Stokes pulses and detection with a 661/20nm BPF.

**Fig. 2.5.** Simultaneous 3PF and SHG imaging of a SmC\* LC. 3PF images first obtained separately for (a,b) two orthogonal polarizations and then superimposed for (c) in-plane and (d) vertical cross-sections. SHG images first obtained separately for (e,f) two orthogonal polarizations and then superimposed for (g) in-plane and (h) vertical cross-sections. (i) Spectra and filter selections corresponding to the images. (j) Spectra showing the excitation pulse and the generated SHG signal. 3PF and SHG signals were forward-detected using 417/60nm and 535/50nm BPFs, respectively.

**Fig. 2.6.** Manipulation and imaging of spherical microparticles in a cholesteric LC. Images show vertical cross-sections of planar cholesteric LC cells obtained in 3PEF (a-c) and CARS (d-f) modes, displaying the cholesteric lamellae having spherical microparticles embedded within them. Particles of 4  $\mu$ m diameter are optically trapped and moved within as well as across the cholesteric layers. The nonlinear signals are collected in the forward direction with a BPF 417/60 for 3PEF and a BPF 661/20 for CARS of CN stretching vibration of 5CB. (g) shows the excitation and the fluorescence spectra of 3PEF for 5CB. (h) shows the broadband Stokes, the pump/probe at 780 nm and the broadband CARS spectrum obtained from the LC with different peaks in the CARS spectra marked to indicate the corresponding Raman vibration. The molecular structure of 5CB is shown in the inset.

**Fig. 2.7.** 3D Imaging of GaN nanorods dispersed in a cholesteric LC. GaN nanorods are manipulated in the layered structure of the cholesteric LC and the LC-nanorod composite is imaged in its lateral plane as well as in the vertical cross-section in two nonlinear modes: the LC is probed using 3PEF (a, b) and CARS (d, e) and the nanorods are visualized in SHG. (c) shows the spectrum with the excitation at 870 nm and the 3PEF emission from the LC molecules and SHG (at 435 nm) from the GaN nanorods. The nanorods interacting with a cholesteric dislocation are imaged in 3PEF (f-h). (g) shows 3PEF image of a dislocation comprising  $\lambda^{+1/2}$  and  $\lambda^{-1/2}$  disclinations in its vertical cross-section. The schematic diagram of the molecular director pattern around the dislocation with the position of the nanorod embedded in it is shown in (i).

**Figure 2.8.** Nanorods as nanoscale probes of the long-range molecular alignment in LCs. (a) SEM micrographs showing GaN nanorods as grown on a thin AlN buffer layer on a Si(111) substrate. The inset in a, shows that nanorods have hexagonal cross-sections. (b,c,d) Polarizing optical microscopy textures showing that the nanorod orientations visualize temporal evolution of  $\mathbf{n}(\mathbf{r})$  as nematic defects annihilate; the elapsed time and the resulting uniform orientation of  $\mathbf{n}(\mathbf{r})$  are marked on the images. (e) Schematics of the structure around the GaN nanorods in the LC with the uniformly-aligned far-field  $\mathbf{n}(\mathbf{r})$ . (f) Vertical nanorod position  $z_{\text{rod}}$  along the helical axis is a linear function of  $\phi_{\text{rod}}$  matching that of the ground-state helicoidal structure (solid line). The reading error of  $\pm 0.5 \mu\text{m}$  is shown by error bars.

**Figure 2.9.** Probing the Burgers vector and structure of a  $b=p/2$  dislocation with core split into the  $\lambda^{+1/2}\tau^{-1/2}$  pairmark  $\lambda$  &  $\tau$  in the figure. (a-f) Direct probing of Burgers vector by sequential translation of the nanorod along a Burgers circuit that includes points 2-7 in (a-f): (a) starting position at the point #2; (b) the nanorod was continuously translated beneath the dislocation to the new location #3 and then (c) rotated  $180^\circ$  CCW with the corresponding translational shift upward for one cholesteric layer; pushing nanorod to the right on the image revealed that the layer is discontinuous and location of the dislocation core; (d) the rod was rotated  $180^\circ$  CCW again while shifting one layer upward; e, the nanorod was moved above the dislocation to the position # 6 and then (f) rotated  $180^\circ$  CW while shifting one layer downward and closing the Burgers circuit (g) Layers displacement around the edge dislocation and nanorod positions corresponding to a-f (red filled circles). (h) Schematics of the visualized core structure of the  $b=p/2$  dislocation with the Burgers circuit and core probing nanorod trajectory (red) around the defect line.

**Fig. 2.S1.** Dislocations in Cholesteric LC. We show three different types of edge dislocations in their vertical cross-sectional plane. (a)  $\lambda^{+1/2}\tau^{-1/2}$  dislocation with  $|\mathbf{b}| = p/2$  (b)  $\tau^{+1/2}\lambda^{-1/2}$  dislocation with  $|\mathbf{b}| = p/2$  (c)  $\lambda^{+1/2}\lambda^{-1/2}$  dislocation with  $|\mathbf{b}| = p$ .

**Fig. 3.1.** Triple Twist Toron field configurations generated by LG beams and embedded into a uniform field by defects. (a) Toron structure with the topological charge “+2” due to the twist-escaped nonsingular disclination ring of strength  $s=+1$  shown by the red line. (b) “-1” hyperbolic point defect and (c) a ring of  $s=-1/2$  disclination topologically equivalent to a “-1” point defect, both exhibiting twist of  $\mathbf{n}(\mathbf{r})$  with the sense of twist shown by red arrows. (d) T3-1 configuration with the Toron accompanied by two hyperbolic point defects. (e) T3-2 structure containing a point defect and a disclination ring. (f) T3-3 configuration with two  $s=-1/2$  defect rings. (g-j) light intensity distributions in the lateral  $xy$  (left) and axial  $xz$  (right) planes of the LG beams of topological charge marked for each of the image pairs; the square cross-sections are  $4 \mu\text{m}$  wide.

**Fig. 3.2.** FCPM imaging and computer simulations of laser-generated Torons. (a) Three-dimensional image of the T3-1 configuration obtained using FCPM with circularly polarized probing light. (b) Vertical cross-section of the  $\mathbf{n}(\mathbf{r})$  of corresponding three-dimensional T3-1 structure obtained by numerical

minimization of the elastic free energy; blue circles denote the hyperbolic point defects and the red ones show the twist-escaped disclination intersecting the plane of the cross-section. (c) In-plane FCPM cross-section passing through the central plane of the T3 structure and containing the circular axis of the torus; the red bars indicate the location of the vertical cross-section. (d) Experimental vertical FCPM cross-section and (e) corresponding computer-simulated FCPM texture obtained for circularly-polarized probing light and the equilibrium director field shown in (b). The confinement ratio is  $d/p=1$  in both the experiments and the simulations.

**Fig. 3.3.** Computer simulations and FCPM imaging of in-plane cross-sections of T3-1 Toron. (a) Schematic representation of the T3-1 structure with the hyperbolic point defects shown by blue dots and the twist escaped non-singular disclination ring shown by a red line. (b) Computer simulated  $\mathbf{n}(\mathbf{r})$  in the central plane b-b cross-section shown in (a) of the T3-1 structure containing the disclination ring. (c,f) In-plane cross-sections of  $\mathbf{n}(\mathbf{r})$  in the vicinity of point defects near the bottom plate, (c) and the top plate (f). (d,g) Corresponding simulated and (e,h) experimental FCPM textures. The red bars in (e) and (h) indicate the FCPM linear polarization states.

**Fig. 3.4.** FCPM imaging of the T3-2s with different locations and diameters of disclination rings. (a-c) FCPM vertical cross-sections of three different T3-2s in a cell of thickness  $d = 15 \mu\text{m}$  with different diameters of the disclination ring at the bottom surface. (d,e) 3D FCPM images of the T3-2 structures having the disclination rings (d) at the bottom and (e) at the top surface.

**Fig. 3.5.** Predetermined optical generation and switching of the Toron structures. (a) Polarizing optical microscopy texture showing T3-1 (the smallest), two T3-2s of opposite winding (intermediate size), and T3-3 (the largest structure) generated next to each other. The inset shows letters “CU” obtained by optical generation of four T3-2s per letter at the letters’ vertices and T3-1 elsewhere within the characters. Orientations of crossed polarizer (P) and analyzer (A) are shown by white bars. (b) Polarizing microscopy image showing that the two T3-2s of opposite spiraling and the T3-1 can be generated at arbitrary location in the sample and then moved to the desired position, such as the one shown in (c), using optical manipulation by laterally shifting the generating infrared laser beam. (c) After optically moving the T3-1 to the image center, the new T3-3 structure is generated in the top right corner of the image; this T3-3 structure is then transformed into a T3-2 structures as shown in (d,e) then to T3-1 shown in (f), and again to the T3-3 configuration shown in (g) by using LG beams of appropriate topological charge values  $l$  marked on the images. Note that the T3-3 structures in (c,d,g) have different diameters of the disclination rings at the top and bottom surfaces and all T3-2s and T3-3s have lateral dimensions 1.1-1.5 times larger than T3-1s.

**Fig. 3.6.** Localized Excitation Type-I. (a) Structure imaged in its mid-plane. (b-c) vertical cross-sections obtained using FCPM in two orthogonal linear polarizations.

(d) Schematic of molecular director reconstructed from the cross-sectional images. The twist-disclination loops are shown in red.

**Fig. 3.7.** Structure of the confining twist disclination loop. (a) The molecular arrangement within a loop of twist-disclination (in red) close to a homeotropic surface. (b) The twist-disclination loops of opposite strengths (opposite sense of twist angles) that confine the structure shown in Fig. 3.6.

**Fig. 3.8.** Localized Excitation Type-II. This structure is similar to Type-I as revealed from its imaging in circular polarization. (a) The structure in its mid-plane. (b) vertical FCPM cross-section, and (c) molecular director pattern as deduced from the cross-sectional images.

**Fig. 3.9.** Localized Excitation Type-III. The structure is imaged using FCPM in linear polarizations as marked, (a) in its mid-plane and, (b-c) vertical cross-sectional planes.

**Fig. 3.10.** Schematic representation of Type-III structure. The structure reveals an arrangement of two nonsingular ( $\lambda$ ) disclination loops in the bulk and two singular twist-disclination loops close to the same surface.

**Fig. 3.S1.** Cholesteric Finger CF1. The vertical cross-section shows two  $\lambda^{+1/2}$  (filled dots) and two  $\lambda^{-1/2}$  (hollow dots) nonsingular disclinations in the bulk that comprise the finger.

**Fig. 3.S2.** Cholesteric Finger CF2. The cross-section representation shows nonsingular  $\mathbf{n}(\mathbf{r})$  comprising one  $\lambda^{+1}$  (filled dot) and two  $\lambda^{-1/2}$  (hollow dots) disclination lines.

**Fig. 3.S3.** Cholesteric Finger CF3. The  $\mathbf{n}(\mathbf{r})$  in the vertical cross-section shows two singular twist-disclinations of strengths  $+\pi$  and  $-\pi$  close to the surfaces (red dots). This type of finger is much narrower than the others.

**Fig. 3.S4.** Cholesteric Finger CF4. The  $\mathbf{n}(\mathbf{r})$  in the vertical cross-section of this type of finger is revealed to comprise two nonsingular disclinations:  $\lambda^{+1/2}$  (filled black dot) and  $\lambda^{-1/2}$  (hollow black dot) and two singular twist-disclinations of strength  $+\pi$  and  $-\pi$  (red dots).

**Fig. 4.1.** Defect-particle interaction mediated by a Lehmann cluster. (A) A defect cluster in a cholesteric LC (ZLI-2806 and CB15) terminates at a particle and can be stretched by optically translating it but contracts once the colloid is released from the trap. (B) A Lehmann cluster in a cholesteric LC (5CB and CB15) is manipulated with the help of an optically trapped particle so as to form a node of clusters. Upon turning the trap off, the particle returns to its original position along the defect line between two stationary trapped colloids, as seen in the frames marked with elapsed

time. (C) Vertical 2PEF-PM cross section of an elementary Lehmann cluster. (D) Lehmann cluster terminating on two particles. (E) Distance vs. time plot for the particle in (A) shown by solid line and for the particle in (B) shown by dashed line. (F) A schematic representation of an elementary Lehmann cluster terminating on a particle; the blue and red lines trace the  $\lambda^{-1/2}$  and  $\lambda^{+1/2}$  defects, respectively.

**Fig. 4.2.** Tensile defect-particle interactions mediated by various oily streaks. (A) An optically trapped particle, embedded in the core of an elementary Lehmann cluster, is used to transform the defect core structure. (B) Distance vs. time plot describing motion of the particle shown in (A) when released from the trap. (C) A schematic representation of the initial and the resultant defect core structures in their vertical cross-sections; the blue and red lines trace  $\lambda^{-1/2}$  and  $\lambda^{+1/2}$  disclinations in the defect cores, respectively. (D) FCPM vertical cross-sections of the Lehmann cluster and (E) the resultant oily streak having a modified core structure.

**Fig. 4.3.** Displacement of a Lehmann cluster across layers. (A) polarizing microscopy image showing how a Lehmann cluster terminating on an optically manipulated particle traverses layers via kinks in the form of windings. (B-D) In-plane 2PEF-PM images showing that the Lehmann cluster is at different depth across the layers on two sides of the kink. (E-G) Vertical 2PEF-PM cross-sections in the locations marked on the in-plane images (B-D). (H) Vertical 2PEF-PM cross-sections along the length of the defect for two orthogonal polarizations of the probing light. (I) A schematic of the reconstructed 3D director field and winding mechanism, with the vertical cross-section planes corresponding to cross-sectional images labeled alongside; the blue and red lines trace the  $\lambda^{-1/2}$  and  $\lambda^{+1/2}$  disclinations of the cluster, respectively. (J) The position of kinks along the cluster's length can be displaced or locked with the help of a particle.

**Fig. 4.4.** 3D patterning of particles within a Lehmann cluster. (A) In-plane FCPM image showing particles embedded in a Lehmann cluster at different depths. (B-D) Vertical cross-sections showing particles localized inside the Lehmann cluster and centered at different  $\lambda^{+1/2}$  and  $\lambda^{-1/2}$  disclinations. (E) Distance vs. time plot for the motion of a particle perpendicular to the length of the cluster, as it is attracted towards the  $\lambda^{+1/2}$  disclination (blue curve; the particle initial position is within the same cholesteric layer as the  $\lambda^{+1/2}$  defect line). The red curve shows similar data for the motion of two attracting particles embedded in the same  $\lambda^{-1/2}$  disclination. The insets show initial and final particle positions for both cases. (F) Distance dependence of the interaction energy for particle-defect and particle-particle interactions. (G-I) Self-arrangement of colloids within a Lehmann cluster as seen in vertical cross sectional images perpendicular to (G,H) and along (I) the length of the defect.

**Fig. 4.5.** 3D patterning of particles along edge dislocations with kinks. (A) Lateral manipulation of a kink in an edge dislocation using an optically trapped particle. (B) In-plane image showing particles embedded within an edge dislocation and separated by kinks; the inset schematically shows how colloidal particles localize on

edge dislocations at different depths within the layered system while separated by kinks. (C) Vertical FCPM cross-section along the length of an edge dislocation. (D) A series of vertical FCPM cross-sections in planes perpendicular to the dislocation as marked in (B). (E) Distance vs. time plot describing the motion of interacting particles embedded into the dislocation: the particles repel from each other (blue curve) when separated by a kink but mutually attract (red curve) without kinks. The initial and final positions of the particles are shown in the insets for both cases. (F,G) Schematics of two alternating core structures of the  $b=p/2$  dislocation as it shifts vertically to form kinks. (H) The distance dependence of the interaction energy for both the repulsive (blue) and the attractive (red) inter-particle interactions within the edge dislocation without and with separating kinks, respectively. (I) planar and (J,K) vertical cross-sections of particles arranged in a dipolar fashion within the core of a  $b=p/2$  dislocation.

**Fig. 4.6.** Generation of kink/anti-kink pairs using optical tweezers. (A) A particle embedded inside the  $\tau^{+1/2}$  disclination of the dislocation is optically trapped. At high power, the axial laser trapping force acting on the particle pushes the dislocation to a different cholesteric layer. (B) Similar generation of the kink/anti-kink pair can be achieved with axial manipulation of two colloidal particles, which now allow one to control locations of the kink and anti-kink. (C) Schematic illustration showing the controlled generation of a kink/anti-kink pair by simultaneous axial translation of colloidal particles across lamellae. (D) Vertical 2PEF-PM cross-sections of the cholesteric layered sample in the vicinity of the generated kink/anti-kink pair, showing how the axial shift of the dislocation is accompanied by the transformation of dislocation cores.

**Fig. 4.S1.** Measurement of tension of a Lehmann cluster by its manipulation using an optically trapped colloid. (A) The defect and the particle in the initial position. (B) The optically trapped particle is pushed against the defect until (C) the component of the line tension balances the laser trapping force, yielding the line tension of about  $T=19.64\text{pN}$ , determined using the maximum bending angle  $q$ . The measurement was done for 5CB- and ZLI-2806-based cholesteric LCs with  $5\ \mu\text{m}$  pitch, where  $\eta$  is (unknown) viscosity of ZLI-2806 in Pa·s.

**Fig. 4.S2.** Tension of defects of different width for cholesteric liquid crystals based on 5CB and ZLI-2806. The cores of the defect are separated by  $s = 1.5p$  (A),  $2p$  (B), and  $2.5p$  (C), respectively. The values of tension are given in terms of the viscosity  $\eta$  of ZLI-2806 in Pa·s.

**Fig. 4.S3.** Measurement of defect line tension by means of its direct optical manipulation. (A-C) A defect structure is drawn out of a Lehmann cluster with the help of optical tweezers. (C-E) When the trap is released, the defect structure contracts to reduce its tensile free energy. (F) Videomicroscopy tracking of the tip of the contracting defect.

**Fig. 4.S4.** Measurement of line tension of a defect with multiple interrupted layers (large  $s$ ) by means of its manipulation using a particle as a “handle”. (A) A colloidal particle embedded inside an oily streak is manipulated to “draw” a new defect. Upon turning off the trap, the particle returns to its original position under the tension of the stretched defect line. (B) Similar manipulation without the help of a particle, performed directly on the defect. (C) The rate of contraction of the defect vs. time in each case.

**Fig. 5.1.** Structure of defect around a colloid in cholesteric LC. (a) LC around a particle is locally melted using optical tweezers. Upon quenching, in a time-sequence of images, we see a twisted ring defect transform into a point defect for a 10- $\mu\text{m}$  diameter particle in 12- $\mu\text{m}$  pitch cholesteric LC. (b) The defect under crossed polarizers. (c) Layer distortion due to the particle in vertical cross-section using 3PEF. (d-f) Similar set of images for a particle 10  $\mu\text{m}$  in diameter, dispersed in a cholesteric LC with 25  $\mu\text{m}$  pitch.

**Fig. 5.2.** Elastically bound particle assemblies. (a-c) Chiral dipolar particles form assemblies under attractive elastic interaction as shown. These assemblies are not only confined to the same cholesteric layer as in (a) but also formed when the particles are separated along the helical axis by  $\approx p/4$  (b) or  $\approx p/2$  (c). (d) An inplane assembly of multiple chiral dipolar particles, in the shape of a curved chain. (e) An assembly formed by several particles at different depths along the helical axis. (f) Interparticle separation as a function of time, as the particles are attracted towards each other to form the in-plane assembly in (a). (g) The interaction energy of the assembly in (a) as a function of interparticle separation.

**Fig. 5.3.** Angular dependence of the elastic interaction. Interaction between two particles with parallel in-plane dipole moments is measured as a function of angular separation. The trajectories showing relative separation is displayed in different colors for different initial configuration. The initial positions are marked with a black dot.

**Fig. 5.4.** Defect-bound particle assemblies. 10  $\mu\text{m}$  diameter particles in 12  $\mu\text{m}$  pitch cholesteric. We can optically form and switch between several types of in-plane or out-of-plane assemblies. (a,b,c) transmission micrograph, 3PEF in-plane section, and 3PEF vertical cross-section, respectively for one type of in-plane assembly. (f,g,h) similar set of images for out-of-plane defect-bound assembly. (i,j,k) Similar set of images for another type of in-plane assembly. (d) Interparticle separation vs. time during formation of assembly shown in (f). (e) Interaction energy vs. distance between particles as it forms assembly in (f).

**Fig. 5.5.** Formation of defect-bound assemblies. The defect-bound assemblies are formed by a pair of particles with anti-parallel in-plane dipole moments. Depending on the mutual orientation of the dipoles, we end up with either an assembly confined within the same cholesteric layer (a,b), or one wherein particle are separated along the helical axis, (c,d).

**Fig. 5.6.** Defect-bound particle assemblies of 10  $\mu\text{m}$  diameter particles in 25  $\mu\text{m}$  pitch cholesteric. (a-d) The in-plane assembly is depicted with the help of transmission micrograph (a), cross-polarized micrograph (b), 3PEF in-plane image (c), and 3PEF vertical cross-section (d). (e-h) Similar set of images for a different type of particle assembly. This configuration is similar to the chains formed by dipolar particles in nematic LCs.

**Fig. 5.7.** 3D defect-bound multi-particle assemblies. 4  $\mu\text{m}$  diameter particles dispersed in 5  $\mu\text{m}$  pitch cholesteric. (a) Assemblies formed by three (a), and four particles (b). (c) A large 3D assembly formed of eight particles, created by bringing in one particle at a time, as shown with the help of selected frames at the end of different steps.

### List of Publications

- [1] D. Engström, M. C. M. Varney, M. Persson, R. P. Trivedi, K. A. Bertness, M. Goksör, and I. I. Smalyukh. Unconventional structure-assisted optical manipulation of high-index nanowires in liquid crystals. *Opt. Exp.* **20**, 7741 (2012)
- [2] I. I. Smalyukh, D. Kaputa, A. V. Kachynski, A. N. Kuzmin, P. J. Ackerman, C. W. Twombly, T. Lee, R. P. Trivedi, and P. N. Prasad. Optically generated reconfigurable photonic structures of elastic quasiparticles in frustrated cholesteric liquid crystals. *Opt. Exp.* **20**, 6870 (2012)
- [3] R. P. Trivedi, I. I. Klevets, B. I. Senyuk, T. Lee, and I. I. Smalyukh. Multi-scale interactions and three-dimensional patterning of colloidal particles and defects in lamellar soft media. *Proc. Natl. Acad. Sci. USA* **109**, 4744 (2012)
- [4] N. Petit-Garrido, R. P. Trivedi, J. Igués-Mullol, J. Claret, C. Lapointe, F. Sagues, and I. I. Smalyukh. Healing of defects at the interface of nematic liquid crystals and structured Langmuir-Blodgett monolayers. *Phys. Rev. Lett.* **107**, 177801 (2011)
- [5] D. Engstrom, R. P. Trivedi, M. Persson, K. A. Bertness, M. Goksor, and I. I. Smalyukh. Three-dimensional long-range order and defect core structures in anisotropic fluids probed by nanoparticles. *Soft Matter* **7**, 6304 (2011)

- [6] R. P. Trivedi, D. Engstrom, and I. I. Smalyukh, Optical manipulation of colloids and defect structures in anisotropic media. *Jour. Opt.* **13**, 044001 (2011) (invited review for special issue on optical tweezers.)
- [7] D. B. Conkey, R. P. Trivedi, S.R.P. Pavani, I.I. Smalyukh, and R. Piestun. Three-dimensional parallel particle manipulation and tracking by integrating holographic optical tweezers and engineered point spread functions. *Opt. Exp.* **19**, 3835-3842 (2011)
- [8] R. P. Trivedi, T. Lee, K. A. Bertness, and I. I. Smalyukh. Three dimensional optical manipulation and structural imaging of soft materials by use of laser tweezers and multimodal nonlinear microscopy. *Opt. Exp.* **18**, 27658-27669 (2010)
- [9] T. Lee, R. P. Trivedi, and I. I. Smalyukh. Multimodal nonlinear optical polarizing microscopy of long-range molecular order in liquid crystals. *Opt. Lett.* **35**, 3447-3449 (2010)
- [10] I. I. Smalyukh, Y. Lansac, N. A. Clark, and R. P. Trivedi. Three-dimensional structure and multistable optical switching of triple-twist particle-like excitations in anisotropic fluids. *Nature Mater.* **9**, 139-145 (2010)
- [11] S. Anand, R. P. Trivedi, G. Stockdale, and I. I. Smalyukh. Non-contact optical control of multiple particles and defects using holographic optical trapping with phase-only liquid crystal spatial light modulator. *SPIE Proc.* **7232**, 723208 (2009) (invited paper)

**Book Chapter:**

- [12] T. Lee, B. Senyuk, R. P. Trivedi, and I. I. Smalyukh, Optical microscopy of soft matter systems. *Soft Matter*, A. Fernandez De Las Nieves (ed.), (Wiley-VCH, to be published). <http://arxiv.org/abs/1108.3287>

**In Preparation:**

- [13] N. Petit-Garrido, R. P. Trivedi, J. Iñes-Mullol, and I. I. Smalyukh. Surface dislocations in cholesteric liquid crystal confined by structured Langmuir-Blodgett monolayers.
- [14] R. P. Trivedi et al. Optically generated localized defect structures in twist-frustrated cholesteric liquid crystals.
- [15] R. P. Trivedi et al. Interactions and three-dimensional assemblies of chiral dipolar particles in cholesteric liquid crystals.

*There are certain defects which, properly implemented, shine brighter even than virtue.*

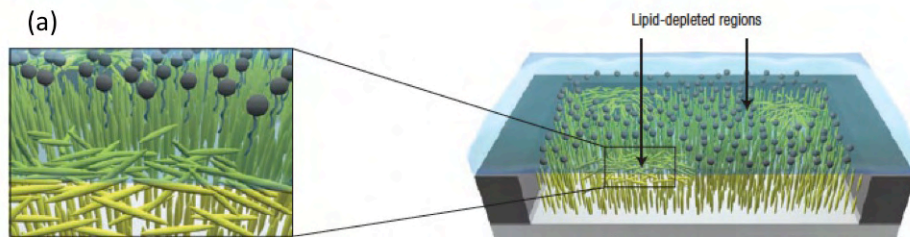
- La Rochefoucauld

## Chapter 1

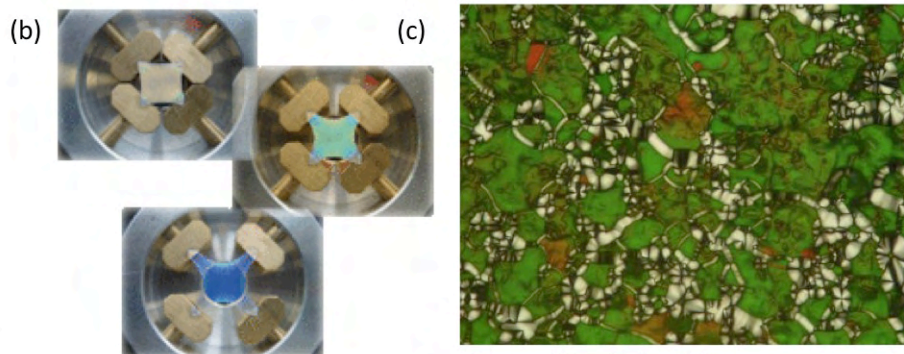
### Introduction

#### 1.1 Motivation

Liquid crystals (LCs) are soft materials usually composed of anisometrically shaped molecules imbricated to feature long-range orientational order with varying degrees of partial positional order [1,2]. They combine properties of crystals and fluids in a unique way in that they show both viscous as well as elastic and anisotropic optical properties in their behavior. In particular, nematic liquid crystals are comprised of rod shaped molecules, the average local orientation whereof is characterized by the director  $\mathbf{n}(\mathbf{r})$ . Optically, thus a uniformly aligned block of nematic LC is a uniaxial crystal with its optical axis along  $\mathbf{n}(\mathbf{r})$ . Liquid crystals, owing to their unique set of mechanical, electrical and optical properties, have been of both fundamental and technological interest. They have been long known to be important in display and other electro-optic technological devices [3-17] like spatial light modulators (SLM), non-mechanical beam-steerers, tunable optical filters, etc. and are promising in technological and biomedical applications such as liquid crystal biosensors, tunable lenses, distributed feedback lasers, muscle-like actuators, etc. They are also important from biological standpoint as lipids, viruses, membranes and cytoskeleton proteins form LC phases [18-28].



Source: S. J. Woltman et al. *Nature Materials* 6, 929 (2007)



Source: ScienceNOW news, Science magazine, May 2001

Source: ScienceDaily, 2007

**Fig. 1.1.** Liquid Crystals: Larger than displays. Liquid crystals are being explored to have a wide-ranging importance in applications such as (a) bio-sensors that would give an optical indication upon sensing a particular species, (b) lasers that can be tuned by stretching the material. (c) They are also important from biochemical standpoint, we see very short DNA molecules form LC phases.

In addition to having multitude of established as well as potential technological applications, liquid crystals are also often employed as proving grounds to study defect-related phenomena in fields ranging from early-universe cosmology [28,29] to condensed matter physics [30,31]. Topological defects play an important role in determining material properties, mediating phase transitions, and causing numerous irreversible phenomena [32-36]. For example, dislocations – line defects in periodically ordered materials – impart malleability to solids such as metals, and thus are of great practical importance. Lamellar media are often studied

using the model system of a cholesteric LC in which the local  $\mathbf{n}(\mathbf{r})$  twists around a helical axis to form a twist-periodic structure [2]. When spatial distortions of the equilibrium twisted structure are on a scale much larger than the helical periodicity, this one-dimensionally periodic system exhibits elastic properties similar to those of layered condensed matter systems [37,38]. Molecular, atomic, or spin configurations that are periodic in one direction, have many similar properties and are encountered in a multitude of other condensed matter systems, such as helimagnets [39], various smectic phases of LCs [2,31], water-surfactant mixtures [40,41], block-copolymers [42], colloidal assemblies [43], lipids [44], DNA condensates [23] etc. These media are of great interest from the standpoint of controlling their bulk elastic and optical properties by stabilizing and decorating networks of defects with particles [45,46]. A number of studies of colloids in LCs have revealed how their properties are enriched by presence of defects [45-55]. There is a fascinating degree of richness in these hybrid material systems on account of colloidal assemblies supported by networks of LC defects as well as localized defects supported by colloidal particles. These have been studied in the past by observing the modification in bulk mechanical/rheological properties [45,46], or have been confined to 2D arrangements [52-54]. To fully understand and exploit the resultant interactions involving colloids and defects in LC systems for their potential practical applications, it is required that these they be explored on the level of individual particles and defects. Stable localized defect structures can also be supported in a LC cell by virtue of its geometry and surface boundary conditions. Under different conditions for both, an intriguing variety of defect

structures comprising rather complicated topological assemblies of point and line defects can be induced optically by means of focused laser beams of various shapes.

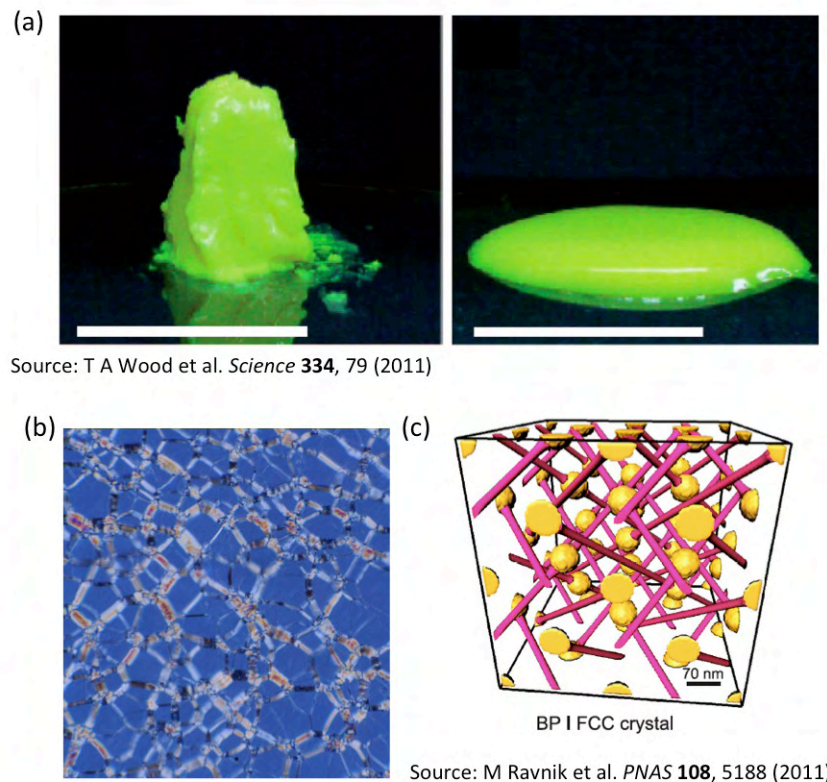


**Fig. 1.2.** Liquid Crystal Colloids. Introducing colloids to LCs assigns novel properties to the mixture. (a) A nematic LC dispersed with colloids forms a defect-supported gel (b) In cholesteric LCs, particle-supported defect networks have shown to significantly enhance bulk elastic constants of the composite. (c) LCs (blue phase shown) can also prove to be a template for 3D assembly of colloids.

To achieve the goal of optically manipulating these structures comprising defects and particles at microscale with an unprecedented control, and then to study the resultant molecular director patterns, needs development of powerful optical system. Techniques relying on application of external fields have been limited even when they use patterned electrodes manufactured using complicated fabrication methods. We have designed and implemented such an integrated system capable of

3D optical manipulation and imaging and used it to study a vast number of LC based composite systems extensively.

## **1.2 Optical Manipulation in Liquid Crystals**

Non-contact optical control has been of great interest in many fields of science and technology as it paves the way to manipulate objects spanning in size from single atoms to microparticles [56,57]. Soon after the first demonstration of optical technique for trapping micrometer-sized transparent dielectric particles suspended in a fluid medium, the advent of “optical tweezers” grew by leaps and bounds in biological and condensed matter physical science research [58,59]. In biology, growing research in cellular and molecular biology demanded methods for precise control of cells, cellular organelles and biopolymers, encouraging the optimization and further development of optical tweezers [60]. Study of physics of mesoscopic systems has become an important area of experimental research. Using optically-manipulated multiple colloidal particles as model systems, phenomena such as self-assembly and many-body interactions provide an accessible testing ground for ideas about matter at the atomic scale, and are interesting in their own right as complex systems. The need to control and perturb these systems has also been a great driving force for development of optical tweezers.

The development of holographic optical tweezers (HOT) has expanded the capabilities of optical trapping to handling multiple particles simultaneously [60]. This has been made possible by technological development of

programmable liquid crystal spatial light modulators (LC-SLM). In HOT, the SLM is configured to act as a phase or amplitude modulation diffractive optical element allowing a single incident laser beam to be split into multiple individually controllable beams. By updating the SLM with a sequence of holograms, the individual optical traps can be moved in 3D. Unlike other approaches to create multiple tweezers that use scanning mirrors or acousto-optic deflectors to laterally scan and thus time-share the laser beam amongst traps, the SLM can manipulate position of objects along the vertical axis as well. Moreover, both lateral and axial displacements of the multiple traps can be set independent of each other to create desired 3D structures. In addition, another major advantage of SLM is in creation of unconventional beam-intensity profiles such as optical vortices (e.g., Laguerre-Gaussian beams) [60]. This has rendered it possible to effectively trap particles with high absorption or refractive index lower than the surrounding medium, a task thitherto unachievable. Optical vortices have also allowed optical manipulation involving transfer of orbital angular momentum and have enabled various novel forms of manipulation techniques.

### **1.3 Imaging of Liquid Crystals**

The fast-growing field of soft matter research requires increasingly sophisticated tools for experimental studies. One of the oldest and most widely used tools to study soft matter systems is optical microscopy. Recent advances in optical microscopy techniques

have resulted in a vast body of new experimental results and discoveries, by applying them at length scales ranging from molecular to macroscopic.

Polarizing microscopy (PM) is an imaging technique traditionally used for study of birefringent and optically active materials, such as liquid crystals, minerals and crystals, where the sample is studied between two crossed or parallel polarizers. The linearly polarized incident light is split by the birefringent sample into two components, extraordinary and ordinary. The 2D intensity pattern in the image is used to deduce the spatial variations of the orientation of the optic axis and/or value of birefringence in the lateral plane of an optically anisotropic sample. Another approach, which is widely used for imaging of biological materials, fluorescence microscopy, employs absorption of light by molecules of fluorescent dyes, which results in the emission of light at longer wavelength. This wavelength difference makes it possible to effectively separate the excitation and emission signals with the help of optical filters. These 2D imaging techniques are severely limited in that, it is nearly impossible to deduce 3D variations of molecular director from 2D intensity pattern obtained from them, especially in samples containing colloids and intricate defect structures.

A more advanced technique, which offers 3D imaging capability by combining the features of fluorescence and confocal microscopies, is fluorescence confocal microscopy. The main feature of confocal microscopy is that the inspection region at a time is a small voxel (volume pixel) and the signal arising from the neighboring region is prevented from reaching the detector by having a pinhole in the detection image plane. It is thus possible to construct a 3D image of the sample by scanning voxel by voxel within the volume of interest. The orientational order of anisotropic soft matter systems can be

probed by combining this mode with the capability of polarized light excitation and detection. Fluorescence confocal polarizing microscopy (FCPM) [61-63] requires that the specimen be stained with anisometric dye molecules, which align parallel or perpendicular to the molecules of the studied “host” material. The intensity of fluorescence is maximized when the linear polarization of excitation light is parallel to the transition dipoles of excitation and fluorescence of the dye molecules in the sample, and is at minimum when the polarization is perpendicular to the transition dipoles. This strong orientational dependence of the measured fluorescence signal allows one to decipher the 3D molecular orientation patterns and liquid crystal director fields directly from the FCPM images.

Nonlinear optical microscopy techniques utilize intrinsic and/or extrinsic nonlinear optical responses of materials and are used for imaging of biological systems and a variety of soft matter systems. These imaging techniques are based on nonlinear light-matter interactions that result in either emission, such as multi-photon excitation fluorescence [64], or scattering, such as multi-harmonic generation [65,66], sum frequency generation [67], and coherent anti-Stokes Raman scattering (CARS) [68-70].

Nonlinear optical microscopy has recently emerged as a powerful tool for non-invasive, label-free imaging with high 3D resolution capable of probing highly scattering thick biological and soft matter systems. There are several advantages of using nonlinear optical microscopy as compared to conventional (linear) optical imaging techniques such as FCPM: (i) low out-of-focus photobleaching (multi-photon absorption occurs only at the focus), (ii) low photodamage (for example biological tissues absorb less in the near-

infrared), (iii) ability to excite ultra-violet (UV)-excitable fluorophores with visible or near-infrared light sources via two- or three-photon absorption, (iv) inherent optical sectioning (no pinhole required because the excitation volume is tightly confined around the focal spot), (v) ability to work with thicker and more viscous specimens (larger penetration depth on account of longer excitation wavelengths) and (vi) chemical bond selectivity in the case of coherent Raman imaging. However, nonlinear optical microscopy typically requires more expensive pulsed lasers (typically a femto-/pico-second pulsed laser) and more complicated microscopy setups that are rarely available commercially. Polarization sensitive excitation and detection of signals is very useful in the study of anisotropic materials such as liquid crystals for imaging of 3D patterns of long-range molecular orientation. The intensity of detected nonlinear optical polarizing microscopy signals depends on the angle  $\beta$  between the polarization of excitation pulses and the liquid crystal director  $\mathbf{n}(\mathbf{r})$  as  $\sim \cos^{2m} \beta$  for the detection with no polarizer and as  $\sim \cos^{2(m+1)} \beta$  for imaging with the polarizer in the detection channel collinear with the polarization of the excitation beam, where  $m$  is the order of the nonlinear process (for example  $m=2$  for two-photon excitation and  $m=3$  for three-photon excitation). Thus nonlinear optical imaging modalities have inherently higher orientational contrast than linear techniques.

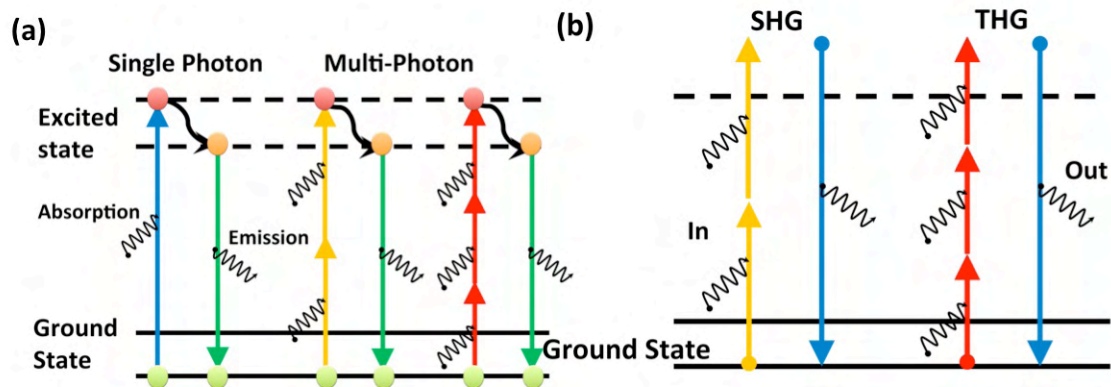


**Fig. 1.3.** Energy Diagram for multiphoton processes. (a) Comparing two- and three-photon fluorescence process with single photon fluorescence. (b) Second- and third-harmonic generation process.

Multi-photon excitation fluorescence employs absorption of two or three (or more) photons of near-infrared light and emission a single photon at a wavelength shorter than the excitation wavelength, by a fluorescent molecule. For this, the specimen may be tagged with an appropriate dye or self-fluorescence of the material can be used (which would require UV excitation were it to be performed in single photon mode, and hence impracticable). The comparison of energy diagrams of the single- and multi-photon processes is shown in Fig. 1.3. The second- and third-harmonic generation microscopies derive contrast from variations in a specimen's ability to generate the respective harmonic signal from the incident light. The energy diagram of second and third harmonic generation processes, Fig. 1.3 shows that there is no energy loss in the scattered light after multiple photons combine into a single photon of higher energy. Multi-harmonic generation does not depend on excitation of fluorescent molecules. Hence it is not required to tag the specimen with a dye and the effects of photobleaching and photodamage are avoided. The second-order susceptibility  $\chi^{(2)}$  in nonlinear process is nonzero only in non-centrosymmetric media while the third-order susceptibility  $\chi^{(3)}$  term

is nonzero for all media. Thus, imaging can also provide information about the symmetry of the studied materials by using these nonlinear processes.

Coherent anti-Stokes Raman scattering (CARS) microscopy is a non-invasive, label-free nonlinear imaging technique that utilizes molecular vibrations to obtain imaging contrast. CARS microscopy requires at least two pulsed laser sources at different frequencies. The spontaneous Raman signal is typically detected on the red side of the spectrum compared to the excitation radiation, where it might be difficult to discriminate it from fluorescence signal. On the contrary, CARS signal is detected on the blue side, which is free from fluorescence interference, but it typically comes with a non-resonant background contribution.

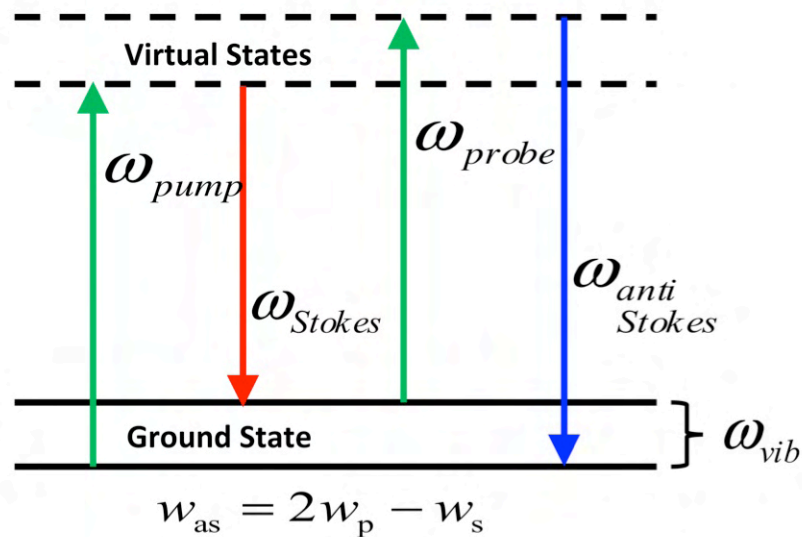


**Fig. 1.4.** Energy Diagram for CARS. Three photons, a pump ( $\omega_p$ ), Stokes ( $\omega_s$ ), and probe ( $\omega_p$ ) combine to give a short wavelength anti-Stokes photon ( $\omega_{as}=2\omega_p-\omega_s$ ).

The CARS technique utilizes a third order nonlinear process, typical implementation of which involves three photons at two different frequencies viz., pump/probe ( $\omega_p = \omega_{pump} = \omega_{probe}$ ) and Stokes ( $\omega_s = \omega_{stokes}$ ) beams as shown in Fig. 1.4.

When the frequency difference between the pump/probe and the Stokes beams matches a certain molecular vibrational frequency ( $\omega_{vib} = \omega_p - \omega_s$ ) and the phase-matching condition of three input photons is fulfilled, a strongly enhanced blue-shifted anti-Stokes ( $\omega_{as} = \omega_p + \omega_{vib} = 2\omega_p - \omega_s$ ) resonance signal is generated in the sample. The resultant CARS signal is at a wavelength shorter than both of the pump/probe and the Stokes beams, as shown in Fig.1.4 The CARS intensity scales with the intensities of the excitation beams as follows

$$I_{CARS}(2\omega_p - \omega_s) \propto (\chi_{CARS}^{(3)})^2 I_p^2(\omega_p) I_s(\omega_s),$$

where  $\chi_{CARS}^{(3)}$  is the third order susceptibility,  $I_p$  and  $I_s$  are the intensities of the pump/probe and Stokes beams, respectively.

There are several ways of generating the excitation pulses at two different wavelengths in CARS microscopy [71]: (i) two tightly synchronized pulsed lasers, (ii) a synchronously-pumped intra-cavity doubled optical parametric oscillator, (iii) a single femtosecond laser pulse spectrally shaped to select two frequencies, or (iv) a synchronously-generated supercontinuum (by using highly nonlinear fiber) with filter-selected  $\omega_p$  and/or  $\omega_s$  from a single femtosecond laser. CARS microscopy offers several unique advantages in the study of soft matter and biological samples: (i) intrinsic vibrational contrast (no labeling needed), (ii) a strong, directional signal (CARS is more sensitive than conventional vibrational microscopy), and (iii) 3D sectioning capability with less photodamage, no photobleaching, and deeper penetration in thick turbid media, similar to other nonlinear optical microscopy techniques.

A variety of optical microscopy techniques discussed here have driven the research in the field of soft matter systems to new frontiers. The older microscopy

techniques have allowed 2D imaging and hence the actual 3D configuration of material components composing soft-matter systems was often left to an educated guess. The introduction of 3D imaging techniques has facilitated unambiguous determination of the molecular and colloidal arrangement with precise localization of other elements. The advent of pulsed lasers has enabled implementation of nonlinear optical microscopies, furthering this trend and rendering the use of labeling agents unnecessary, while at the same time giving similar or better spatial resolution. Nonlinear optical microscopy has also made it more convenient to image composite soft-matter systems by allowing imaging of different constituents in different nonlinear modalities simultaneously, instead of going through the difficult, and often impossible process of finding appropriate dyes that would bind to each of the constituents selectively. Further general development of optical microscopy techniques is an ongoing quest that will continue to contribute to the body of knowledge of soft matter systems.

#### **1.4 Thesis Overview**

The thesis presents experimental realization of state-of-the-art techniques and their application for creation, manipulation and characterization of assemblies of defects and particles in liquid crystal based systems.

As motivated in earlier in the introductory remarks, we require state of the art optical techniques to achieve this goal of studying these LC based complex systems. To that effect, Chapter 2 discusses development of experimental tools, viz., integrated holographic optical trapping and multimodal nonlinear optical microscopy setup that allows us to accomplish this task of 3D optical manipulation

and imaging of liquid crystalline materials. This description is substantiated with a few demonstrative examples showing the strength of the experimental techniques developed and implemented.

In Chapter 3, I describe a variety of optically generated, stable structures in LCs, each intricate in its composition of constituent defects, which is revealed with the help of FCPM and nonlinear microscopy techniques. A breathtaking level of richness in the types of these structures is achieved by controlling the LC cell geometry and surface boundary conditions of the cell surfaces.

Chapter 4 provides a detailed account of distance-independent colloidal interactions mediated by line defects in cholesteric LCs. It then discusses how these defects can also be used, by exploiting their topological structure and by optically manipulating them to provide attractive or repulsive interactions for patterning of colloids to create sparse colloidal assemblies.

Chapter 5 discusses defects supported by colloidal particles (in contrast to the previous chapter, where we saw colloids supported by defects) in cholesteric LCs and how these give rise to novel kinds of elastic and defect-assisted interactions and possibilities of stable 3D structuring of particles.

In Chapter 6, I sketch an outlook for future work on extending the study of LC defect/colloidal assemblies and provide conclusions for the work presented here.

## Chapter 2

### Experimental Techniques

#### 2.1 Introduction

In this chapter, I describe design and development of experimental techniques as motivated in the introduction. To achieve the goal of performing simultaneous three-dimensional optical manipulation and non-invasive structural imaging of composite soft-matter systems, we have developed an integrated system of holographic optical trapping [72,73] and multimodal nonlinear microscopy [74,75]. We combine different nonlinear microscopy techniques such as coherent anti-Stokes Raman scattering, multi-photon excitation fluorescence and multi-harmonic generation, and use them for visualization of long-range molecular order in soft materials by means of their polarized excitation and detection [74-76]. The combined system enables us to accomplish manipulation in composite soft materials such as colloidal inclusions in liquid crystals as well as imaging of individual constituents of the composite material in different nonlinear optical modalities. I demonstrate the application of this system in manipulation of anisotropically shaped colloids (nanowires), and visualization of three-dimensional long-range molecular orientational patterns from nonlinear optical images [77,78].

## 2.2 Holographic Optical Manipulation

I describe here the design and development of the HOT system based on a LC-SLM [72,73]. A schematic diagram of the optical layout is presented in Fig. 2.1. The setup is built around an inverted microscope (IX-81, Olympus). We employ a continuous wave, Ytterbium-doped fiber laser (YLM series, IPG Photonics) at 1064 nm. The polarization of the beam incident on the SLM is tuned to maximize the phase modulation efficiency of the SLM by use of a Glan-laser polarizer and a half-wave plate. Two telescopes are introduced in the optical train of the HOT setup: the first one (lenses L1 and L2) to expand the beam diameter of the laser so as to overfill the active area of the SLM and the latter (lenses L3 and L4) to project the phase-modulation pattern encoded by the SLM onto the back-aperture of the objective as well as to resize the beam to slightly overfill the latter. We use high numerical aperture (NA) oil immersion microscope objectives (from Olympus) for holographic trapping: 60X (NA=1.42, ~65% transmission at 1064nm) and 100X (NA=1.4, ~70% transmission at 1064nm). The SLM itself is a reflective, electrically addressed, phase-only, LC-SLM with resolution of 512 x 512 pixels and pixel size of 15 x 15  $\mu\text{m}^2$  (obtained from Boulder Nonlinear Systems). The SLM can control the phase of the incident laser beam on a pixel-by-pixel basis by modulating it according to the holographic pattern supplied by the computer at an effective refresh rate of 30 Hz. This modulated light beam is imaged at the back aperture of the microscope objective acting as a Fourier transform lens. The holograms are generated on graphical user interface software HOTkit (obtained from Arryx).

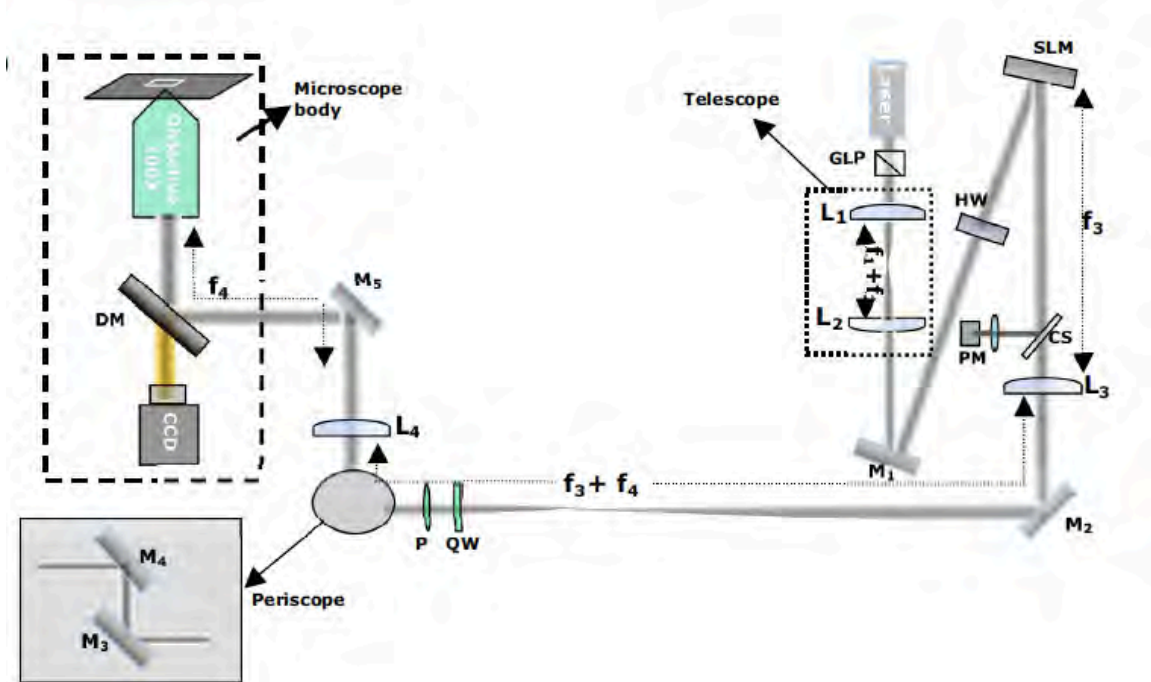


**Fig. 2.1** (a) Schematic diagram of the holographic optical tweezers setup.  $L_1$  ( $f_1=100\text{mm}$ ),  $L_2$  ( $f_2=250\text{mm}$ ),  $L_3$  ( $f_3=850\text{mm}$ ), and  $L_4$  ( $f_4=400\text{mm}$ ) are plano-convex lens with anti reflection coating for  $1064\text{nm}$ ;  $M_1$ ,  $M_2$ ,  $M_3$ ,  $M_4$ , and  $M_5$  are silver-coated mirrors; GLP is a Glan-laser polarizer for  $1064\text{nm}$ ; HW is a half waveplate; SLM is the LC Spatial light modulator; CS is the cover slip; PM is the Power meter; QW is a Quarter wave plate; P is the Polarizer; DM is the dichroic mirror; MO is the Microscope Objective.

### 2.3 Multimodal Nonlinear Optical Polarization Microscopy

While performing optical manipulation in LCs, it is imperative that the changes in  $\mathbf{n}(\mathbf{r})$  effected due to presence of defects, by inclusion of colloids, or by application of external optical fields, be imaged to elucidate the underlying physical phenomena. I describe here multimodal nonlinear optical polarizing microscopy (MNOPM) system [74,75] that combines multiple nonlinear optical imaging modalities to address this issue by directly probing the ordered arrangement of constituent molecules of the LCs instead of exclusively relying on additives such as dyes. MNOPM includes imaging modalities such as coherent anti-Stokes Raman

scattering (CARS), multi-photon excitation fluorescence (viz., two/three photon excitation fluorescence – 2PEF/3PEF), and multi-harmonic generation (e.g., second harmonic generation – SHG) with achromatic control of polarization of excitation beams using twisted nematic polarization rotator. I show here the integrated implementation of HOT with the MNOPM imaging system. This integrated system gives capabilities of non-contact 3D optical manipulation along with non-invasive, label-free, high resolution and orientation sensitive 3D imaging.

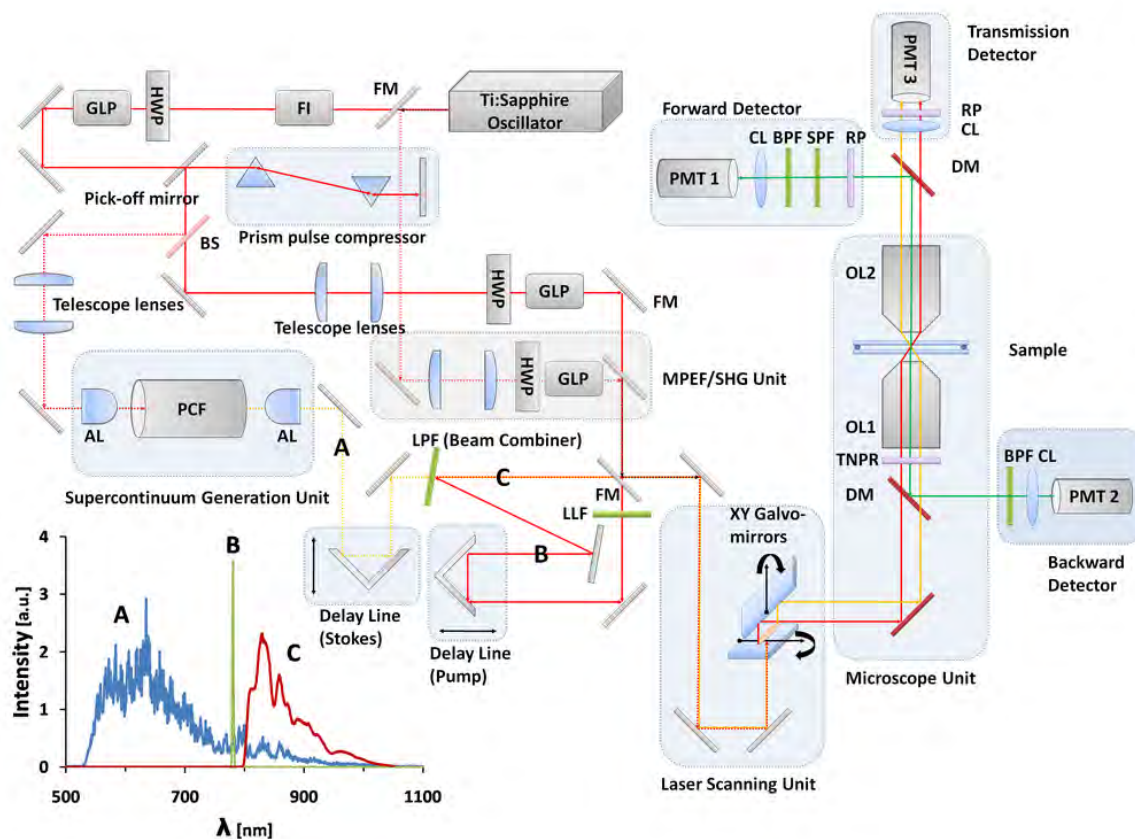


**Fig. 2.2.** Schematic diagram of the MNOPM setup. The inset shows spectra (note that intensity scales are different) at marked positions in the setup: (A) after the PCF, (B) pump/probe pulse at 780nm, and (C) broadband Stokes pulse after the beam combiner. AL: achromatic lenses, BPF: band pass filter, BS: beam splitter, CL: collecting lens, DM: dichroic mirror, FI: Faraday Isolator, FM: flip mirror, GLP: Glan laser polarizer, HWP: broadband half wave plate, LPF: long pass filter, OL: objective lens, PCF: photonic crystal fiber, PMT: photon multiplier tube, RP: rotating polarizer, SPF: short pass filter, TNPR: twisted nematic polarization rotator.

The schematic diagram of the MNOPM setup is shown in Fig. 2.2. A tunable (680-1080nm) femtosecond Ti:Sapphire oscillator (140fs, 80MHz, Chameleon Ultra-II, Coherent) is used for nonlinear optical excitation. For CARS imaging, a femtosecond pulse from the laser beam is split into a pump/probe beam and another beam synchronously pumping a highly nonlinear polarization maintaining photonic crystal fiber (PCF, FemtoWHITE-800, NKT photonics); the output of the PCF (marked "A" in Fig.2.2) is used as a synchronized broadband Stokes pulse. A Faraday isolator protects the Ti:Sapphire laser from the back-reflection of the PCF. Laser line filters (i.e., LL01-780, Semrock) are used to reduce the spectral bandwidth of pump/probe pulse. The pump/probe and Stokes pulses (marked "B" and "C" in Fig.2.2, respectively) are recombined spatially at a long pass filter (such as BLP01-785R, Semrock) and temporally by using delay lines in each beam path and then introduced into a laser scanning unit (FV300, Olympus). Power and polarization of pulses in different parts of the setup are controlled by half wave plates and Glan-laser polarizers. Both pump/probe and Stokes pulses are focused into a sample using an oil-immersion objective (100x, NA=1.4) the inverted microscope. A galvano-mirror scans the sample laterally in the focal plane of the objective while the motion of the objective along the microscope's optical axis is controlled by a stepper motor. MNOPM signals are collected by either the same objective (epi-detection mode) and/or another oil-immersion objective (60x, NA=1.42) in forward mode and detected by photomultiplier tubes (H5784-20, Hamamatsu). A series of long-pass dichroic mirrors (i.e., FF735-Di01-25x36, Semrock) and short-pass and band pass filters (BPFs) are used for spectral selection

of various nonlinear optical signals in the detection channels. We utilize excitation pulses with collinear polarizations controlled by a twisted nematic polarization rotator or an achromatic half-wave plate. The same objective is used for both optical manipulation and imaging: a simplified schematic diagram of the complete integrated setup is shown in Fig. 2.3.

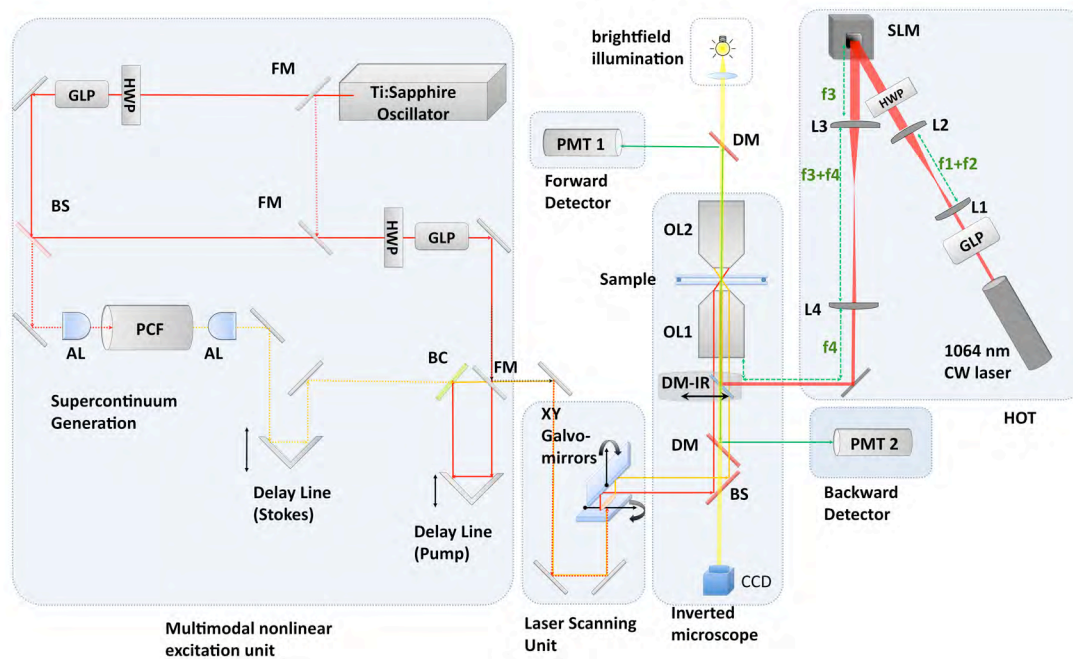


**Fig. 2.3.** Schematic diagram of the integrated MNOPM and HOT optical setup which is built around an inverted microscope. The components of MNOPM: HWP: half wave-plate, GLP: Glan-laser polarizer, PCF: photonic crystal fiber, AL: aspheric lens, BS: beam-splitter, BC: beam combiner, FM: folding mirror, PMT: photo-multiplier tube, DM: dichroic mirror, OL: objective lens. The components of the HOT: SLM: spatial light modulator, L1, L2, L3, L4: plano-convex lenses, DM-IR: dichroic mirror for the IR trapping laser.

## 2.4 Imaging with MNOPM

I present here a few examples, with the help of which, we can see the strength of imaging orientational order of LCs with MNOPM. The system provides us

with the capability to image a material in multiple modalities, contingent on nonlinear optical properties of the material to be characterized. The 3D imaging capability simplifies the process of delineating complex director patterns present in LCs.

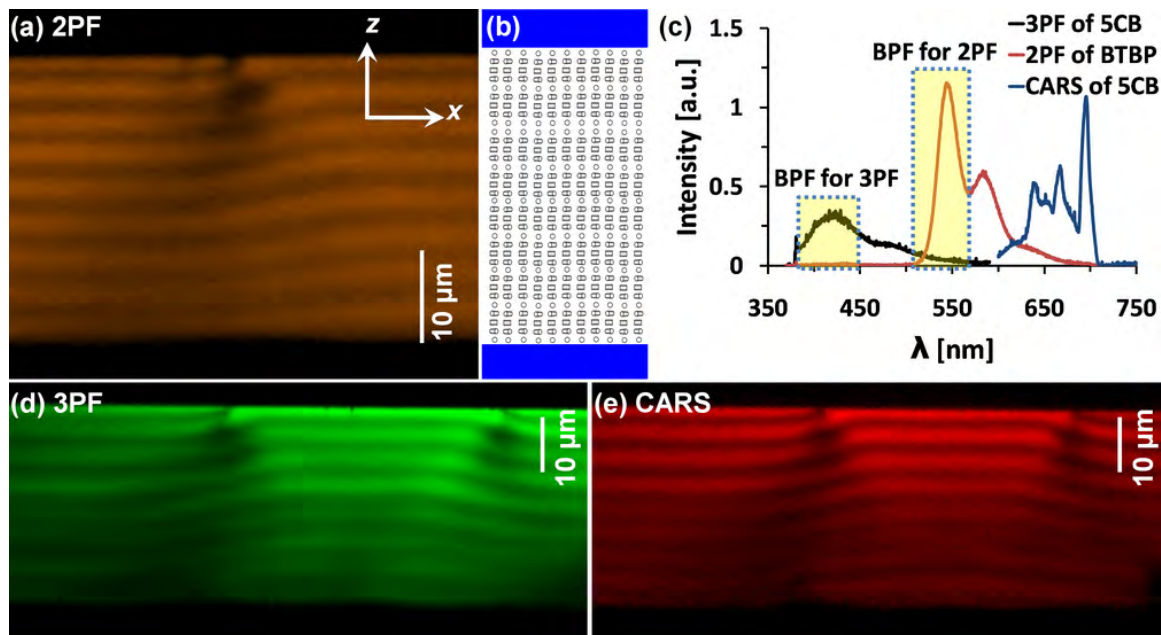


**Fig. 2.4.** Cross-sectional images of a cholesteric LC with 10 $\mu$ m pitch. (a) 2PF image of BTBP doped cholesteric for excitation at 980nm and detection with 535/50nm BPF. (b) Schematics of  $\mathbf{n}(\mathbf{r})$  in a planar cholesteric cell. (c) 2PF spectrum of the BTBP-doped cholesteric LC and 3PF and broadband CARS spectra of an unlabeled cholesteric LC. Images of labeling-free cholesteric LC obtained using (d) 3PF with 870nm excitation and detection with a 417/60nm BPF and (e) CARS-PM with excitation of 780nm pump/probe and a broadband Stokes pulses and detection with a 661/20nm BPF.

Submicron resolution of MNOPM along the optical axis is enabled by the nonlinear optical nature of the used processes and is demonstrated using vertical cross-sectional images of  $\sim 30\mu\text{m}$ -thick cells (Fig. 2.4) that have planar ground-state cholesteric structure shown in Fig. 2.4(b). 2PEF image in Fig. 2.4(a) shows such a structure with defects and is obtained for a cholesteric LC doped with BTBP [ $n,n'$ -bis(2,5-di-*tert*-butylphenyl)-3,4,9,10-perylene dicarboximide] by the use of 980nm

excitation and detection marked on the respective spectrum shown in Fig. 2.4(c). Similar co-located high-resolution images are obtained in 3PEF and CARS modalities without the use of dyes, Fig. 2.4(d,e). Image in 3PEF made is obtained via self-fluorescence of 5CB due to three photon excitation at 870nm.

CARS image is obtained with excitation using 780nm pump/probe and broadband Stokes pulses. CARS due to CN-vibration in 5CB molecules results in signal centered at  $\sim 664\text{nm}$  (CARS frequency is related to that of pump/probe and Stokes pulses as  $\omega_{\text{CARS}} = 2\omega_{\text{pump/probe}} - \omega_{\text{Stokes}}$ ). The broadband nature of CARS due to broadband Stokes from the PCF expands the capability of imaging using other spectral lines, viz., those due to  $\omega(\text{CC})$  and  $\omega(\text{CH})$  vibrations.

Figure 2.5 shows 3PEF and SHG forward-detection images of  $S_mC^*$  (Felix 015-100) in an untreated cell obtained using a 1050 nm excitation pulse (with excitation power  $\sim 1\text{mW}$ ) for two orthogonal polarizations. The ferroelectric LC molecule, on account of being noncentro-symmetric, has non-zero second order nonlinear susceptibility, which can be exploited for SHG imaging. The spectra and selecting filters corresponding to 3PF and SHG images are shown in Fig. 2.5(i,j). The in-plane images and vertical cross-sections match well for all polarizations of excitation beams. The strong SHG signal at 525nm [Fig. 2.5(i)] reveals the polar ordering and corresponding biaxial director structure of the  $S_mC^*$  phase with focal conic domains, matching that revealed by 3PF images in Fig. 2.5(a-h).

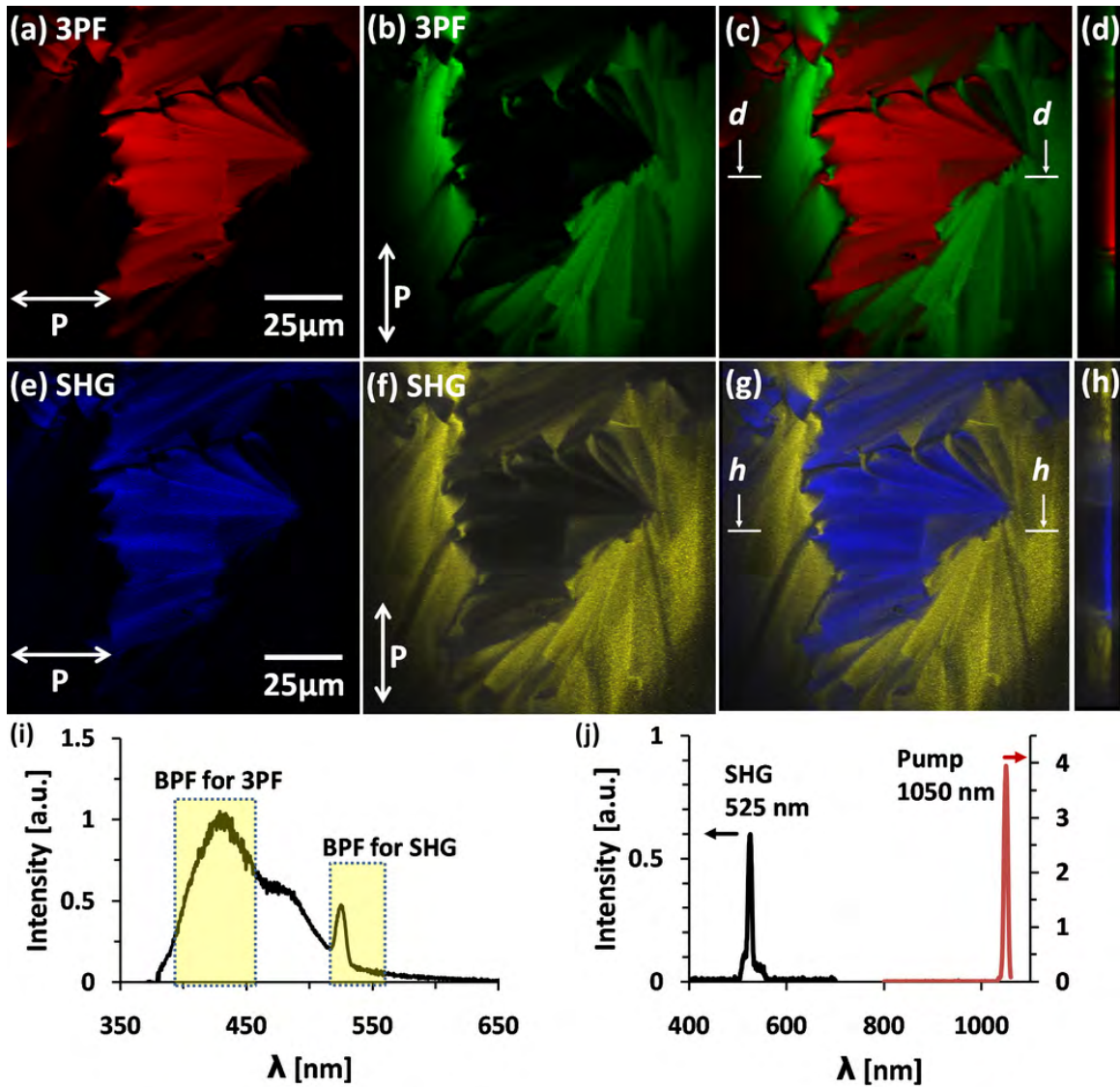


**Fig. 2.5.** Simultaneous 3PF and SHG imaging of a SmC\* LC. 3PF images first obtained separately for (a,b) two orthogonal polarizations and then superimposed for (c) in-plane and (d) vertical cross-sections. SHG images first obtained separately for (e,f) two orthogonal polarizations and then superimposed for (g) in-plane and (h) vertical cross-sections. (i) Spectra and filter selections corresponding to the images. (j) Spectra showing the excitation pulse and the generated SHG signal. 3PF and SHG signals were forward-detected using 417/60nm and 535/50nm BPFs, respectively [14].

The intensity of detected MNOPM signals depends on the angle  $\theta$  between the collinear polarizations of excitation pulses and  $\mathbf{n}(\mathbf{r})$  as  $\sim \cos^{2i}\theta$  for the detection

with no polarizers and as  $\sim \cos^{2(i+1)}\theta$  with a polarizer in the detection channel collinear with the polarizations of excitation beams, where  $i$  is the order of the nonlinear process. Imaging in 2PEF and SHG modes involves second-order nonlinear processes, whereas CARS and 3PEF are third-order nonlinear processes. Therefore, MNOPM images in all modalities have a stronger sensitivity to spatial variations of  $\mathbf{n}(\mathbf{r})$  compared to single-photon FCPM imaging. Because of the near-infrared excitation, light scattering due to the thermal fluctuations of  $\mathbf{n}(\mathbf{r})$  is relatively small and MNOPM imaging can be done for thick LC sample of thickness  $\sim 100\mu\text{m}$ , which is impossible to achieve using FCPM. Compared to the FCPM with the visible-light excitation MNOPM imaging is less affected by artifacts such as those due to light defocusing caused by LC birefringence and the Mauguin effect resulting in the light polarization following the slowly-twisting  $\mathbf{n}(\mathbf{r})$  when the twist occurs in the direction along the microscope's optical axis. It should be noted that FCPM would be unable to visualize the structure of 5CB-based cholesteric shown in Fig. 2.4 due to the Mauguin effect. The technique can potentially be extended to probe dynamic processes in LCs and LC composites associated with temporal changes of  $\mathbf{n}(\mathbf{r})$  due to application of fields and flow, similar to that recently demonstrated by using the 2PF mode of nonlinear optical microscopy and dye-doped LCs.

## 2.5 Application of HOT+MNOPM: Illustrative Examples

We demonstrate 3D manipulation and nonlinear imaging capabilities of the integrated setup by using an example of a system consisting of cholesteric LC as the host medium and colloids of spherical and anisometric (rod-like) shapes dispersed

in it. We illustrate manipulation of melamine resin (refractive index =1.68) spherical microparticles dispersed in cholesteric LCs based on nematic 5CB in a series of vertical cross-sectional images obtained in CARS and 3PEF modes, Fig. 2.6. The cell substrates are treated to provide strong planar surface boundary conditions. The particles have tangential anchoring on their surface because of which they cause distortion in the cholesteric layers. The particle-induced layer distortions depend on the particle size relative to the cholesteric pitch and the cell thickness, and are partially suppressed in the images shown by the strong tangential boundary conditions for layer orientation at the cell substrates.

In general, motion of particles perpendicular to the layers is more difficult compared to that within a layer. The HOT system allows motion of particles along the optical axis of the microscope (direction  $z$ , Fig. 2.6a), i.e., across the cholesteric layers at relatively high values of optical power ( $\sim 50$  mW, compared to  $\sim 10$  mW sufficient to move the particles laterally). Due to the high NA of the objective used, the range of movement along  $z$  attainable by HOT is limited to only a few microns. In the case of the images shown, a large range of particle displacements (tens of micrometers) along  $z$  is achieved by use of HOT in conjunction with movement of the objective along  $z$ . The resultant configurations of cholesteric layers are imaged in 3PEF, Fig. 2.6(a-c), as well as in CARS, Fig. 2.6(d-f), in a different set of similar manipulations. The 3PEF images are obtained with excitation at 870 nm and detecting the fluorescence by use of a band pass filter centered at 417 nm. The 3PEF spectrum obtained for 5CB is shown in Fig. 2.6g.

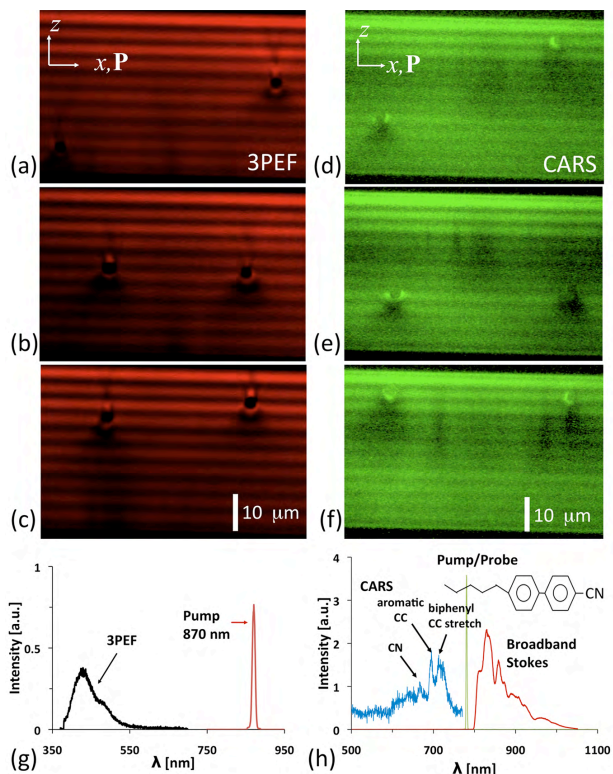


**Fig. 2.6.** Manipulation and imaging of spherical microparticles in a cholesteric LC. Images show vertical cross-sections of planar cholesteric LC cells obtained in 3PEF (a-c) and CARS (d-f) modes, displaying the cholesteric lamellae having spherical microparticles embedded within them. Particles of 4 μm diameter are optically trapped and moved within as well as across the cholesteric layers. The nonlinear signals are collected in the forward direction with a BPF 417/60 for 3PEF and a BPF 661/20 for CARS of CN stretching vibration of 5CB. (g) shows the excitation and the fluorescence spectra of 3PEF for 5CB. (h) shows the broadband Stokes, the pump/probe at 780 nm and the broadband CARS spectrum obtained from the LC with different peaks in the CARS spectra marked to indicate the corresponding Raman vibration. The molecular structure of 5CB is shown in the inset.

For the set of wavelengths used for pump/probe (780 nm) and Stokes (broadband), the CARS images due to CN stretching vibration are obtained for the signal centered at approximately 664.7 nm, which is selected by a BPF 661/20 nm. Multiple vibrational modes of the molecule can be probed simultaneously because of the use of a broadband Stokes pulse, all of which show up in the CARS spectrum, as seen in Fig. 2.6h (molecular structure of 5CB is shown in the inset). Thus we

obtain the full CARS spectral information about the material and can select a particular vibration of interest for imaging.

The shape anisotropy of microparticles dispersed in LCs lends to them interesting trapping behavior and self-assembling properties. We use such a soft-matter system of GaN nanorods ( $n_{\text{GaN}} \approx 2.3$ ) dispersed in cholesteric LC to illustrate the capabilities of the integrated HOT and MNOPM setup [77,78]. The GaN nanorods tend to align parallel to the local  $\mathbf{n}(\mathbf{r})$ , as they set tangential alignment for the LC molecules. In a cholesteric LC, they are therefore parallel to the cholesteric layers. This allows them to be used effectively as probes of  $\mathbf{n}(\mathbf{r})$ . GaN has a Wurtzite non-centrosymmetric crystal structure and hence generates a strong second-harmonic response dependent on the relative orientation of the nanorod to the polarization of the incident radiation – thus enabling their facile polarization-dependent nonlinear imaging. Figure 2.7 shows this combined nonlinear imaging, e.g., in Fig.2.7(a,b), the LC is imaged in 3PEF and a pair of nanorods in SHG mode. Figure 2.7(c) shows the overlapping spectra of the 3PEF signal from LC and the SHG peak from the nanorods (at 435 nm) for excitation beam at 870 nm; both are simultaneously collected by use of the same BPF 417/60 nm. Figure 2.7(d,e) shows similar set of images obtained with the LC imaged in CARS and the nanorods in SHG mode. It is clear from the cross-sections, Fig. 2.7(b,e), that the nanorod aligns parallel to the layers. The apparently increased thickness of the nanorod in the cross-sectional images is due to its thermal diffusion over the signal-integration period and also because of the diffraction-limited spatial resolution.

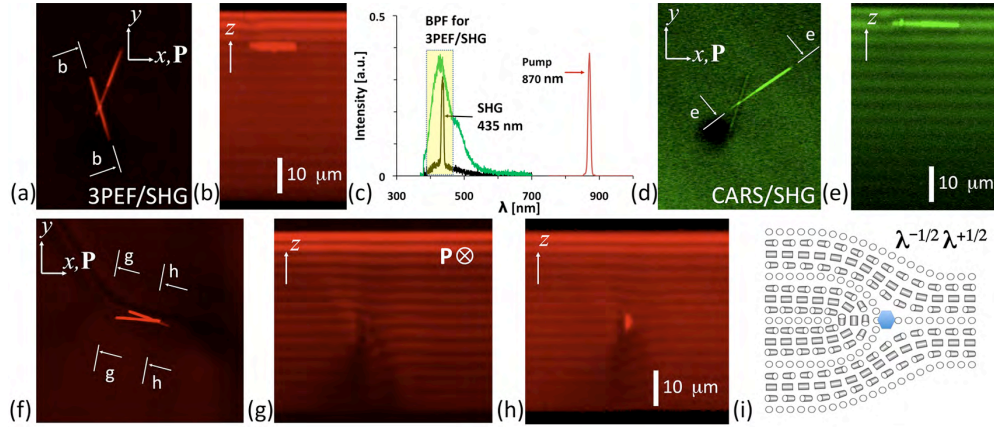


**Fig. 2.7.** 3D Imaging of GaN nanorods dispersed in a cholesteric LC. GaN nanorods are manipulated in the layered structure of the cholesteric LC and the LC-nanorod composite is imaged in its lateral plane as well as in the vertical cross-section in two nonlinear modes: the LC is probed using 3PEF (a, b) and CARS (d, e) and the nanorods are visualized in SHG. (c) shows the spectrum with the excitation at 870 nm and the 3PEF emission from the LC molecules and SHG (at 435 nm) from the GaN nanorods. The nanorods interacting with a cholesteric dislocation are imaged in 3PEF (f-h). (g) shows 3PEF image of a dislocation comprising  $\lambda^{+1/2}$  and  $\lambda^{-1/2}$  disclinations in its vertical cross-section. The schematic diagram of the molecular director pattern around the dislocation with the position of the nanorod embedded in it is shown in (i).

Here we show a nanorod weakly interacting with a dislocation with Burgers vector  $|\mathbf{b}| = b = p$ , having its core split into two nonsingular disclinations,  $\lambda^{-1/2}\lambda^{+1/2}$  (see Appendix II for a discussion of classification of defects in cholesteric LCs) Figure 2.7(f) shows a nanorod aligned parallel to the dislocation with core shown in a vertical cross-section in Fig. 2.7(g). The nanorod is also aligned along the core of the defect line shown in the cross-section in Fig. 2.7(h). The schematic representation of the director structure forming the dislocation and the position of the nanorod embedded in it is shown in Fig. 2.7(i).

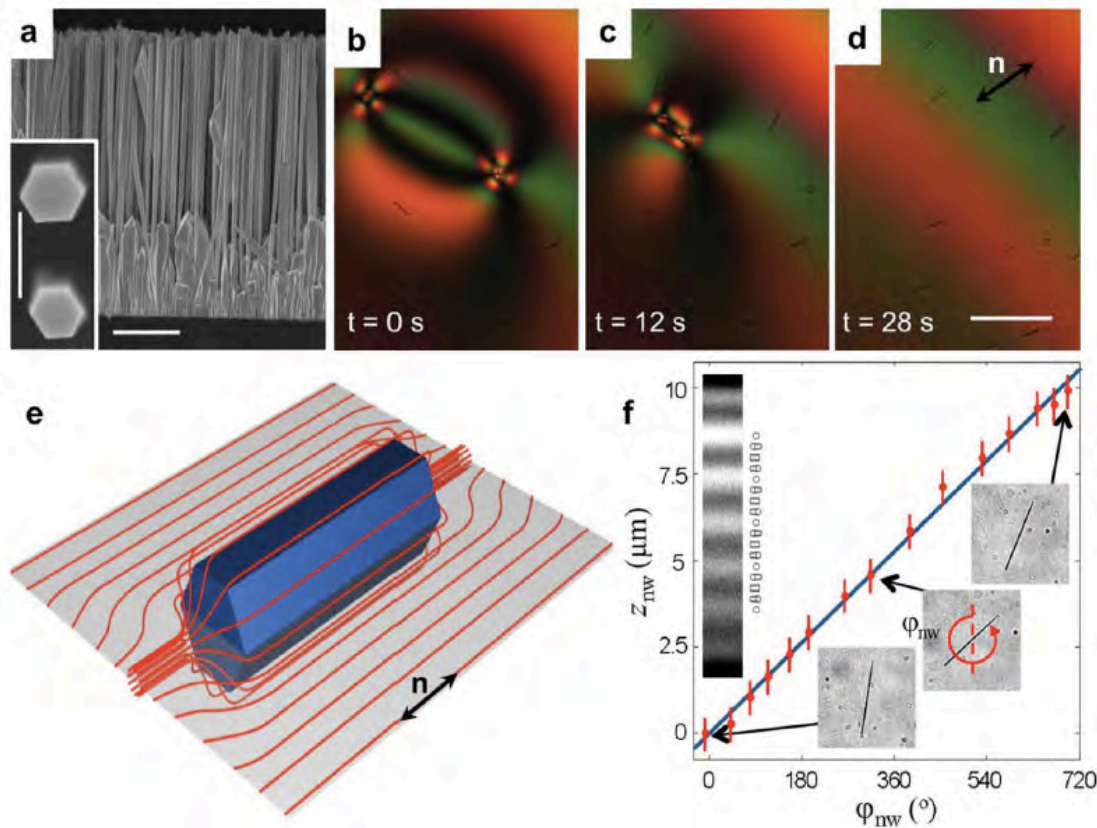


**Figure 2.8.** Nanorods as nanoscale probes of the long-range molecular alignment in LCs. (a) SEM micrographs showing GaN nanorods as grown on a thin AlN buffer layer on a Si(111) substrate. The inset in a, shows that nanorods have hexagonal cross-sections. (b,c,d) Polarizing optical microscopy textures showing that the nanorod orientations visualize temporal evolution of  $\mathbf{n}(\mathbf{r})$  as nematic defects annihilate; the elapsed time and the resulting uniform orientation of  $\mathbf{n}(\mathbf{r})$  are marked on the images. (e) Schematics of the structure around the GaN nanorods in the LC with the uniformly-aligned far-field  $\mathbf{n}(\mathbf{r})$ . (f) Vertical nanorod position  $z_{rod}$  along the helical axis is a linear function of  $\phi_{rod}$  matching that of the ground-state helicoidal structure (solid line). The reading error of  $\pm 0.5 \mu\text{m}$  is shown by error bars.

The characteristic alignment of nanorods dispersed in LCs to orient along  $\mathbf{n}(\mathbf{r})$  of the equilibrium helicoidal structure, Fig. 2.8f, results in a coupling of its rotation with translation along the helical axis of the cholesteric LC. For optical manipulation, one or two laser traps are positioned at the ends of a nanorod that are then used to rotate and move it in 3D. The handedness of the helix and the rotation direction determine whether the rod moves upward or downward; its translation

away from the microscope objective is easier than toward it, due to the scattering forces originating from the large rod-CLC refractive index mismatch. The measured vertical position  $z_{nw}$  of a nanorod along the helix is a linear function of its in-plane orientation angle  $\phi_{nw}$  (Fig. 1f), consistent with the  $\mathbf{n}(\mathbf{r})$  of the equilibrium helicoidal structure. From the linear fit by  $z_{nw} = \phi_{rod} \cdot p / (2\pi)$ , the measured effective pitch is  $p = 5.3 \pm 0.3 \mu\text{m}$ , matching that obtained from the FCPM cross-section in the same location (inset Fig. 2.8f).

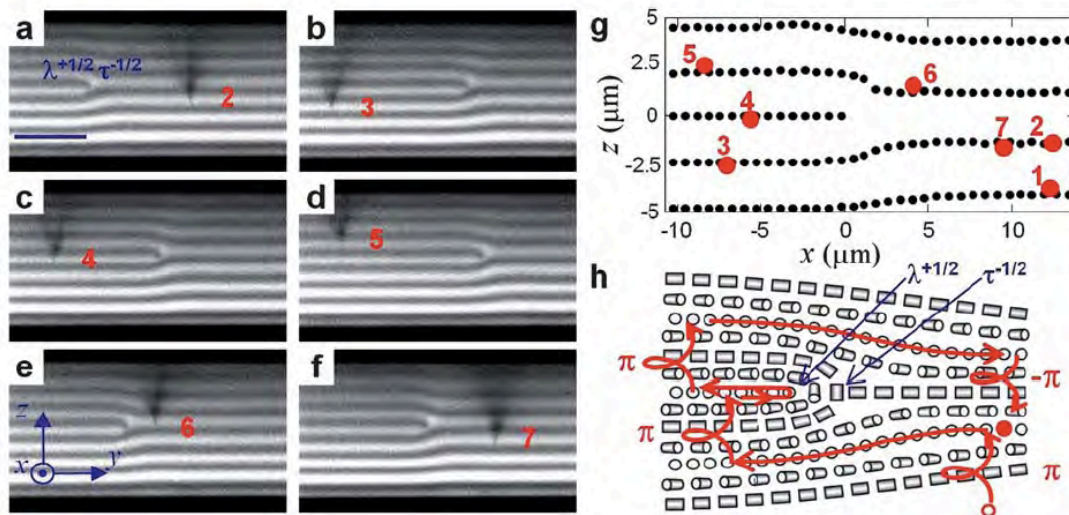


**Figure 2.9** Probing the Burgers vector and structure of a  $b=p/2$  dislocation with core split into the  $\lambda^{+1/2}\tau^{-1/2}$  pairmark  $\lambda$  &  $\tau$  in the figure. (a-f) Direct probing of Burgers vector by sequential translation of the nanorod along a Burgers circuit that includes points 2-7 in (a-f): (a) starting position at the point #2; (b) the nanorod was continuously translated beneath the dislocation to the new location #3 and then (c) rotated  $180^\circ$  CCW with the corresponding translational shift upward for one cholesteric layer; pushing nanorod to the right on the image revealed that the layer is discontinuous and location of the dislocation core; (d) the rod was rotated  $180^\circ$  CCW again while shifting one layer upward; **e**, the nanorod was moved above the dislocation to the position # 6 and then (f) rotated  $180^\circ$  CW while shifting one layer downward and closing the Burgers circuit (g) Layers displacement around the edge dislocation and nanorod positions corresponding to a-f (red filled circles). (h) Schematics of the visualized core structure of the  $b=p/2$  dislocation with the Burgers circuit and core probing nanorod trajectory (red) around the defect line.

Furthermore, this coupling between rotation and optical translation of the nanorod enables its use as a probe for visualization of the CLC layer displacements and the layered structures. Figure 2.9 shows how an optically manipulated nanorod probes the Burgers vector and core structure of such an elementary dislocation. A combination of rotational and translational motion along the so-called Burgers circuit (Fig. 2.9) reveals the Burgers vector's magnitude  $|\mathbf{b}| = b = p/2$  and that the dislocation core is split into a  $\lambda^{+1/2}\tau^{-1/2}$  pair (Fig. 2.9h). Core structures and reconstructed layer profiles (Fig. 2.9g) match those obtained from the FCPM images (Fig. 2.9a-f).

## 2.6 HOT+MNOPM: Discussion

Optical manipulation has proved to be a tool of immense utility in quantifying elasticity-mediated colloidal interactions [80-82], controlling particle dynamics [83], measuring tension of defect lines in LCs [84-86], and manipulation based on director reorientation under an optical trap [87-89]. Optical tweezers based on acousto-optic deflectors and scanning galvanomirrors allow for measurement of these forces, which are typically probed only within the microscope's lateral plane. HOT extends these capabilities of optical tweezers to facilitate manipulation along the microscope's axial direction as well. Combining HOT with high-resolution 3D multi-particle tracking system enables precise real-time 3D localization of the trapped colloids. This helps determine the map of interaction forces exerted on each particle in 3D [90]. In addition to 3D

manipulation capabilities, HOT allows for generation of beams with phase singularities, which play an important role in controlling the LC defects. Optical trapping has been previously combined with nonlinear imaging by performing both the tasks using the same pulsed-laser – the laser beam that traps the object can be used to simultaneously image it in a nonlinear modality such as two-photon fluorescence, Raman micro-spectroscopy, or broadband supercontinuum CARS. Although these integrated trapping and imaging techniques have been widely useful in biophysics [91], they do not allow orientational imaging of long-range molecular patterns that are critically important when performing such manipulation in anisotropic LC fluids.

Even though FCPM has been successfully integrated with optical manipulation and used to image LC director patterns, it requires doping LCs with specific dyes. For some LC imaging applications, it is hard to find a suitable dye that would align both excitation and fluorescence transition dipoles along  $\mathbf{n}(\mathbf{r})$ . Moreover, to image biaxial LCs with FCPM, one would be required to use different dye molecules aligning along the different biaxial directors [92], while MNOPM can perform such imaging by selecting appropriate chemical bonds of the constituent molecules.

FCPM imaging of LCs with twisted configurations of  $\mathbf{n}(\mathbf{r})$ , with the helical axis parallel to the microscope's axis is difficult, because the polarization of the imaging light follows the twist of  $\mathbf{n}(\mathbf{r})$  as it propagates through the LC. This so-called Mauguin effect is quantified by the Mauguin parameter,  $\eta_{Mauguin} = p\Delta n/2\lambda$ , where  $p$  is the pitch of the twist in  $\mathbf{n}(\mathbf{r})$  structure being imaged,  $\Delta n$  is its birefringence and  $\lambda$

is the wavelength of imaging light. Values of  $\eta_{Mauguin} \gg 1$  are detrimental to imaging and preclude the reconstruction of  $\mathbf{n}(\mathbf{r})$ . MNOPM partially mitigates this issue, as it uses longer wavelengths in the near-infrared range. The use of longer excitation wavelengths in MNOPM imaging also helps improve the penetration depth inside the sample compared to FCPM. Defocusing because of scattering due to fluctuations of  $\mathbf{n}(\mathbf{r})$  is also less severe for longer wavelengths.

The strength of the MNOPM approach is fully realized when employed to study composite soft-matter systems with some of the constituents exhibiting long-range orientational order, such as LC colloidal dispersions. The PCF based implementation of broadband CARS [93] and other imaging modalities makes our system cost-effective compared to other implementations [94] because only one laser is used to generate all the needed excitation pulses. Furthermore, CARS imaging with a broadband Stokes pulse enables imaging over a broad spectral range ( $\sim 800 - 3500 \text{ cm}^{-1}$ ), probing multiple vibration states at the same time. The integration of HOT with MNOPM greatly enhances the capabilities in optical control and characterization of soft-matter systems in an unprecedented manner, as both the components of the integrated system work simultaneously yet independently of each other.

There are several artifacts one needs to be cautious about while imaging LCs. As discussed earlier, nonlinear imaging techniques mitigate the Mauguin effect because the excitation wavelengths are longer, but the imaging quality can still be adversely affected when LCs with high birefringence and very slowly twisting director are imaged. Another artifact that requires attention is unintended light

induced realignment of  $\mathbf{n}(\mathbf{r})$  by the imaging beam – the optical Freederickz transition. Optical realignment occurs above a certain threshold laser power determined by the cell thickness and the birefringence of the material. This limits the maximum intensity that can be used to image LCs and hence ultimately sets a limit on the speed of imaging. The optical forces exerted by the imaging beam on the colloidal particles or director structures can be a significant source of unintended optical manipulation when high optical power and slow rate of beam scanning are used. For the imaging reported here, the optical power at the sample is small enough (combined power < 2 mW) so that effects due to the optical Freederickz transition as well as those due to optical forces are negligible.

Similar artifacts may also adversely affect optical manipulation in LCs. In addition, sample heating by the trapping beam may change the pitch of the cholesteric LC being studied, cause local convective flows, or locally induce phase transition. Therefore it is critical to ensure that the LC and the particles being manipulated have negligible absorption at the trapping wavelength. Optical manipulation in LCs is further complicated by the fact that they are birefringent turbid media. Birefringence causes defocusing and depolarization as the beam is focused deep into the sample. Due to the optical anisotropy of LCs, trapping in LCs is polarization dependent and therefore depolarization can affect force measurements. Light scattering due to thermal fluctuations of  $\mathbf{n}(\mathbf{r})$  also reduces trapping efficiency. These effects due to birefringence, turbidity and the optical aberrations along the optical path can be accounted and compensated for in real-time with the same SLM used to generate the laser trap patterns [95].

## 2.7 Summary

The combined capabilities of labeling-free 3D optical imaging in CARS, 3PEF, SHG and other nonlinear optical modes, with non-contact 3D optical manipulation facilitate the design of novel composite soft-materials and chemical-sensitive characterization of the underlying self-organization processes. The application of the integrated system can be extended to the study of multitudes of other soft-matter systems involving nanoparticles, lipids, DNA and other biological materials-based LCs, polymer dispersed LCs, etc. These soft-matter systems form the basis for novel materials with intriguing mechanical properties (artificial muscles, materials with electro-optically controlled elasticity, high-strength fibers, etc.) and photonic applications (metamaterials, LC-based tunable lasers, etc.). The integrated system has immense potential in molecular and cellular biology, e.g., in determining the mechanism behind how lipid membranes organize into complex-shaped organelles [96], in tracking cellular processes such as metabolism by imaging different components of the cell in different nonlinear modalities. Furthermore, the diffraction limit in imaging can be overcome by combining MNOPM with near-field scanning technique.

## 2.8 Appendix I: Material Preparation

LC samples are prepared between two glass substrates of  $\sim 170 \mu\text{m}$  thickness. The sample thickness is set by sandwiching silica microspheres with diameter 15 – 60  $\mu\text{m}$  between these glass plates as they are sealed together by glue. The surface

boundary conditions for the LC molecules on the glass substrates are set as follows: (a) treating the substrate with 2% by weight aqueous solutions of N,N-dimethyl-n-octadecyl-3-aminopropyl-trimethoxysilyl chloride (Sigma Aldrich) sets  $\mathbf{n}(\mathbf{r})$  perpendicular to the surface; (b) coating the substrate with polyimide (e.g., PI-2555, HD Microsystems) and rubbing the coated layer anchors the  $\mathbf{n}(\mathbf{r})$  at the surface along the rubbing direction. A room-temperature nematic LC, 5CB (4-pentyl-4'-cyanobiphenyl, Frinton Labs), ZLI-2806 (EM Chemicals), etc., is doped with a chiral agent CB-15 (EM Chemicals) or cholesteryl pelargonate (Sigma-Aldrich). The resultant pitch  $p$  of the cholesteric LC is determined by controlling the concentration of the chiral dopant in it and the strength of the chiral dopant in a particular nematic host, called the helical twisting power ( $H_{\text{HTP}}$ ). The pitch  $p$  is related to the dopant concentration as . The cholesteric LCs chosen for the experiments described in this article have a pitch in the range from 2  $\mu\text{m}$  to 20  $\mu\text{m}$ .

A dispersion of microparticles is prepared in the cholesteric LC as follows. (a) Melamine resin spherical particles of 2, 4, 8  $\mu\text{m}$  in diameter (obtained from Fluka) are used as particles which provide tangential anchoring on their surfaces. First, a powder is obtained from their aqueous solution by evaporating the water. The mixture of this powder and LC is sonicated to break apart colloidal aggregates. (b) To get homeotropic anchoring on particles, silica particles of diameter 2, 4  $\mu\text{m}$  (obtained from Sigma Aldrich) are treated with 2% by weight aqueous solutions of N,N-dimethyl-n-octadecyl-3-aminopropyl-trimethoxysilyl chloride. Solvent transfer is performed by centrifuging the particle dispersion four to five times and replacing water with isopropanol. This isopropanol based silica particle dispersion is added to

LC and the solvent is evaporated. Finally the LC-particle mixture is sonicated to break apart particle aggregates. (c) We also use Gallium Nitride (GaN) nanorods doped into the cholesteric LC as anisometrically shaped probes for LC manipulation and imaging. The nanorods are  $\sim 10 \mu\text{m}$  in length and have a hexagonal cross-section with  $\sim 150 \text{ nm}$  edge sides. The nanorods are doped with Si such that the free-carrier concentration is around  $1 \times 10^{18} \text{ cm}^{-3}$ . At these doping densities, the optical absorption at  $1064 \text{ nm}$  is sufficiently low ( $\sim 80 \text{ cm}^{-1}$ ) so that heating of the LC while the rods are manipulated with focused laser beams is negligible. The long axis of the nanorods is along the c-axis (0001) of their Wurtzite crystal structure, with the sidewalls being m-planes [(1 -1 0 0) family], producing the hexagonal cross-section. The nanorods are first dispersed in isopropanol and then transferred into the LC by mixing and letting isopropanol evaporate by heating the mixture to  $\sim 60 \text{ }^\circ\text{C}$ .

## 2.9 Appendix II: Material Properties

Material/Property	$K_{11}$ , pN	$K_{22}$ , pN	$K_{33}$ , pN	$n_e$	$n_o$	$\Delta n$
MLC-6609	17.2	7.51	17.9	1.551	1.473	0.078
ZLI-3412	14.1	6.7	15.5	1.558	1.479	0.079
ZLI-2806	14.9	7.9	15.4	1.518	1.475	0.043
5CB	6.4	3	10	1.714	1.536	0.178
AMLC-0010	17.2	7.51	17.9	1.55	1.47	0.08
E7	11.1	6.4	17.1	1.746	1.521	0.225

## 2.10 Appendix II: Classification of Defects in Cholesteric Liquid Crystals

The disclinations are classified according to the scheme of Kleman and Fridel [31]. In the  $\lambda$  disclinations, the material  $\mathbf{n}$ -director field is non-singular because  $\mathbf{n}$  is parallel to the defect line in its core, so that the singularity is observed only in the immaterial director fields  $\boldsymbol{\chi}$  (along the helical axis) and  $\boldsymbol{\tau}$  orthogonal to both  $\mathbf{n}$  and  $\boldsymbol{\chi}$ . In the  $\tau$  - disclinations, the  $\boldsymbol{\tau}$  -field is non-singular but  $\mathbf{n}$  and  $\boldsymbol{\chi}$  director fields are singular. In  $\chi$  -disclinations, the singularities are found in both  $\mathbf{n}$  and  $\boldsymbol{\tau}$  director fields but not in the  $\boldsymbol{\chi}$ -field.

Topological defects in a medium with broken translational symmetry are dislocations. Cholesteric LCs, on account of their lamellar structure can be thought of as having broken the translational symmetry along the helical axis. The edge dislocations observed in cholesterics are split into two disclinations of strength  $\pi$  (i.e., magnitude of charge  $\frac{1}{2}$ , oppositely charged to conserve the total topological charge). A  $\tau^{\pm 1/2}$  and a  $\lambda^{\pm 1/2}$  disclination combine to form a dislocation with magnitude of its Burgers vector,  $|\mathbf{b}| = p/2$ . Two  $\lambda$ -disclinations comprise a  $|\mathbf{b}| = p$  dislocation. We show in Fig. 2.S1 three resultant different types of edge dislocations:  $\lambda^{+1/2}\tau^{-1/2}$ ,  $\tau^{+1/2}\lambda^{-1/2}$ , and  $\lambda^{+1/2}\lambda^{-1/2}$ .

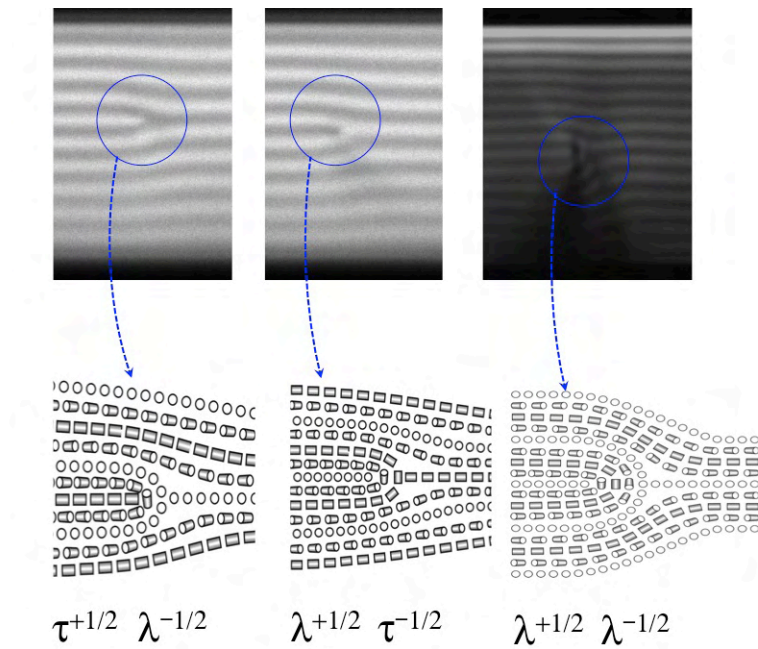


**Fig. 2.S1.** Dislocations in Cholesteric LC. We show three different types of edge dislocations in their vertical cross-sectional plane. (a)  $\lambda^{+1/2}\tau^{-1/2}$  dislocation with  $|\mathbf{b}| = p/2$  (b)  $\tau^{+1/2}\lambda^{-1/2}$  dislocation with  $|\mathbf{b}| = p/2$  (c)  $\lambda^{+1/2}\lambda^{-1/2}$  dislocation with  $|\mathbf{b}| = p$ .

## Chapter 3

### Optical Generation of Defects

#### 3.1 Introduction

Control of structures formed by molecular ordering in LCs lays the ground for technological applications such as displays, liquid crystal biosensors, distributed feedback lasers, and beam steering devices. In addition to controlled generation, deterministic and reproducible multistable switching of these structures of molecular alignment is critical for robust functionality of these applications. In this chapter, I describe facile optical creation and multistable switching of localized configurations of molecular orientation field in confined chiral nematic LC (CNLC). These localized particle-like excitations dubbed “Torons” [97] are generated by focused laser beams and are shown to embed twist-deformations in three dimensions, into a background of uniform molecular alignment. Their structures are studied with the help of confocal polarizing microscopy, revealing therein a manifestation of both skyrmion-like and Hopf fibration features. Skyrmions are an important class of nonlinear excitations, found in various other systems such as chiral helimagnets, and their detailed visualization and understanding is important from fundamental perspective in understanding discrete excitations in continuous fields in condensed matter and particle physics [98,99]. Finally, I discuss various

other types of localized defect structures, which, along with the Toron, form a wide class of optical excitations in CNLCs.

### 3.2 Structure of Torons

Because of its propensity for twisting upon addition of chiral dopant to nematic phase, the resultant CLNC assumes a ground state with twisted molecular arrangement, viz., cholesteric phase or blue phase. These ground-state structures can be suppressed by application of external fields or by incompatible surface anchoring, rendering the CNLC uniform and thus frustrated with respect to its preference for twist. This frustration, however, can be relieved locally, and I present here several particle-like excitations in  $\mathbf{n}(\mathbf{r})$  dubbed “Torons”, enabling reappearance of twist that was initially rendered uniform. Torons can be optically generated in a highly controlled manner at a selected place. They are then structurally characterized with full detail in 3D with the help of FCPM. The basic Toron configuration is a double twist cylinder closed on itself in the form of a torus (Fig. 3.1a) and coupled to the surrounding uniform field by point or line topological singularities (Fig. 3.1b-f). Remarkably, Torons enable twist in all three dimensions and are stabilized by strong elastic energy barriers associated with nucleation of topological defects.

CNLC of equilibrium helical pitch  $p$  is confined into a cell of thickness  $d$  with the inner surfaces of glass plates treated to provide homeotropic anchoring. These boundary conditions are incompatible with the ground-state cholesteric twist and tend to unwind twisted structures forcing a uniform bulk alignment.

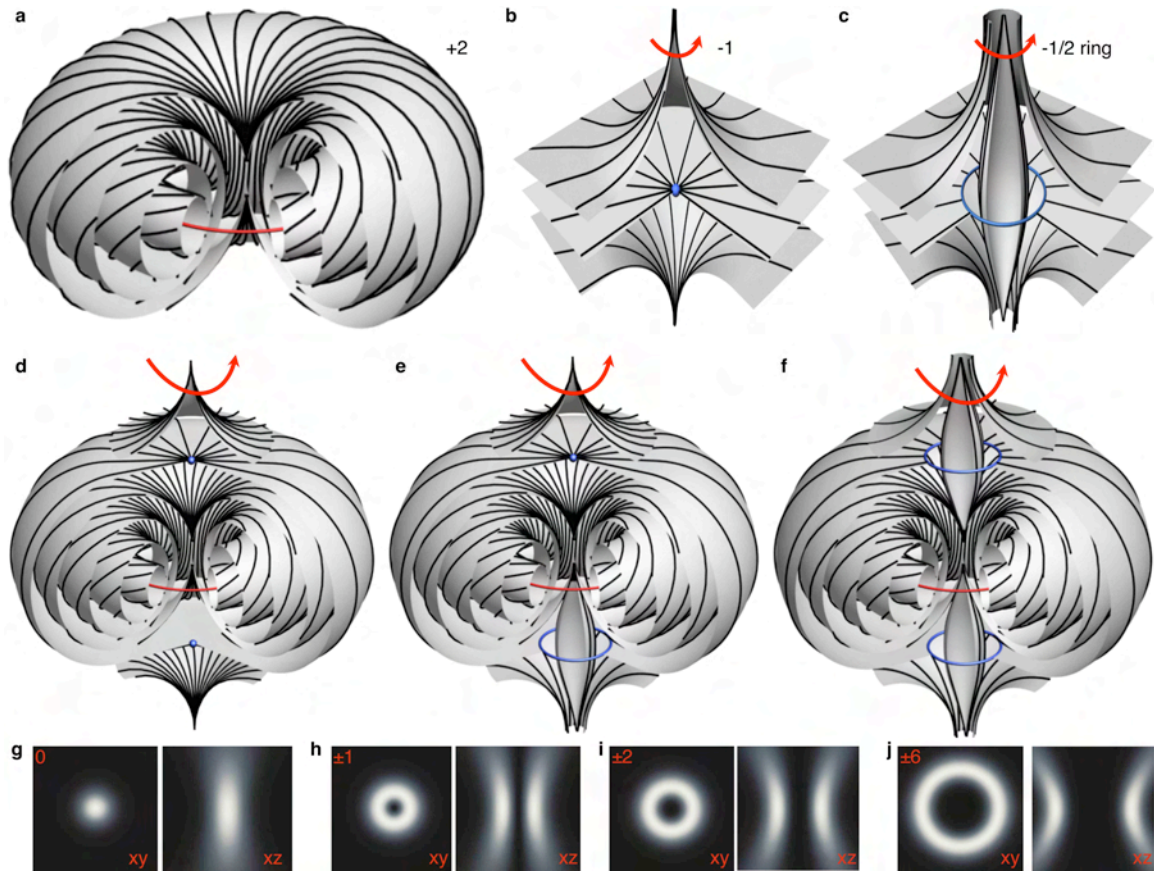


**Fig. 3.1.** Triple Twist Toron field configurations generated by LG beams and embedded into a uniform field by defects. (a) Toron structure with the topological charge “+2” due to the twist-escaped nonsingular disclination ring of strength  $s=+1$  shown by the red line. (b) “-1” hyperbolic point defect and (c) a ring of  $s=-1/2$  disclination topologically equivalent to a “-1” point defect, both exhibiting twist of  $\mathbf{n}(\mathbf{r})$  with the sense of twist shown by red arrows. (d) T3-1 configuration with the Toron accompanied by two hyperbolic point defects. (e) T3-2 structure containing a point defect and a disclination ring. (f) T3-3 configuration with two  $s=-1/2$  defect rings. (g-j) light intensity distributions in the lateral  $xy$  (left) and axial  $xz$  (right) planes of the LG beams of topological charge marked for each of the image pairs; the square cross-sections are  $4 \mu\text{m}$  wide.

The helical structure is unwound (nematic-like) when the cell gap is much smaller than the pitch ( $p \gg d$ ), while for larger cell gaps ( $p \ll d$ ), the director can twist freely in the center of the sample and meet the vertical boundary conditions at the glass plates. The condition for generation of Torons occurs at  $d/p \approx 1$ . Laguerre-Gaussian (LG) beams of charge  $l = 0 - \pm 10$  and intensity distributions in the lateral

and axial planes shown in Fig. 3.1(g-j) are focused into the bulk of unwound CNLC typical  $d/p = 0.75-1.1$ . When the laser power is increased above a certain threshold value  $P_{th} = 30-50$  mW, the beam rotates the local  $\mathbf{n}(\mathbf{r})$  along its polarization direction, inducing a distortion (due to the positive dielectric anisotropy of the LC used). This initial distortion disappears within 5-10 ms upon turning off the laser. However, if the laser power is increased above the second threshold  $P > (1.2-2.2) \cdot P_{th}$ , this distortion transforms into one of the Toron structures, which persists even after the laser is switched off. The generated Torons are embedded in a sea of uniform  $\mathbf{n}(\mathbf{r})$  and have a characteristic size  $\approx p$  in all directions. 3D images and cross-sections obtained by FCPM in different linear and circular polarizations of excitation laser, such as those shown in Fig. 3.2, enable reconstruction of  $\mathbf{n}(\mathbf{r})$  for the observed three distinct types of Torons, Fig. 3.1d-f.

The structure that emerges is a double-twist cylinder looped on itself. In the toroid's midplane, the structure is skyrmion-like as the director at the center is vertical and twists by  $180^\circ$  radially, matching the vertical far field  $\mathbf{n}(\mathbf{r})$ . The  $\mathbf{n}(\mathbf{r})$  is tangent to the circular axis of the toroid and rotates in all directions when moving away from it (Figs. 3.1-3.3). The uniformly-twisted field lines of  $\mathbf{n}(\mathbf{r})$  on a family of nested tori resemble the stereographic projection of the Hopf fibration [100], while being localized in a finite-volume of space because of the presence of defects embedding the Toron into a uniform field. Mapping the director field at the toroid surfaces into the order parameter space of the CNLC covers the sphere twice and implies that the topological charge of the Toron structure is +2, suggesting that defects of opposite charge are needed to embed it into the uniform field.

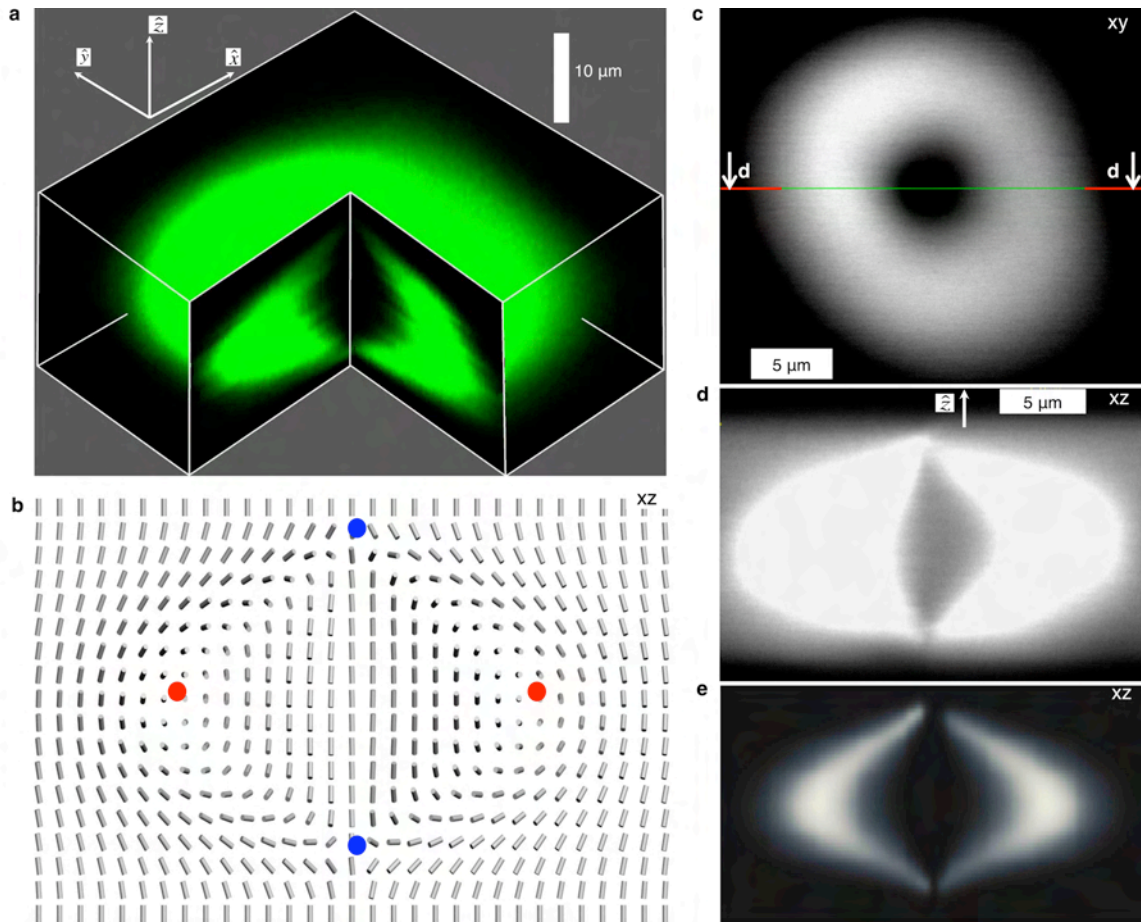


**Fig. 3.2.** FCPM imaging and computer simulations of laser-generated Torons. (a) Three-dimensional image of the T3-1 configuration obtained using FCPM with circularly polarized probing light. (b) Vertical cross-section of the  $\mathbf{n}(\mathbf{r})$  of corresponding three-dimensional T3-1 structure obtained by numerical minimization of the elastic free energy; blue circles denote the hyperbolic point defects and the red ones show the twist-escaped disclination intersecting the plane of the cross-section. (c) In-plane FCPM cross-section passing through the central plane of the T3 structure and containing the circular axis of the torus; the red bars indicate the location of the vertical cross-section. (d) Experimental vertical FCPM cross-section and (e) corresponding computer-simulated FCPM texture obtained for circularly-polarized probing light and the equilibrium director field shown in (b). The confinement ratio is  $d/p=1$  in both the experiments and the simulations.

Indeed, FCPM imaging (Figs. 3.2-3.4) reveals that the orientational order within the localized Toron structures is locally broken on topological defect points (Fig. 3.1b) or ring-shaped lines (Fig. 3.1c), depending on the type of structure

formed. CNLC disclinations are often observed “escaping in the 3<sup>rd</sup> dimension” via twist to avoid singularity in  $\mathbf{n}(\mathbf{r})$  in their core. The Toron contains such a twist-escaped ring of disclination of charge +1 (red line in Fig. 3.1a) (the  $s=+1$  defect ring is equivalent to a +2 point defect). The director field of the Toron is matched to the surrounding uniform alignment by introducing defects of total charge -2 such as the -1 hyperbolic point defects (Fig. 3.1b, Fig. 3.3) or -1/2 disclination ring (Fig. 3.1c).

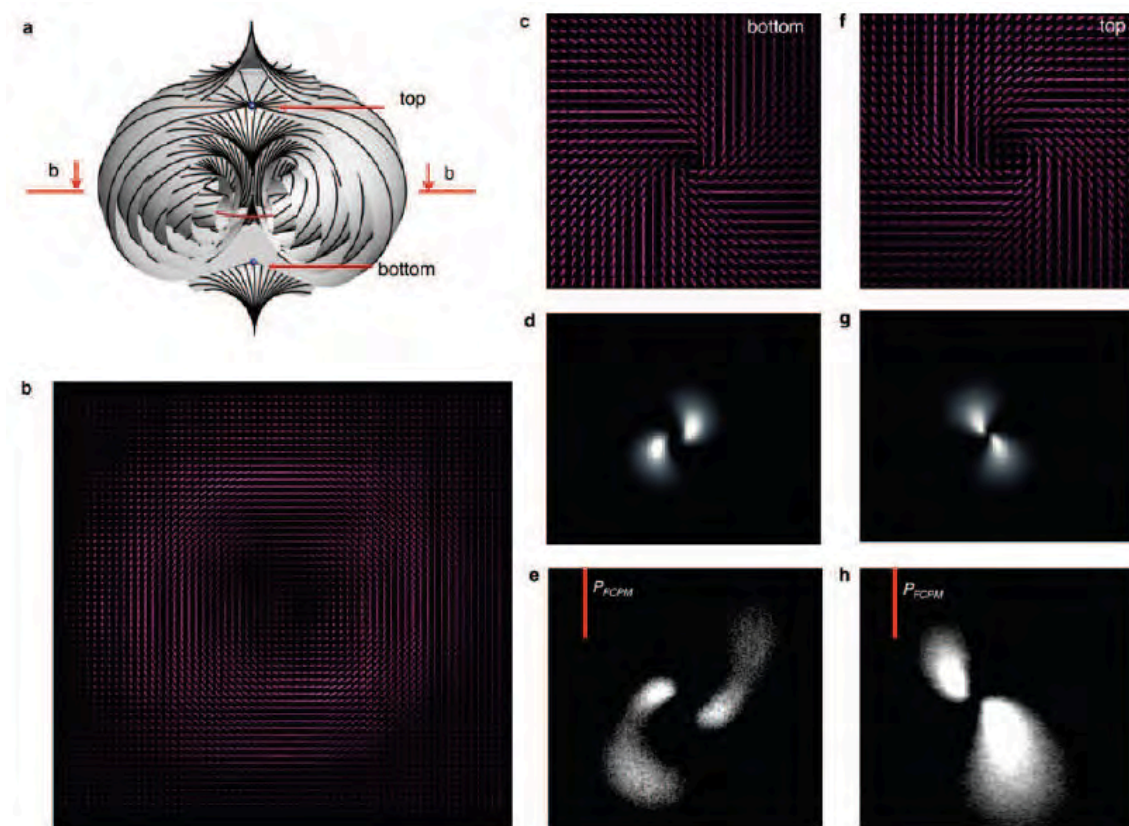


**Fig. 3.3.** Computer simulations and FCPM imaging of in-plane cross-sections of T3-1 Toron. (a) Schematic representation of the T3-1 structure with the hyperbolic point defects shown by blue dots and the twist-escaped non-singular disclination ring shown by a red line. (b) Computer simulated  $\mathbf{n}(\mathbf{r})$  in the central plane b-b cross-section shown in (a) of the T3-1 structure containing the disclination ring. (c,f) In-plane cross-sections of  $\mathbf{n}(\mathbf{r})$  in the vicinity of point defects near the bottom plate, (c) and the top plate (f). (d,g) Corresponding simulated and (e,h) experimental FCPM textures. The red bars in (e) and (h) indicate the FCPM linear polarization states.

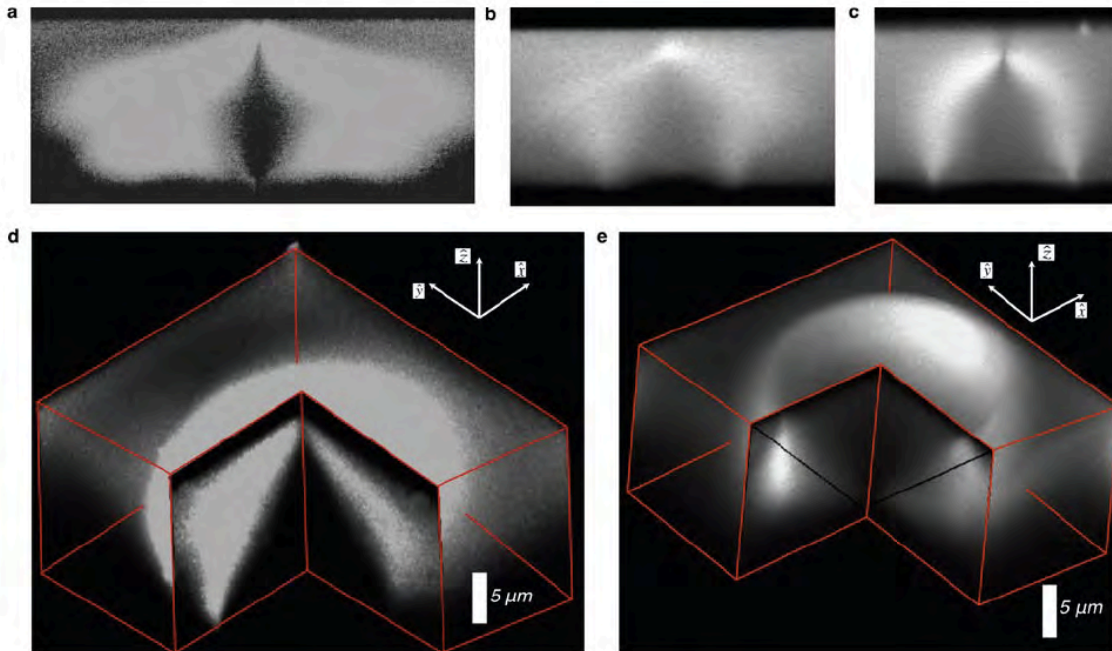


**Fig. 3.4.** FCPM imaging of the T3-2s with different locations and diameters of disclination rings. (a-c) FCPM vertical cross-sections of three different T3-2s in a cell of thickness  $d = 15 \mu\text{m}$  with different diameters of the disclination ring at the bottom surface. (d,e) 3D FCPM images of the T3-2 structures having the disclination rings (d) at the bottom and (e) at the top surface.

### 3.3 Controlled Generation of Torons

Different defect-proliferated Torons can be induced next to each other as shown in Fig. 3.5a: T1 with two hyperbolic -1 point defects shown by the blue dots in Fig. 3.1d, T2 with combinations of line and point defects such as the one in Fig. 1e, and T3 with two  $-1/2$  disclination rings shown by blue lines in Fig. 3.1f. Since the  $-1/2$  disclination rings are equivalent to -1 point defects, topological charge of Torons in the uniform field is always conserved. The defects do not annihilate, but are rather stably unbound to enable the 3D twist within the structure. The 3D FCPM images and vertical cross-sections allow us to visualize and distinguish structural details of different Torons (Figs. 3.3, 3.4). For example, FCPM textures in Fig. 3.4 not

only identify the structures as T2, but also visualize the location of point and ring defects at the top or bottom glass plates.

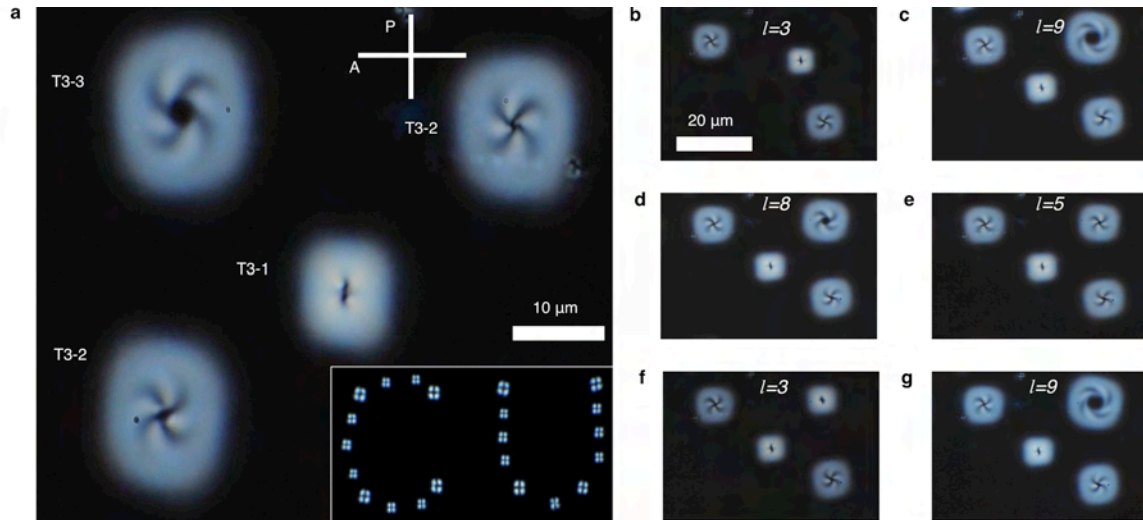


**Fig. 3.5.** Predetermined optical generation and switching of the Toron structures. (a) Polarizing optical microscopy texture showing T3-1 (the smallest), two T3-2s of opposite winding (intermediate size), and T3-3 (the largest structure) generated next to each other. The inset shows letters “CU” obtained by optical generation of four T3-2s per letter at the letters’ vertices and T3-1 elsewhere within the characters. Orientations of crossed polarizer (P) and analyzer (A) are shown by white bars. (b) Polarizing microscopy image showing that the two T3-2s of opposite spiraling and the T3-1 can be generated at arbitrary location in the sample and then moved to the desired position, such as the one shown in (c), using optical manipulation by laterally shifting the generating infrared laser beam. (c) After optically moving the T3-1 to the image center, the new T3-3 structure is generated in the top right corner of the image; this T3-3 structure is then transformed into a T3-2 structures as shown in (d,e) then to T3-1 shown in (f), and again to the T3-3 configuration shown in (g) by using LG beams of appropriate topological charge values  $l$  marked on the images. Note that the T3-3 structures in (c,d,g) have different diameters of the disclination rings at the top and bottom surfaces and all T3-2s and T3-3s have lateral dimensions 1.1-1.5 times larger than T3-1s.

By varying  $l$  of the generating vortex beams, we can selectively create (Fig. 3.5a) and switch (Fig. 3.5b-g) the Toron configurations. For example, the letters “CU” in the inset of Fig. 3.5a are composed of T2s at the corners and T1s elsewhere within the characters. Generation of different types of Torons depends on the initial laser-

induced director tilt from the vertical alignment, which, in turn, depends on the intensity distributions shown in Fig. 3.1(g-j). Beams having large  $|l|$  with high-intensity lobes in the periphery and low-intensity center generate T2s or T3s whereas beams with small  $|l|$  generate T1s. For example, in a cell with  $p \approx d = 5 \mu\text{m}$ , the T1 structure is induced by the LG beams with  $l = \pm(0-4)$ , T2 is observed for  $l = \pm(4-8)$ , and T3 for  $|l| > 8$ . Therefore, Torons can be reversibly transformed between each other as shown in the top right corner of panels c-g of Fig. 3.5. The threshold generating laser powers are comparable for all T3s and vary from  $60 \text{ mW}$  for  $l=0$  to  $110 \text{ mW}$  for  $l=10$ . The threshold power increases with increasing the cell thickness and helical pitch ( $70 \text{ mW}$  for the  $l=0$  beam and a cell of  $p \approx d \approx 15 \mu\text{m}$ ) but is independent of the sign of  $l$  and the CNLC handedness. Torons can be switched between each other or transformed into a uniform unwound state by applying electric fields; however, the spontaneous transformation between these structures requires nucleation of additional defects defining energy barriers much larger than the thermal energy. Generation of Torons is possible as long as the condition  $p/d \approx 1$  is satisfied, while having no explicit dependence on  $d$  or  $p$  individually. We have used materials with both positive and negative low-frequency dielectric anisotropy  $\Delta\epsilon_{lf}$ . For positive  $\Delta\epsilon_{lf}$  (e.g., nematic host ZLI-3412), the Torons can be erased into uniform nematic-like state by applying voltage of  $\sim 10 \text{ V}$  at  $1 \text{ kHz}$ . In CNLCs with negative dielectric anisotropy (e.g., nematic host MLC-6609), the low-frequency electric field tends to reorient  $\mathbf{n}(\mathbf{r})$  perpendicular to the electric field lines and reduces the threshold laser power of the LG beam needed to generate Torons because the action of the electric field assists that of the optical field. The Torons

and their periodic arrays or other structural arrangements are stable over long time at no external fields, but can also be “erased” by applying a voltage pulse to transparent electrodes or “reshaped” by a laser beam.

### **3.4 Localized Excitations: Toron Cousin Structures**

In addition to Torons that relieve twist-frustration in surface confined CNLCs, there are multiple other localized Skyrmionic defect structures, which also achieve the same by being induced by means of an optical generating beam. Localized topological configurations, such as Skyrmions, baby-Skyrmions, and Merons, play an important role in practically all branches of physics, such as nuclear physics, condensed matter, astrophysics, and string theory. For example, since mid nineties, Skyrmions have been found to play an important role not only in various aspects of particle physics and astrophysics but also in condensed matter systems such as chiral magnets.

The skyrmion concept is nowadays useful in describing dense hadronic matter relevant to compact stars and holographic baryons in the gravity-gauge duality. Describing nonsingular localized and topologically stable field configuration, Skyrmions and other localized topological configurations are typically characterized by a topological number, the so-called Skyrmion number, and cannot terminate in a uniform field without additional defects. Although they have been recently observed experimentally in chiral magnets and in cholesteric blue phases subjected to strong external fields, Skyrmions are still rather elusive objects. One of the reasons is the effect of surfaces and confinement, which typically perturb the skyrmionic textures

and make them energetically more costly, although may be required to obtain arrays of Skyrmions in certain conditions [Fukuda, Zumer Nature Comm]. It is therefore of great interest to explore how localized structures such as Skyrmions terminate at surfaces with different boundary conditions.

We generate various Skyrmionic textures using tightly focused laser beams and then explore how the ensuing axially symmetric director configurations vary across the sample thickness and at confining substrates. We demonstrate that both singular and nonsingular defect loops and point defects can arise as a result of confining skyrmion-like 2D textures into cells with strong surface boundary conditions and only weak perturbations to the texture exist in cells with weak surface anchoring. They are generated cells with homeotropic anchoring so that the chiral LC contained within is twist-frustrated. The thickness of the cell is approximately equal to the equilibrium helical pitch of the CNLC contained in it.

Having these similarities with conditions for generation of Torons, the important difference is the strength of surface anchoring on the substrates: Torons require strong homeotropic boundary conditions on both substrates, so as to support the existence of anchoring point defects or disclination rings in the bulk of liquid crystal. On the contrary, the structures shown in Figs. 3.6 – 3.10 have one salient feature differentiating them from Torons: the defects comprising these structures are pinned (or very close) to the surface. This requires a high cost in surface anchoring energy, and hence these structures are realizable only in presence of weak homeotropic boundary conditions. These structures are imaged in 3D using FCPM and from the vertical cross-sectional images, we deduce their structure and

present schematic representation of molecular director and the topology and composition of the constituent defects.

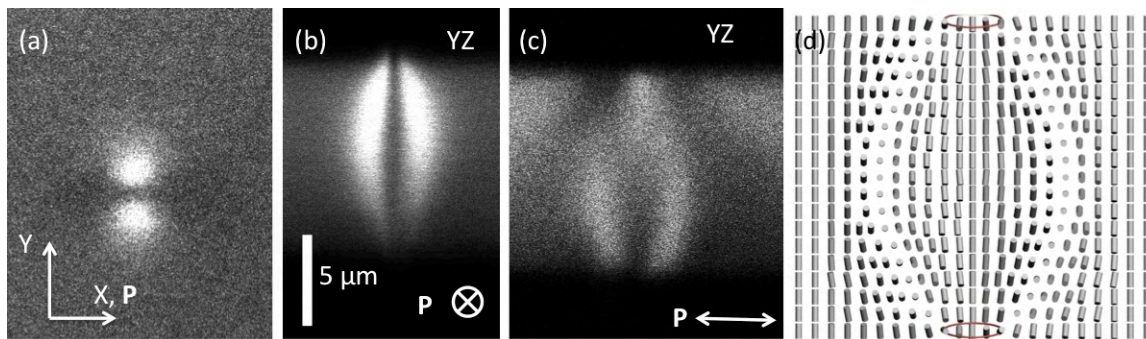


**Fig. 3.6.** Localized Excitation Type-I. (a) Structure imaged in its mid-plane. (b-c) vertical cross-sections obtained using FCPM in two orthogonal linear polarizations. (d) Schematic of molecular director reconstructed from the cross-sectional images. The twist-disclination loops are shown in red.

Structure shown in Fig. 3.6 is a localized excitation, which is terminated on two surfaces by very small loops of singular twist disclination lines, helping the twist-relieving structure to be compatible with the homeotropic anchoring at the substrates. The vertical extent of the structure is approximately  $p$ , while laterally it is much narrower and extends about  $p/2$ , as seen in the vertical cross-sectional images, Fig. 3.6(b,c). The schematic reconstruction of  $\mathbf{n}(\mathbf{r})$  in the vertical plane shows the location of twist disclinations in the structure (red circles). The director structure of a loop of a twist disclination close to a homeotropic surface is shown in Fig. 3.7(a). Twist disclinations are topologically different than the wedge disclinations (the  $\tau$  or  $\lambda$  kind), which we have encountered so far. The strength of the twist disclinations is equal in magnitude and opposite to each other, i.e., the

sense of angles is opposite,  $+\pi$  and  $-\pi$ , thus conserving the total topological charge in the structure, as seen in Fig. 3.7(b).

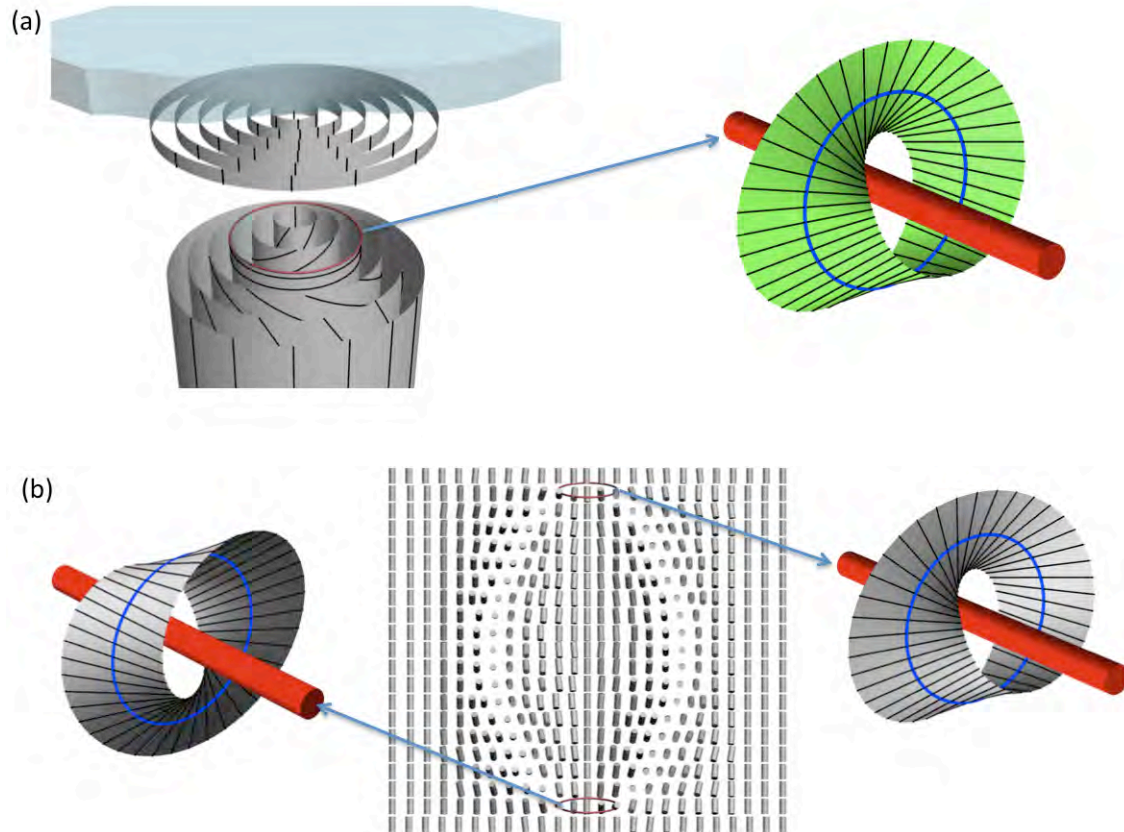


**Fig. 3.7.** Structure of the confining twist disclination loop. (a) The molecular arrangement within a loop of twist-disclination (in red) close to a homeotropic surface. (b) The twist-disclination loops of opposite strengths (opposite sense of twist angles) that confine the structure shown in Fig. 3.6.

We note that the strength of the disclination forming the loop is  $\pi$ , therefore the net strength of the loop thus formed is  $2\pi$ , which is the angle by which the director turns in the middle plane of the cell (going from homeotropic region in the left to that in the right). The structure can be generated optically with the help of an LG beam with  $l=\pm(0-4)$ , having optical power up to 100 mW focused at/close to the substrate. Focusing such a high intensity beam close/at the substrate would

compromise the surface anchoring and make it easier for defects to pin close to the surfaces. In Fig. 3.8, we see a related structure, with the difference that the twist disclination loop on one of the two binding surfaces has not contracted; seen in vertical cross-section Fig. 3.8(b) and schematic representation Fig. 3.8(c). Topologically though, it is similar to the structure shown in Fig. 3.6.

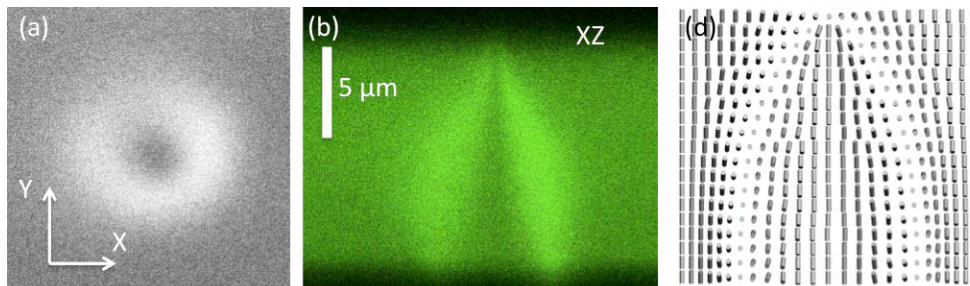


**Fig. 3.8.** Localized Excitation Type-II. This structure is similar to Type-I as revealed from its imaging in circular polarization. (a) The structure in its mid-plane. (b) vertical FCPM cross-section, and (c) molecular director pattern as deduced from the cross-sectional images.

In Fig. 3.9 we see a different kind of optically generated defect structure with an elaborate configuration of  $\mathbf{n}(\mathbf{r})$ . The structure has lateral expanse much larger than its vertical dimension. It is generated with the help of LG beams having high value of charge,  $|l| = \pm(12-20)$  and optical power of up to 100 mW. From the vertical cross-sections, Fig. 3.9(b,c), we reconstruct the  $\mathbf{n}(\mathbf{r})$  for this structure having axial symmetry, Fig. 3.10. It reveals two loops of nonsingular  $\lambda$  disclinations of opposite charge, situated in the bulk (loops of  $\lambda^{+1/2}$  and  $\lambda^{-1/2}$ ). The structure is anchored to the same substrate via two loops of singular twist disclinations (with opposite sense of angles), the inner one of which, in this case, has shrunk to a point defect. Thus the net strength of the inner loop is  $+2\pi$  and the outer loop is formed by a twist

disclination of angle  $-\pi$  (net angle of the loop,  $-2\pi$ ). The director turns by total of  $4\pi$  in the middle plane of the cell, as can be seen in Fig. 3.10. The presence of two oppositely charged non-singular and singular disclinations ensure that the global topological charge is conserved.

We find that the structures described above are related and can be understood in terms of linearly invariant defect structures found in similar cell geometries, viz., cholesteric fingers (see Appendix I for a brief overview of cholesteric fingers). We observe the similarity between the structure shown in Fig. 3.6 and type-three cholesteric finger, CF3. The CF3 has total twist of  $\pi$  in its mid-plane (and hence a very narrow structure) and is anchored with the help of twist disclinations on opposite surfaces. The structure in Fig 3.6 can be thought of as a loop of CF3. Similarly, we find that the structure shown in Fig. 3.9 can be likened to a loop of finger of the type CF4, with a combination of two twist disclinations on the same surface and two nonsingular  $\lambda$ -disclinations in the bulk.

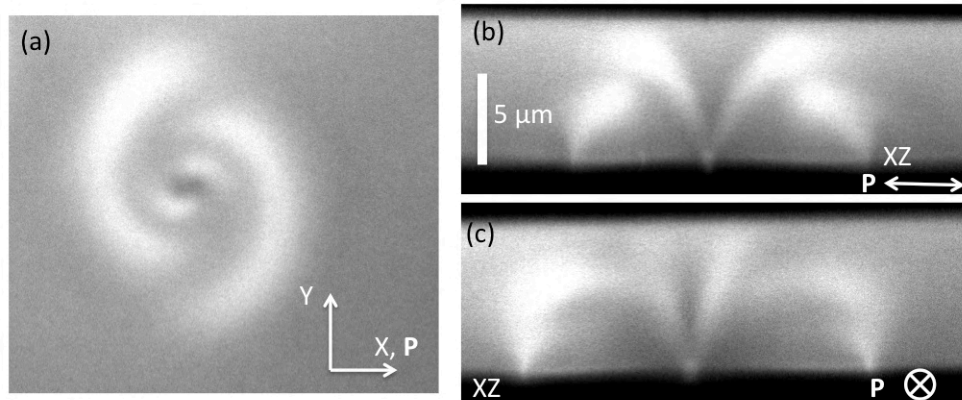


**Fig. 3.9.** Localized Excitation Type-III. The structure is imaged using FCPM in linear polarizations as marked, (a) in its mid-plane and, (b-c) vertical cross-sectional planes.

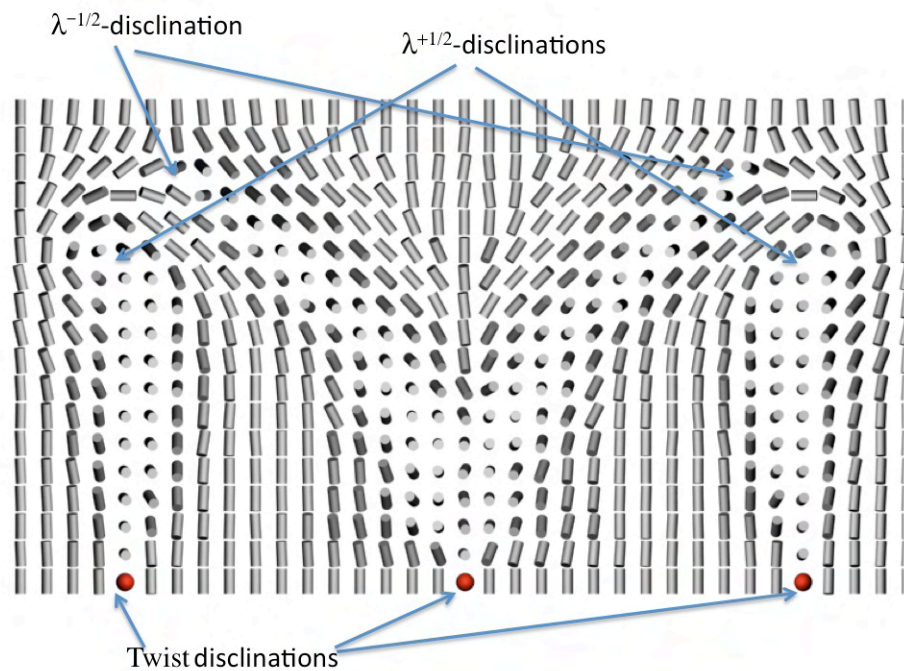


**Fig. 3.10.** Schematic representation of Type-III structure. The structure reveals an arrangement of two nonsingular ( $\lambda$ ) disclination loops in the bulk and two singular twist-disclination loops close to the same surface.

### 3.5 Summary

Robust generation of Torons at predetermined locations combined with both optical and electrical reversible switching can lead to new ways of multistable structuring of complex photonic architectures in soft materials. A wide variety of condensed phase phenomena arise as a result of the existence of particle-like excitations of continuous fields. Out of the three T3s observed in CNLCs with non-polar symmetry and the  $S^2/Z_2$  order parameter space, one (T3-1) can potentially be realized in polar condensed matter systems such as chiral magnets with the  $S^2$  order parameter space; this is in contrast to the T3-2s and T3-3s containing half-integer

disclinations that can not exist in a vector field. Therefore, in addition to their generation in frustrated chiral nematic systems, Torons can give origin to new forms of structural self-assembly in other chiral condensed matter phases, playing a role of “building blocks” similar to that of double twist cylinders in blue phases. The detailed knowledge of their structure may provide the basis for studies of complex twisted fields in condensed matter and impinge on understanding of particle-like excitations in other branches of science [98, 99].

The minimum size of the optically-induced Torons is not limited by the wavelength of generating light and is comparable to the cholesteric pitch  $p$ . When cholesteric pitch is smaller than the wavelength of generating light, by gradually tuning the laser power just above the Toron generation threshold, only one T3 structure can be induced at the center of the beam. This diffraction-unlimited nature of the process allows optical generation of Torons down to  $\sim 100$  nm in size even when an infrared laser beam is used. Since arbitrary periodic configurations of T3s can be generated for Toron sizes and lattice periodicities ranging from  $\sim 100$  nm to  $100 \mu\text{m}$  or larger, potential applications include data storage devices, light- or voltage-controlled diffraction gratings, and all-optical information displays. Both optical and electrical multistable switching of T3s with low-intensity beams or low-voltage electric fields is especially attractive for these applications as it enables low power consumption and diversifies modes of operation for the ensuing technologies and devices. Although the values of optical anisotropy of thermotropic liquid crystals are typically smaller than 0.5, the refractive index contrast can be enhanced by doping them with nanoparticles [101], potentially enabling photonic crystal

applications. Furthermore, the elasticity mediated interactions between particles embedded in the liquid crystal host make it interesting, from both fundamental and applied standpoints, to explore how the presence of Torons in the host medium translates into the oriented self-organization of immersed inclusions depending on their shape, size, and chemical composition or surface treatment. Since CNLCs with the T3s assembled into various structures can be photo-polymerized or polymer-stabilized [102], the spectrum of potential applications may extend to polymer-stabilized diffraction gratings, flexible displays, electronic books, non-mechanical beam steering devices, etc.

In conclusion, robust optical generation of multistable triple twisted Toron structures demonstrates that optical phase singularities in laser beams can allow for the control of topological singularities in materials. It is of special interest to further explore how linked and knotted optical wave dislocations [103-104] could generate topological defects and structures in soft matter as well as how arrays and nodes of liquid crystal defects, in return, could allow for devising of novel light beams by controlling their optical phase singularities. Torons and their arrays with tunable periodicity and interactions may be used as model systems for probing many-body interactions and condensed matter phenomena, similar to the current use of colloids. The detailed 3D structure of Torons reported here may provide new insights into the toroidal DNA condensation and DNA arrangement in chromosomes [105]. Furthermore, facile generation and switching of Torons open up the possibilities for applications ranging from all-optical devices to novel multistable information displays.

### 3.6 Appendix I: Cholesteric Fingers

Cholesteric fingers are linearly invariant defect structures (solitons) in that can occur spontaneously or be induced optically in cells with homeotropic anchoring and thickness between  $0.5p$  and  $p$ . They are classified into four types, CF1 – CF4, depending on the type of constituent disclination lines. See for example [62,106,107] for analysis of their detailed structure and imaging.

I show below schematic representation of the underlying pattern of  $\mathbf{n}(\mathbf{r})$  for different types of fingers in their vertical cross-sections, Fig. 3.S1-3.S4, to further elucidate the director configuration in the solitonic structures described in Section 3.4.

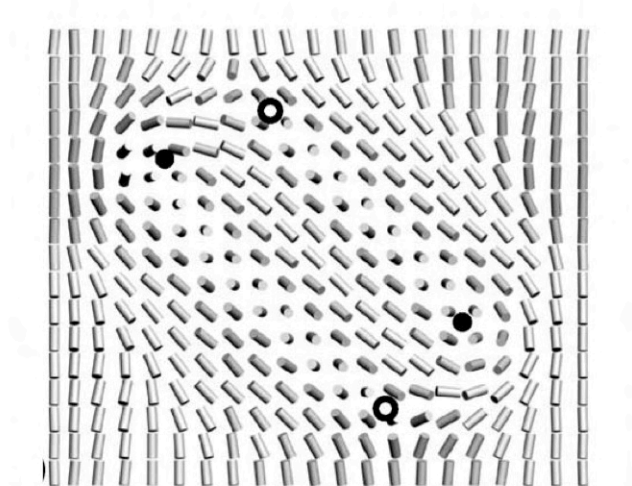


**Fig. 3.S1.** Cholesteric Finger CF1. The vertical cross-section shows two  $\lambda^{+1/2}$  (filled dots) and two  $\lambda^{-1/2}$  (hollow dots) nonsingular disclinations in the bulk that comprise the finger.

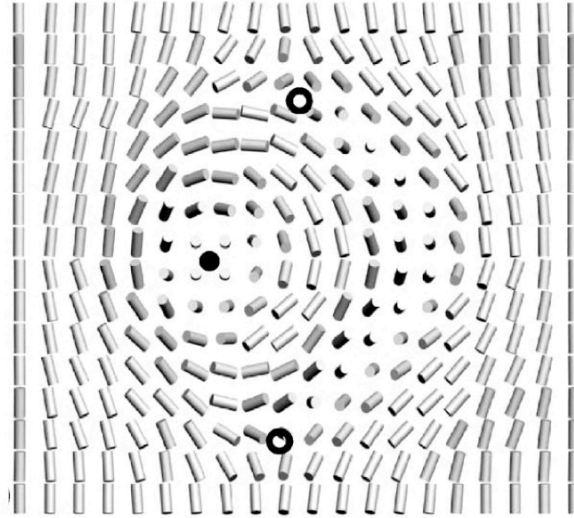


**Fig. 3.S2.** Cholesteric Finger CF2. The cross-section representation shows nonsingular  $\mathbf{n}(\mathbf{r})$  comprising one  $\lambda^{+1}$  (filled dot) and two  $\lambda^{-1/2}$  (hollow dots) disclination lines.

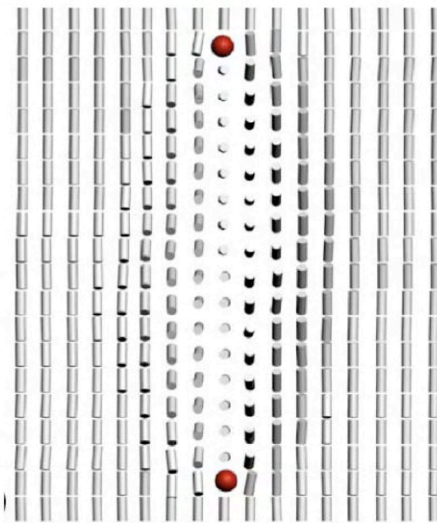


**Fig. 3.S3.** Cholesteric Finger CF3. The  $\mathbf{n}(\mathbf{r})$  in the vertical cross-section shows two singular twist-disclinations of strengths  $+\pi$  and  $-\pi$  close to the surfaces (red dots). This type of finger is much narrower than the others.

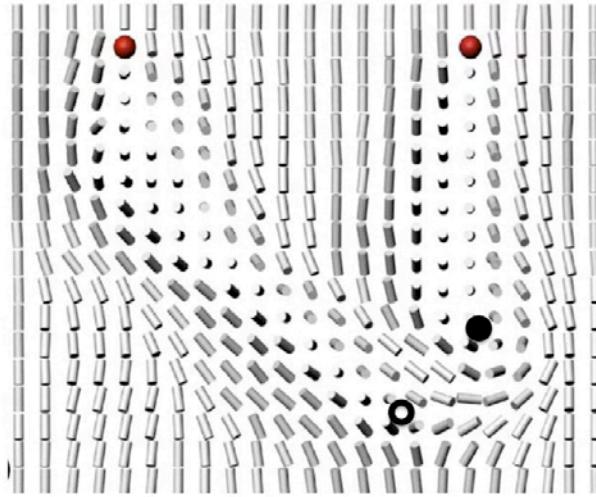


**Fig. 3.S4.** Cholesteric Finger CF4. The  $n(r)$  in the vertical cross-section of this type of finger is revealed to comprise two nonsingular disclinations:  $\lambda^{+1/2}$  (filled black dot) and  $\lambda^{-1/2}$  (hollow black dot) and two singular twist-disclinations of strength  $+\pi$  and  $-\pi$  (red dots).

## **Chapter 4**

# **Interactions and Patterning of Colloids and Defects in Cholesteric Liquid Crystals**

### **4.1 Introduction**

Colloidal systems find important applications ranging from fabrication of photonic crystals to direct probing of phenomena typically encountered in atomic crystals and glasses. New applications - such as nanoantennas, plasmonic sensors, and nanocircuits - pose a challenge of achieving sparse colloidal assemblies with tunable inter-particle separations that can be controlled. I demonstrate here reconfigurable multi-scale interactions and assembly of colloids mediated by defects in cholesteric liquid crystals that are probed by means of laser manipulation and three-dimensional imaging [108]. We find that colloids attract via distance-independent elastic interactions when pinned to the ends of cholesteric oily streaks, line defects at which one or more layers are interrupted., dislocations and oily streaks can also be optically manipulated to induce kinks, allowing one to lock them into the desired configurations that are stabilized by elastic energy barriers for structural transformation of the particle-connecting defects. Under the influence of elastic energy landscape due to these defects, sublamellar-sized colloids self-assemble into structures mimicking the cores of dislocations and oily streaks.

Interactions between these defect-embedded colloids can be varied from attractive to repulsive by optically introducing dislocation kinks. The reconfigurable nature of defect-particle interactions allows for patterning of defects by manipulation of colloids and, in turn, patterning of particles by these defects, thus achieving desired colloidal configurations on scales ranging from the size of defect core to the sample size. This defect-colloidal sculpturing may be extended to other lamellar media, providing the means for optically guided self-assembly of mesoscopic composites with pre-designed properties.

The fascinating richness of interactions involving colloids and defects in LC systems and their potential practical applications [45,46,110] require that these effects be explored on the level of individual particles and defects. Here, we probe defect-particle interactions and show that colloidal stabilization of defect structures can be extended to individual defect-particle level. Since the nature and strength of these interactions are defect-dependent, we use 3D optical imaging based on FCPM and 2PEF-PM to visualize the internal defect core structures and layer deformations. We optically generate various defects and alter their internal structure via non-contact manipulation with laser tweezers, and then quantitatively probe the ensuing particle-defect and particle-particle interactions. We demonstrate the feasibility of forming pre-designed stable 3D configurations of colloidal particles arranged along defects within cholesteric layers as well as along directions perpendicular to the layers. This may enable the physical “synthesis” of novel composites [110] having optically controlled properties, with patterned defect lines playing the role of artificial bonds between colloids and providing a framework for testing various

elastic theories [111]. We also demonstrate the ability to pattern sublamellar-sized particles within the defect cores, which is of great interest for nanophotonics applications.

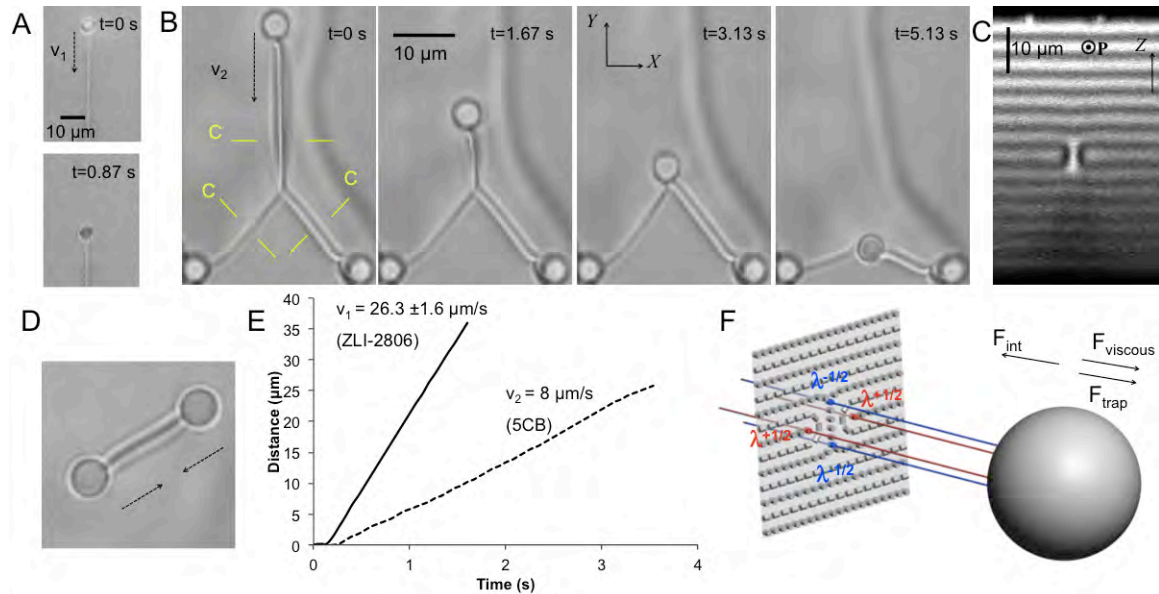


**Fig. 4.1.** Defect-particle interaction mediated by a Lehmann cluster. (A) A defect cluster in a cholesteric LC (ZLI-2806 and CB15) terminates at a particle and can be stretched by optically translating it but contracts once the colloid is released from the trap. (B) A Lehmann cluster in a cholesteric LC (5CB and CB15) is manipulated with the help of an optically trapped particle so as to form a node of clusters. Upon turning the trap off, the particle returns to its original position along the defect line between two stationary trapped colloids, as seen in the frames marked with elapsed time. (C) Vertical 2PEF-PM cross section of an elementary Lehmann cluster. (D) Lehmann cluster terminating on two particles. (E) Distance vs. time plot for the particle in (A) shown by solid line and for the particle in (B) shown by dashed line. (F) A schematic representation of an elementary Lehmann cluster terminating on a particle; the blue and red lines trace the  $\lambda^{-1/2}$  and  $\lambda^{+1/2}$  defects, respectively.

## 4.2 Defect-mediated Colloidal Interactions

Cholesteric LCs host a great variety of linear defects that are also encountered in other lamellar systems. The most abundant of these defects are dislocations and oily streaks that terminate or interrupt one or more layers. Elementary edge dislocations have Burgers vector  $|\mathbf{b}| = b/p/2$ . Their cores comprise

a dipole of  $\lambda$ - and  $\tau$ -disclinations of opposite half-integer strength. An elementary oily streak (also called “Lehmann cluster”) has the net Burgers vector equal to zero and is composed of a quadruple of nonsingular  $\lambda$ -disclinations, viz., two  $\lambda^{+1/2}$  and two  $\lambda^{-1/2}$  disclinations, Fig. 4.1. Unlike dislocations, Lehmann clusters can terminate on colloidal particles as they have the same number of cholesteric layers on opposite sides, and structure compatible with tangential surface anchoring conditions for  $\mathbf{n}(\mathbf{r})$  on the colloidal spheres such as the melamine resin polymer microparticles used in our study. The structures of defect-connected colloids like one shown in Fig. 4.1(A,B,D) can be found to occur spontaneously during defect coarsening upon quenching the LC cell from isotropic phase. These defect-particle configurations can also be generated using laser tweezers. These defects then mediate distance-independent attractive interaction between the particles, with the interaction force equal to the defect line tension (free energy per unit length), Fig. 4.1. We measure this force via optical manipulation of a particle attached to the tip of the line defect and tracking its motion, upon being released from the trap, and being dragged at a constant velocity  $v$ , Fig. 4.1E. Owing to relatively small  $v$  and high effective viscosity  $\eta$  of the LC (i.e., the Reynolds number is small), the inertial forces acting on the particle are negligible. The defect-mediated pair-interaction force  $F_{\text{int}}$  is balanced by the viscous drag that can be estimated using Stokes’ law, yielding  $F_{\text{int}} = F_{\text{viscous}} = 6\pi\eta Rv$ , where  $R$  is the particle radius. We use a value of viscosity coefficient that is the average of the measured values for directions parallel and perpendicular to the uniform  $\mathbf{n}(\mathbf{r})$ , obtaining  $\eta = 56.3$  mPa.s for 5CB-based cholesteric. Interactions due to defect lines of zero Burgers vector may involve

multiple mobile or stationary particles inter-connected by defects. For example, Fig. 4.1B shows a node of three Lehmann clusters, sustained with their ends pinned to particles. The particle released from a laser trap is dragged by the receding defect with the ensuing force equal to its line tension (Fig. 4.1E).

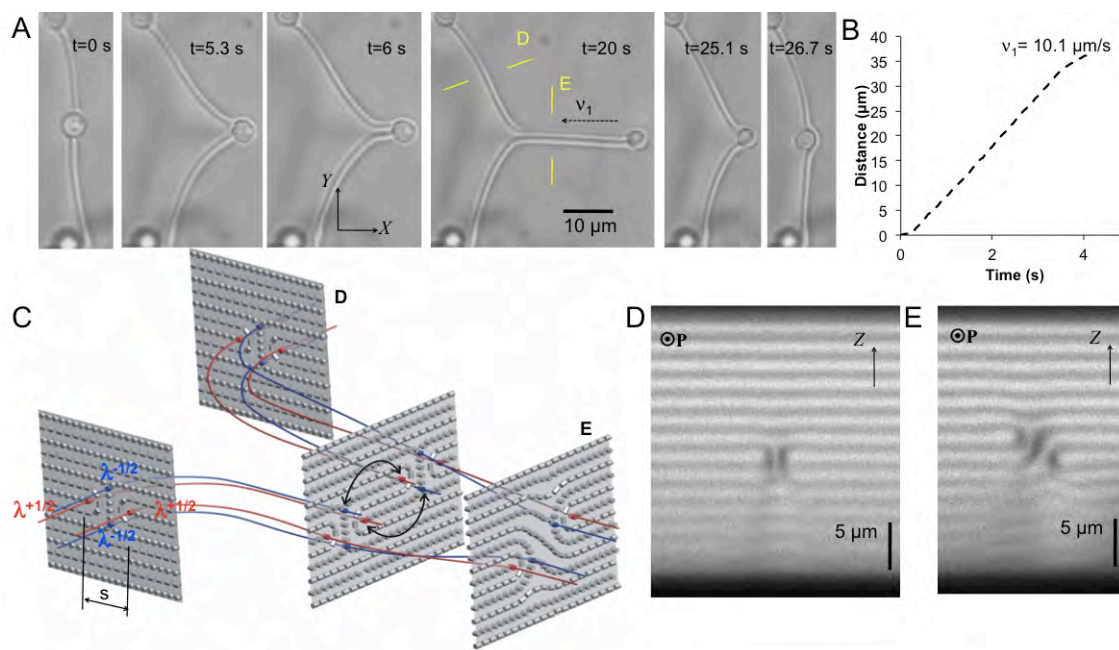


**Fig. 4.2.** Tensile defect-particle interactions mediated by various oily streaks. (A) An optically trapped particle, embedded in the core of an elementary Lehmann cluster, is used to transform the defect core structure. (B) Distance vs. time plot describing motion of the particle shown in (A) when released from the trap. (C) A schematic representation of the initial and the resultant defect core structures in their vertical cross-sections; the blue and red lines trace  $\lambda^{-1/2}$  and  $\lambda^{+1/2}$  disclinations in the defect cores, respectively. (D) FCPM vertical cross-sections of the Lehmann cluster and (E) the resultant oily streak having a modified core structure.

The strength of the distance-independent defect-mediated interactions depends on the core structure of oily streaks. For example, the fragments of optically manipulated Lehmann cluster shown in Fig. 2A turn by  $\pm 90^\circ$ , so that each part shifts vertically by a distance of  $\pm p/4$ , to conform to the cholesteric helix. The Lehmann cluster stretched thus metamorphoses into a defect with a different core

structure schematically shown in Fig. 4.2C, as reconstructed using FCPM vertical cross-sections (Fig. 4.2D,E). Although the ensuing elastic force acting on this defect-dragged microsphere is also distance-independent, its value is about 1.3-1.4 times larger. Fig. 4.S2 reveals that the strength of defect-mediated colloidal interactions increases with their width. For example, line tension values for the Lehmann cluster in 5CB-based cholesteric obtained by experimental methods range from 17 pN to 19.6 pN and the numerical estimate is 20.5 pN.

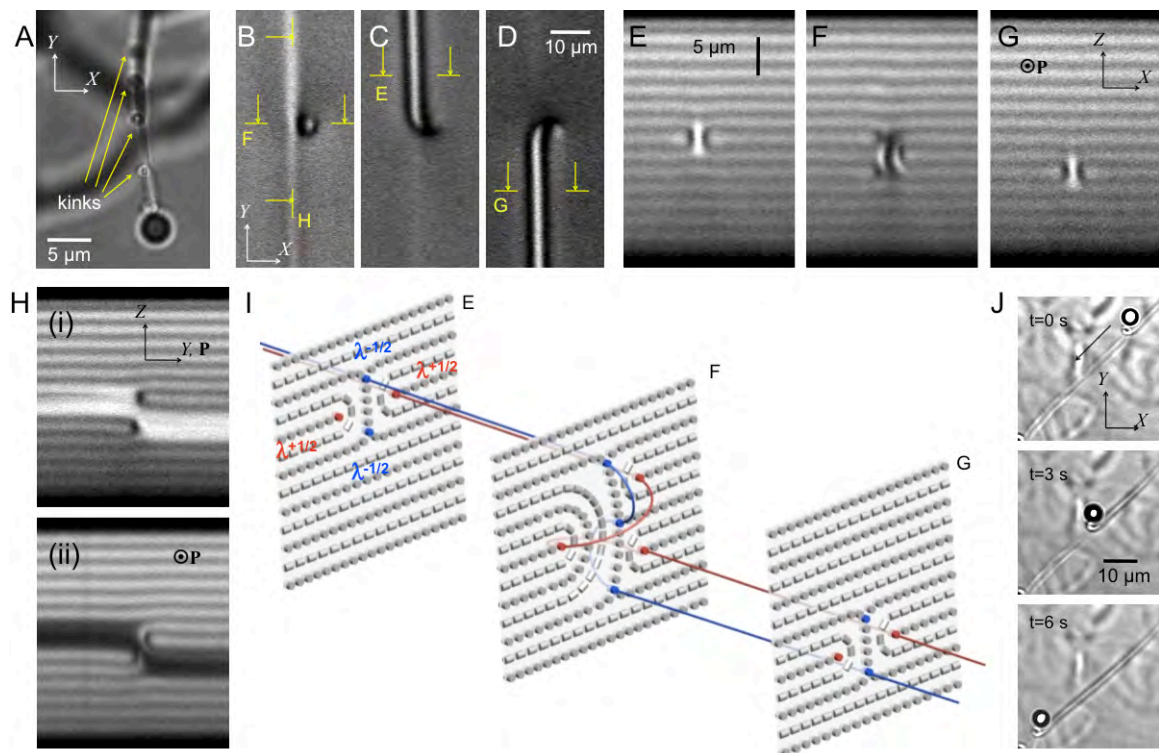


**Fig. 4.3.** Displacement of a Lehmann cluster across layers. (A) polarizing microscopy image showing how a Lehmann cluster terminating on an optically manipulated particle traverses layers via kinks in the form of windings. (B-D) In-plane 2PEF-PM images showing that the Lehmann cluster is at different depth across the layers on two sides of the kink. (E-G) Vertical 2PEF-PM cross-sections in the locations marked on the in-plane images (B-D). (H) Vertical 2PEF-PM cross-sections along the length of the defect for two orthogonal polarizations of the probing light. (I) A schematic of the reconstructed 3D director field and winding mechanism, with the vertical cross-section planes corresponding to cross-sectional images labeled alongside; the blue and red lines trace the  $\lambda^{-1/2}$  and  $\lambda^{+1/2}$  disclinations of the cluster, respectively. (J) The

position of kinks along the cluster's length can be displaced or locked with the help of a particle.

Lehmann clusters can also “glide” across the layers via “kinks” mediated by winding of the constituent  $\lambda^{+1/2}\lambda^{-1/2}$  disclinations (Fig. 4.3). Figure 4.3A shows a Lehmann cluster terminating on a particle and traversing across several layers via kinks such that each winding shifts the cluster across the layers by distance  $p$ . In-plane images shown in Fig. 3B-D and cross-sectional images in Fig. 3E-H, obtained in 2PEF-PM imaging mode, show the vertical displacement of the dislocation due to the kink with winding of  $\lambda$ -disclinations. The schematic diagram in Fig. 4.3I shows reconstructed  $\mathbf{n}(\mathbf{r})$  and traces the disclination lines  $\lambda^{+1/2}$  and  $\lambda^{-1/2}$  that preserve their nonsingular nature by conforming to the cholesteric helix while winding. Both the kink and the colloidal particle weakly pinned to it (with the binding energy  $\sim 20$ - $100k_B T$ ) can be optically translated along the length of the defect, Fig. 4.3J. Colloidal particles placed at the location of kinks and anti-kinks allow one to affix their positions and prevent their mutual annihilation, thus achieving controlled patterning of colloids and defects in 3D. This shows that the colloidal stabilization of defect structures in cholesteric LCs, originally demonstrated by Zapototsky et al., [45,46] can be extended down to the level of individual defects and particles. Our experiments indicate that morphing of defect structures between different states typically involves consecutive transformations that preserve the nonsingular nature of defect cores and/or involve low-energy structures that are not separated by elastic energy barriers. Colloids placed at the nodes and kinks hinder these defect

transformations by imposing strong energetic barriers  $\gg k_B T$  and entrap the system in long-lived metastable states.

### 4.3 Defect-arbitrated Colloidal Patterning

Elasticity-mediated interactions between defects and particles can be exploited for their 3D patterning. While large particles typically localize at defect nodes, colloids of size smaller than the layer thickness exhibit a wide variety of anisotropic interactions with defects and also with each other when confined in defect cores. To explore these interactions, we use melamine resin particles with  $R=1 \mu\text{m}$  and tangential boundary conditions for  $\mathbf{n}(\mathbf{r})$ , dispersed in a cholesteric LC with  $p=8 \mu\text{m}$ . These particles experience highly anisotropic interactions that drive them into well-defined positions within defect cores (Fig. 4.4) and yield binding potential of the order of  $1000k_B T$ . Depending on its initial location, each colloid can stably co-localize with any of the four  $\lambda$ -disclinations forming a Lehmann cluster, Fig. 4.4A-D. For example, the attraction of a particle towards the  $\lambda^{+1/2}$  disclination is within a range of  $\sim 4R$  (Fig. 4.4E), with the distance dependence of the interaction energy shown in Fig. 4.4F.

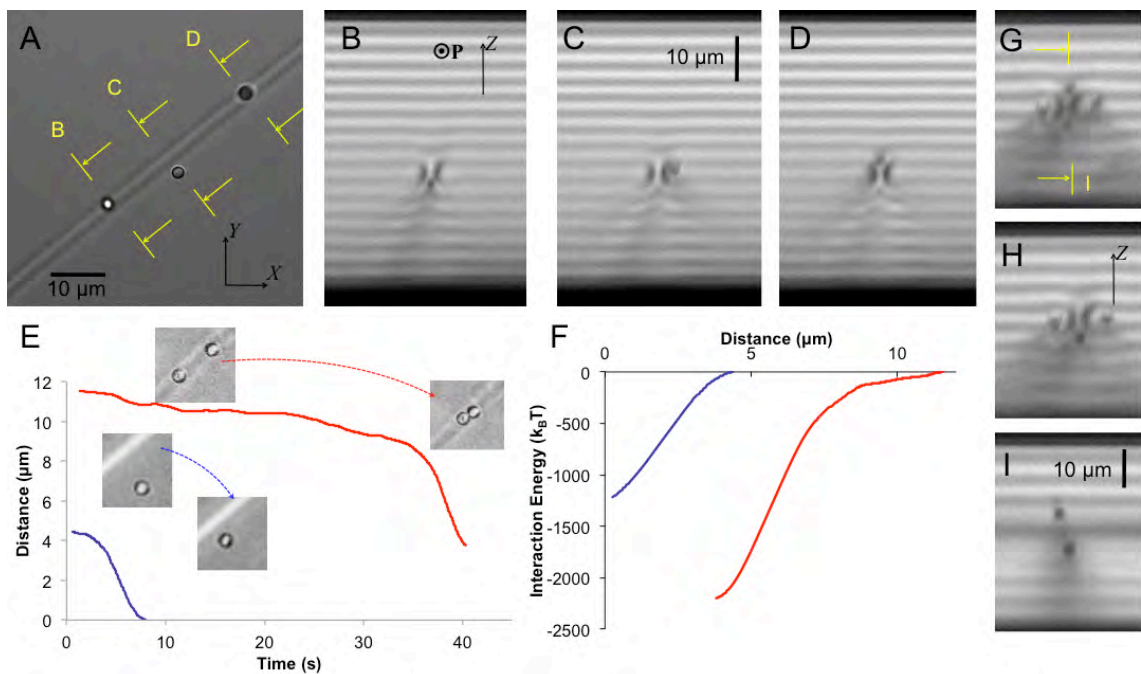


**Fig. 4.4.** 3D patterning of particles within a Lehmann cluster. (A) In-plane FCPM image showing particles embedded in a Lehmann cluster at different depths. (B-D) Vertical cross-sections showing particles localized inside the Lehmann cluster and centered at different  $\lambda^{+1/2}$  and  $\lambda^{-1/2}$  disclinations. (E) Distance vs. time plot for the motion of a particle perpendicular to the length of the cluster, as it is attracted towards the  $\lambda^{+1/2}$  disclination (blue curve; the particle initial position is within the same cholesteric layer as the  $\lambda^{+1/2}$  defect line). The red curve shows similar data for the motion of two attracting particles embedded in the same  $\lambda^{-1/2}$  disclination. The insets show initial and final particle positions for both cases. (F) Distance dependence of the interaction energy for particle-defect and particle-particle interactions. (G-I) Self-arrangement of colloids within a Lehmann cluster as seen in vertical cross sectional images perpendicular to (G,H) and along (I) the length of the defect.

Defects and the corresponding director distortions create an elastic potential landscape for the particles to interact while being localized within their cores. The interactions of particles centered on the same  $\lambda$ -disclinations of the core yield binding energies  $\sim 2000k_B T$ . The particles centered on different disclinations of dislocation or oily streak cores interact to localize roughly in the same plane orthogonal to the defect length (Fig. 4.4G-H and Fig. 4.5I-K). This can be exploited

for self-assembly of various colloidal structures replicating the defect core morphology, e.g. a diamond-like arrangement of four colloids centered on  $\lambda$  - disclination within the Lehmann cluster, Fig. 4.4(G-I). Interestingly, to further minimize elastic energy in this defect-bound colloidal configuration, particles centered at the two  $\lambda^{-1/2}$  disclinations get slightly displaced with respect to each other along the defect length (Fig. 4.4I), so that only three of the four particles are clearly visible in the cross-sectional images orthogonal to the defect line (Fig. 4.4G,H). Two particles embedded in the same  $\lambda$  disclination experience a relatively long-range (up to  $\approx 12R$ ) attractive interaction along the defect line (Fig. 4.4E,F).

Glide of dislocations across lamellae via kinks enables colloidal structuring in 3D (Fig. 4.5A-D). Although particles centered on the same disclination of an elementary edge dislocation core attract each other along its length (Fig. 4.5E,H), they repel from a kink and also from each other when separated by kinks. This behavior is different from the above-discussed attractive interaction between a similar colloid and a vertical winding kink in a Lehmann cluster with nonsingular defect structure (Fig. 4.3J). The kink in the edge dislocation has length and tilt with respect to lamellae that minimize the overall elastic energy cost of connecting edge dislocation fragments at different layers. When optically moved towards a kink, a particle alters its equilibrium structure, length, and tilt, and thus is repelled from it to minimize elastic energy. The magnitude of repulsive and attractive potentials is of the order of  $1000k_B T$  at short distances. Therefore, these interactions can be employed to selectively arrange colloids at different height across lamellae while being centered at the  $\tau \pm 1/2$  or  $\lambda \pm 1/2$  lines. For example, particles embedded in

the same elementary dislocation and separated by kinks form a sparsely spaced ladder-like structure shown in Fig. 4.5B-D. The sequence of vertical cross-sections (Fig. 4.5D) demonstrates how the  $b=p/2$  dislocation core alternates between that composed of  $\tau^{-1/2} \lambda^{+1/2}$  and  $\lambda^{-1/2} \tau^{+1/2}$  disclinations (Fig. 4.5F,G) and how particles find well-defined equilibrium positions while interacting with each other and kinks within the core.

Dislocations and oily streaks can be optically manipulated to induce kinks and thus generate a desired profile of elastic potential along their lengths, both within and across the layers. For example, the kink/anti-kink pair in the dislocation of Burgers vector  $b=p/2$  shown in Fig. 4.5A is generated using optical tweezers acting on a pinned particle as shown in Fig. 4.6. The axial optical trapping force needed to generate the kinks of  $b=p/2$  dislocation via pulling or pushing colloidal particles across the layers is of the order of 10-15 pN, in agreement with the estimates of the Peierls-Nabarro friction due to the transformation between  $\tau^{-1/2} \lambda^{+1/2}$  and  $\lambda^{-1/2} \tau^{+1/2}$  disclination pairs in the core. The kink can be optically translated along the defect length (Fig. 4.5A) and their position can be affixed by use of particles larger than the lamellar size, as discussed above. Thus, the linear defects can be directed along a desired 3D path within and across lamellae, giving rise to the desired landscape of interaction potential for patterning of sublamellar-sized particles.

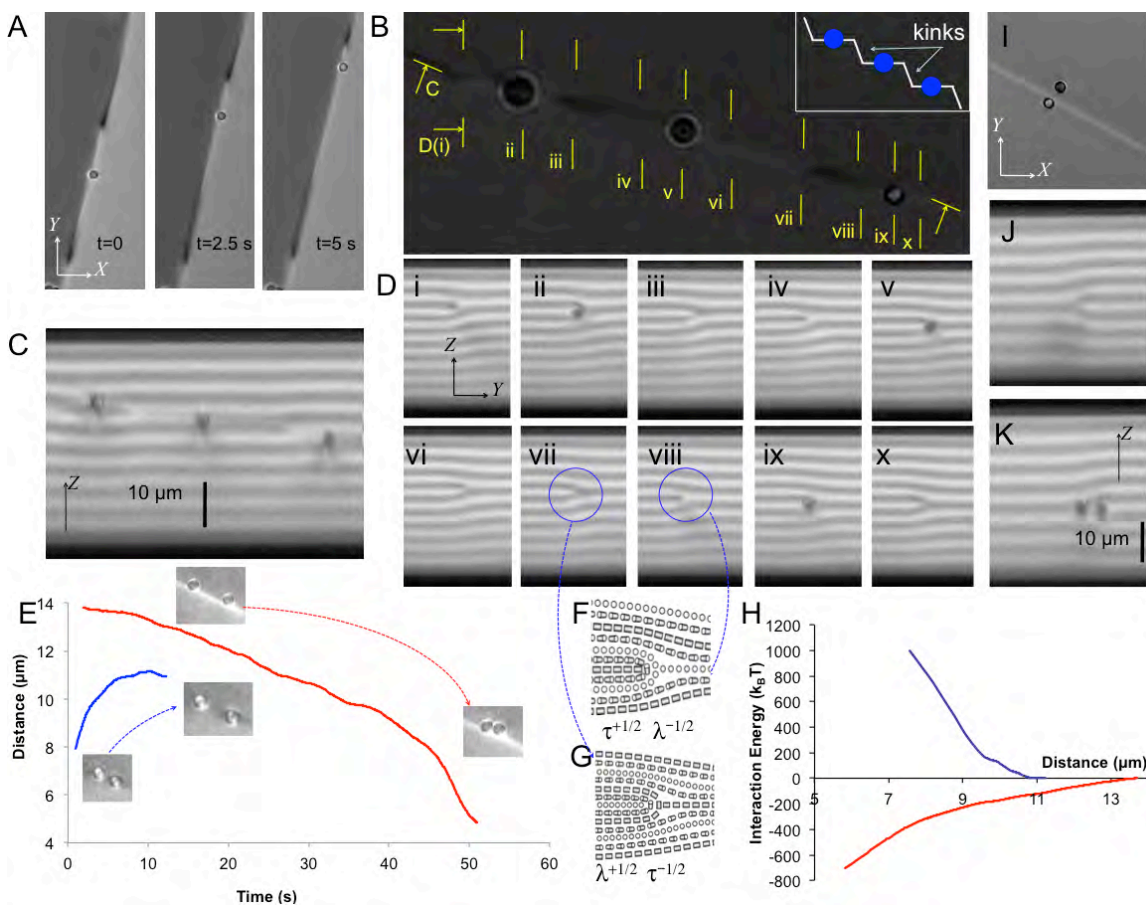


**Fig. 4.5.** 3D patterning of particles along edge dislocations with kinks. (A) Lateral manipulation of a kink in an edge dislocation using an optically trapped particle. (B) In-plane image showing particles embedded within an edge dislocation and separated by kinks; the inset schematically shows how colloidal particles localize on edge dislocations at different depths within the layered system while separated by kinks. (C) Vertical FCPM cross-section along the length of an edge dislocation. (D) A series of vertical FCPM cross-sections in planes perpendicular to the dislocation as marked in (B). (E) Distance vs. time plot describing the motion of interacting particles embedded into the dislocation: the particles repel from each other (blue curve) when separated by a kink but mutually attract (red curve) without kinks. The initial and final positions of the particles are shown in the insets for both cases. (F,G) Schematics of two alternating core structures of the  $b=p/2$  dislocation as it shifts vertically to form kinks. (H) The distance dependence of the interaction energy for both the repulsive (blue) and the attractive (red) inter-particle interactions within the edge dislocation without and with separating kinks, respectively. (I) planar and (J,K) vertical cross-sections of particles arranged in a dipolar fashion within the core of a  $b=p/2$  dislocation.

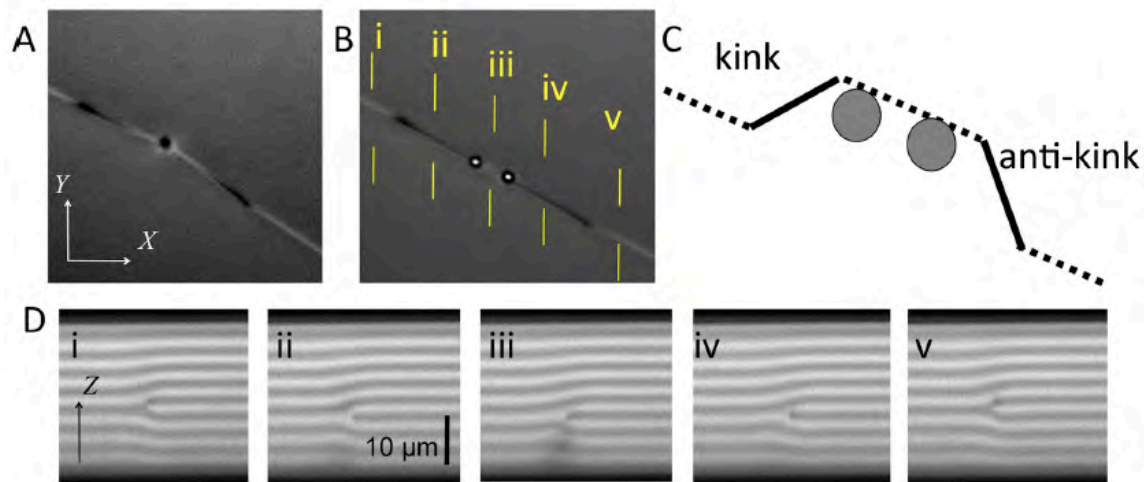


**Fig. 4.6.** Generation of kink/anti-kink pairs using optical tweezers. (A) A particle embedded inside the  $\tau^{+1/2}$  disclination of the dislocation is optically trapped. At high power, the axial laser trapping force acting on the particle pushes the dislocation to a different cholesteric layer. (B) Similar generation of the kink/anti-kink pair can be achieved with axial manipulation of two colloidal particles, which now allow one to control locations of the kink and anti-kink. (C) Schematic illustration showing the controlled generation of a kink/anti-kink pair by simultaneous axial translation of colloidal particles across lamellae. (D) Vertical 2PEF-PM cross-sections of the cholesteric layered sample in the vicinity of the generated kink/anti-kink pair, showing how the axial shift of the dislocation is accompanied by the transformation of dislocation cores.

#### 4.4 Summary

Most colloidal self-assembly approaches rely on the formation of close-packed crystal structures, taking advantage of typically short-range screened electrostatic and other interactions. We have demonstrated sparsely spaced controlled arrangements of colloids in cholesteric lamellae that utilize reconfigurable elastic interactions enriched by defects and stabilized by strong energetic barriers for transformation and annihilation of defects caused by presence of particles. The nature of interactions and the intra-defect assemblies are scale-invariant and hence can be controlled by changing the cholesteric pitch from about

50 nm to hundreds of microns. Since the defect structures and elasticity in other lamellar systems are similar to the ones studied here, our approach of using defects for sparse arrangement of colloids can be extended to other lamellar hosts such as diblock copolymers, DNA condensates, and various smectic LCs, as long as the energetic barriers due to the transformation of particle-stabilized defect structures can be kept  $\gg k_B T$ . Importantly, since the observed behavior of colloids in this system only depends on the boundary conditions for  $\mathbf{n}(\mathbf{r})$  at their surfaces, one can use particles of different material compositions, including metal plasmonic nanoparticles. Stable self-assembled arrangements of elastically-bound two, four, or more particles centered in disclinations of the cores of dislocation and oily streaks are thus of great interest for applications such as nanoantennas and optical field concentrators, especially since the inter-particle spacing can be varied from nanometers to microns. In addition to laser tweezers, the control of the 3D defect-particle architectures can be based on the application of electric fields, by using electrophoretic/dielectrophoretic forces applied to particles or through the modification of defect core structures due to direct coupling of  $\mathbf{n}(\mathbf{r})$  with applied fields; using LCs with positive or negative dielectric anisotropy further enriches the control capabilities. The latter approach offers tuning of line tension of linear defects like oily streaks (allowing one to even achieve negative tension values in materials with positive dielectric anisotropy), providing additional robust means for tuning interactions between particles at the ends of connecting defects or within the defect cores. Magnetic control can be efficient when using ferromagnetic or superparamagnetic colloids [109]. One can expect that observed interactions would

be highly dependent on the shape of used particles, possibly enabling selective shape-dependent localization of particles into different disclinations within the defect cores.

We have demonstrated 3D patterning of defect-colloidal networks in cholesteric lamellae by using optical generation and stabilization of desired defect structures by means of colloids. The stabilized defect networks, in turn, form a 3D elastic energy landscape capable of entrapping sublamellar-sized colloids. By introducing kinks in dislocations and oily streaks, interactions between these smaller colloids can be tuned from attractive to repulsive, offering powerful means to control sparsely spaced colloidal assemblies. Since both dielectric and metal particles can be used to form these defect-colloidal structures, potential applications include engineering of new materials, such as optical nanoantennas and metamaterials. Acting as elastic “bonds” connecting particles in long-lived metastable states, these highly controlled defect networks also offer the means to design elastic properties of new LC-colloidal composites [110].

#### 4.5 Appendix I: Analytical Estimates

The elastic free energy density for a lamellar medium can also be given in terms of the principal radii of curvature ( $R_1$  and  $R_2$ ) of the lamellar deformation and the dilation/compression of the layers as

$$F_{elastic} = \frac{K_1}{2} \left( \frac{1}{R_1} + \frac{1}{R_2} \right)^2 + \frac{1}{2} B \gamma^2 \dots\dots\dots(4.1)$$

The constant  $K_1$  (describing the splay of the  $\chi$ - director field) and the Young modulus  $B$  (describing the energy cost associated with dilation/compression of layers) are related to the Frank elastic constants of the liquid crystal as  $K_1=3K_{33}/8$  and  $B=K_{22}(2\pi/p)^2$ . Assuming that the layer spacing within and around the oily streak and dislocation defects remains intact, the line tension of these defects can be calculated as the lamellar curvature energy per unit length [31,40]:

$$T = \sum_{i=1}^m \frac{\pi K_1 (p/2)}{r_i} + \sum_{i=m+1}^{\infty} \frac{K_1 p}{r_i} \sin^{-1} \frac{s/2}{r_i} \dots\dots\dots(4.2)$$

,where  $r_i = (p/2) \cdot (i + 1/2)$  and  $s$  is the width of an oily streak defined as the distance between constituent  $\lambda^{+1/2}$ -disclinations. The analytical expression (4.2) is based on the assumption of equidistant layers and can be used only for rough estimates of tension. Indeed, a comparison of computer simulations and analytical estimates with Eq. (4.2) indicates that the core energy of oily streaks cannot be disregarded, even in the case when the core is composed of only nonsingular disclinations.

#### 4.6 Appendix II: Experimental Estimation of Defect Core Energy

The defect tension is experimentally measured using several different approaches, with the use of colloidal particles as “handles” and without them. We first need to calibrate the trapping gradient force at a particular value of optical power and at a certain depth (same as where the defect is located) in the LC cell. This is performed by first positioning the particle and trap at a distance of three to four times the particle diameter from each other. While the particle , under the influence of the trap, its motion is tracked by means of video microscopy. From this

we obtain velocity of the particle as a function of its distance from the center of the focus. The forces acting on the particle are obtained by using Stokes law. The magnitude of the gradient trapping force ( $F_{\text{trap}}$ ) is the maximum value the viscous force acting on the particle along its trajectory.

In the first method, using optical tweezers, a particle embedded within the defect is pulled orthogonally to the defect line, until a resultant defect is engendered. Upon releasing the particle from the trap, this newly created defect contracts, dragging the particle along with it (Fig. 4.1). The motion of the particle is recorded at the rate of 15 frames per second using a charge coupled device camera (640 X 480 pixels) and analyzed with particle tracking software (ImageJ or Tracker) to yield particle velocities and hence the tensile forces acting on the particles. An alternative approach involves manipulation of a defect line by pushing an optically trapped particle orthogonally to the length of the defect. At a fixed value of optical power, component of the tensile force of the defect will balance the trapping force up to a maximum bending angle, from which the value of tension can be obtained as,  $T = F_{\text{trap}}/2\cos(\theta)$  (Fig. 4.S1). We measured the tension of defects of different widths as shown in Fig. 4.S2. Since the wider defects are also more vertically spread, while the particle size is the same (4  $\mu\text{m}$ ), the value of tension obtained thus for defects with large  $s$  is typically an underestimation. To directly probe the colloidal pair interactions or defect-colloid interactions described in this work [109], the particles are first positioned at appropriate lateral distances and axial location in their initial configuration using optical tweezers. The laser traps are then switched off and we track the particle motion under the effect of interacting forces balanced by the

viscous drag force. Since both the particles are free to move, the interaction force on each particle is then equal to the defect line tension and calculated as  $F_{\text{int}} = \frac{1}{2} F_{\text{viscous}} = 3\pi\eta Rv$ .

**Table 4.S1**

Material Properties

Properties LC	$K_{11}$ , $pN$	$K_{22}$ , $pN$	$K_{33}$ , $pN$	$K$ , $pN$	$n_o$	$n_e$	$H_{HTP}$ of CB15, $\mu\text{m}^{-1}$	$\gamma_1$ , $\text{mPa}\cdot\text{s}$
5CB	6.4	3	10	$\approx 7$	1.536	1.714	+7.3*	$\approx 100$
ZLI-2806	14.9	7.9	15.4	$\approx 11$	1.475	1.518	+5.9*	$\approx 240$

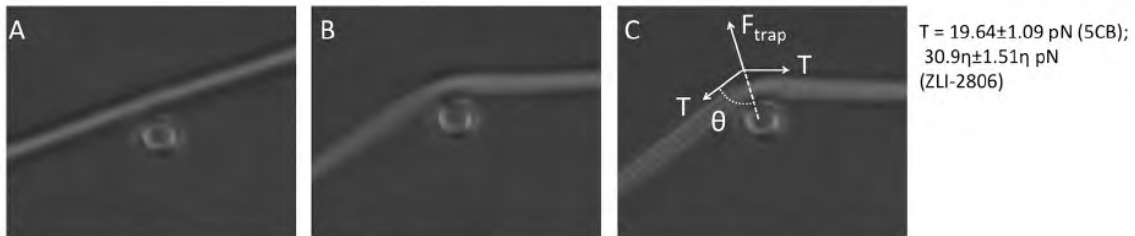


**Fig. 4.S1.** Measurement of tension of a Lehmann cluster by its manipulation using an optically trapped colloid. (A) The defect and the particle in the initial position. (B) The optically trapped particle is pushed against the defect until (C) the component of the line tension balances the laser trapping force, yielding the line tension of about  $T=19.64\text{pN}$ , determined using the maximum bending angle  $q$ . The measurement was done for 5CB- and ZLI-2806-based cholesteric LCs with  $5 \mu\text{m}$  pitch, where  $\eta$  is (unknown) viscosity of ZLI-2806 in  $\text{Pa}\cdot\text{s}$ .

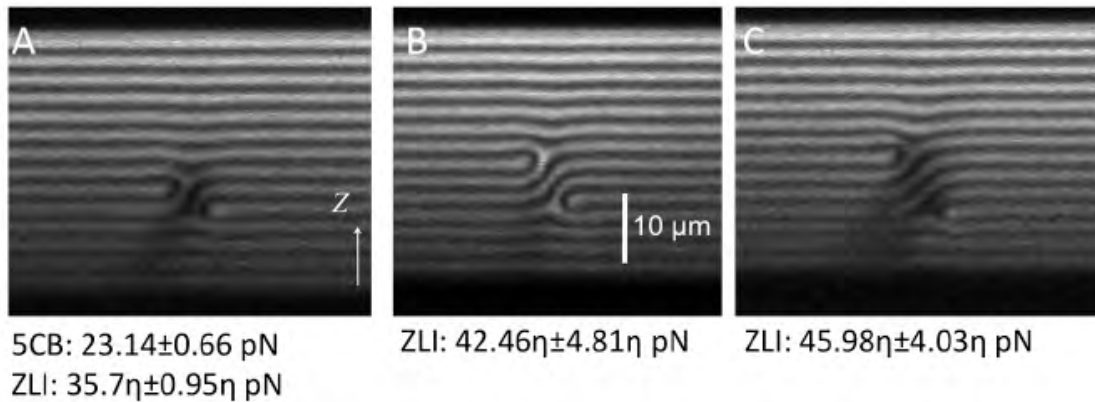


**Fig. 4.S2.** Tension of defects of different width for cholesteric liquid crystals based on 5CB and ZLI-2806. The cores of the defect are separated by  $s = 1.5p$  (A),  $2p$  (B), and  $2.5p$  (C), respectively. The values of tension are given in terms of the viscosity  $\eta$  of ZLI-2806 in Pa·s.

In addition to methods described above, which involve the use of optically trapped particles as handles, we also obtain the line tension values of defects by directly optically manipulating them with the laser tweezers. For this, we use a beam having power high enough for the electric field of the focused laser beam to reorient  $\mathbf{n}(\mathbf{r})$  within the focal volume. This region can then be trapped, since for the particular polarization of trapping beam, it has effective refractive index ( $\approx n_e$ ) higher than that of the surrounding LC and because of the involved attractive elastic forces between the defect and laser-induced distortion. This allows direct manipulation of the defect without using a particle. Upon turning off the trap, the extended defect structure shrinks (Figs. 4.S3 & 4.S4) and the tip of the defect is tracked to measure its rate of contraction. The rate of contraction in this case is much higher compared to the case when a particle is attached at the tip, since there is no viscous drag acting on a colloid in this case. This transformation of the defect involves a continuous transformation of the director structure at the defect tip. The

rate of contraction of the defect depends on its width  $s$ , the rotational viscosity coefficient ( $\gamma_1$ ), and the twist elastic constants ( $K_{22}$ ) of the LC, scaling as  $4K_{22}/s\gamma_1$  [14]. For example, using this rough analytical estimation, one obtains a value of the contraction rate of  $37.3 \mu\text{m/s}$  for a defect with  $s = 1.5\mu\text{m}$  in 5CB, which is consistent with the experimental value of  $39.9 \mu\text{m/s}$  (Fig. 4.S1). The value of tension obtained from the measured rate of contraction can be estimated as  $\sim(\pi/4)s \gamma_1 v$  and is approximately  $23.6 \text{ pN}$  for a defect with  $s=1.5$  in 5CB-based cholesteric LC, consistent with the values measured using the two different colloidal-particle-based methods of  $23.1 \pm 0.7 \text{ pN}$  (Fig. 4.S1A) and  $20.5 \text{ pN}$  (Fig. 4.2A).

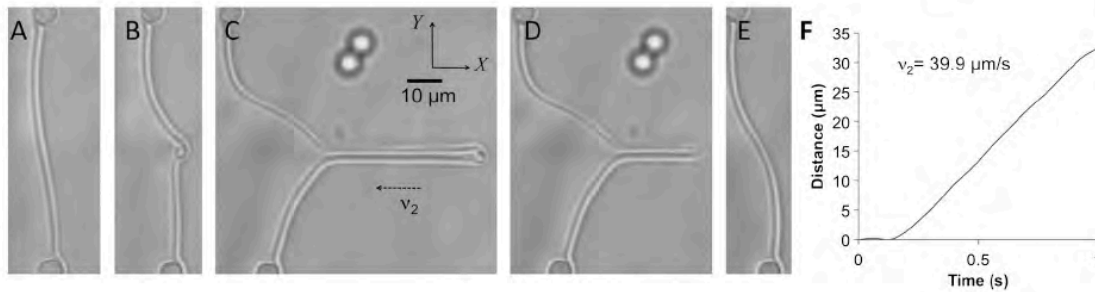


**Fig. 4.S3.** Measurement of defect line tension by means of its direct optical manipulation. (A-C) A defect structure is drawn out of a Lehmann cluster with the help of optical tweezers. (C-E) When the trap is released, the defect structure contracts to reduce its tensile free energy. (F) Videomicroscopy tracking of the tip of the contracting defect.

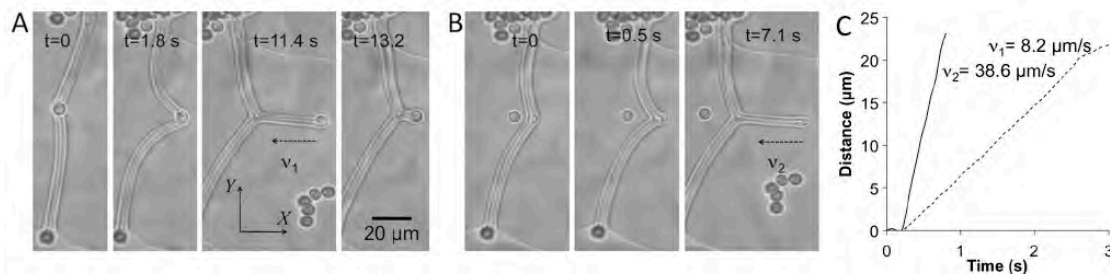


**Fig. 4.S4.** Measurement of line tension of a defect with multiple interrupted layers (large  $s$ ) by means of its manipulation using a particle as a “handle”. (A) A colloidal particle embedded inside an oily streak is manipulated to “draw” a new defect. Upon turning off the trap, the particle returns to its original position under the tension of the stretched defect line. (B) Similar manipulation without the help of a particle, (C) Videomicroscopy tracking of the tip of the contracting defect.

performed directly on the defect. (C) The rate of contraction of the defect vs. time in each case.

## Chapter 5

### 3D assembly of particles in Cholesteric Matrix

#### 5.1 Introduction

Introduction of foreign particles in nematic LCs leads to creation of defects in their vicinity such that the net topological charge of the system is conserved. The nature of defects and resultant symmetries in the molecular deformation field induced depend on the type/strength of surface anchoring [112,113,83] or the shapes of the particles [81]. For example, particles with strong homeotropic surface anchoring give rise to a -1 (hedgehog) point defect (imparting dipolar symmetry to the resultant director configuration) [112], while particles with weak homeotropic anchoring (or having size comparable to the cell thickness) give rise to a loop of  $-1/2$  disclination (also called a “Saturn-ring” defect) around them (resulting in an elastic quadrupolar symmetry) [113]. These defects supported by colloids and the resultant deformation in  $\mathbf{n}(\mathbf{r})$  provide new kinds of colloidal interactions in nematic LCs leading to one- and two-dimensional colloidal organization [114].

Colloidal interactions involving these effects have been studied in depth and well-understood for nematic LCs but the case of cholesteric LCs remains significantly unexplored. In the previous chapter, we explored one aspect of colloidal interactions in cholesterics LCs, viz., microscopic study of colloidal interactions and assembly mediated by defects that are inherently present in

cholesteric LCs. We intend to explore here another direction, i.e., study of interactions between colloids on account of defects and symmetries induced by their presence in cholesteric LCs. It can be heuristically argued that, because of breaking of chiral plane of symmetry and the layered structure of cholesteric LCs, they promise a richer topological landscape for formation of defects around colloidal particles and resultant interactions between them, as compared to the case of nematic LCs [53-55]. This scenario is further enriched by the observation that variation of the parameter  $d/p$  (ratio of diameter of the particle to the pitch of the cholesteric) can be exploited to “tune” the nature of defects and interactions. E.g., on one extreme, a particle with  $d \ll p$  will effectively “see” the cholesteric medium as “local nematic” LC and will produce similar defects/interactions.

Towards this goal of studying topology of the defect supported by an individual particle in cholesteric LC, there have been simulations [55]. Simulations have predicted existence of loops of  $-1/2$  disclinations that twist under the background twist in cholesteric LCs. There also have been some experiments involving particles with homeotropic anchoring dispersed in different cholesteric LC mixtures of varying pitch [54]. These have shown an interesting variety of twisted and linked loops of disclinations involving multiple particles. But these experiments have been confined to two-dimensional geometries (i.e., diameter of the particle  $\sim$  thickness of the cell).

As noted earlier, the case of  $d \ll p$  is essentially similar to a nematic colloid and thus a cholesteric with higher concentration of chiral dopant will result in more interesting behavior, which is what is the focus of exploration in this chapter (i.e.,  $d$

$\sim p$ ). The purpose of this exploration being 3D assembly, we employ appropriate particle and cell geometries. We first we note the nature of defect around a colloid under these conditions. Finally we study various kinds of interactions leading to 3D assemblies of colloids bound by elastic forces or defects.

## 5.2 Structure of Defects around Particles

As seen in the previous section, experiments conducted thus far have resulted in twisted Saturn-ring type of defects around particles (homeotropic anchoring) in cholesteric medium. This loop winding around the particle twists while doing so, due to the inherent helicity of the cholesteric. We study the defect structure in LC-particle system such that the particle diameter is comparable to (slightly less than) the cholesteric pitch, and this composite is confined within cells that are at least three times the particle diameter. For these system parameters, we report observation of point defect in the vicinity of particles giving rise to elastic dipoles. These “dipoles” are significantly modified by the chirality of the LC (since  $d \sim p$ ).

We experimentally confirm the existence of a point defect as shown in Fig. 5.1. To perform this, we use a high power optical trap to locally melt the cholesteric LC (12  $\mu\text{m}$  pitch) in a small region surrounding a particle (10  $\mu\text{m}$  diameter). Upon removal of the trap, the LC quenches to cholesteric phase and results first in a twisted loop. This loops relaxes over a period of 5-10 s to a point defect as seen in the sequence shown in Fig. 5.1(a,d). The resultant point defect can be seen in an image taken between crossed polarizers, Fig. 5.1(b,e), as well. The deformation of

$\mathbf{n}(\mathbf{r})$  in the vertical plane can be seen in vertical 3PEF cross-section, Fig. 5.1(c). The sequence in Figure 5.1(d) shows similar transformation of a twisted defect-loop to a point defect when a particle of same size is dispersed within LC of longer pitch ( $\sim 25 \mu\text{m}$ ).

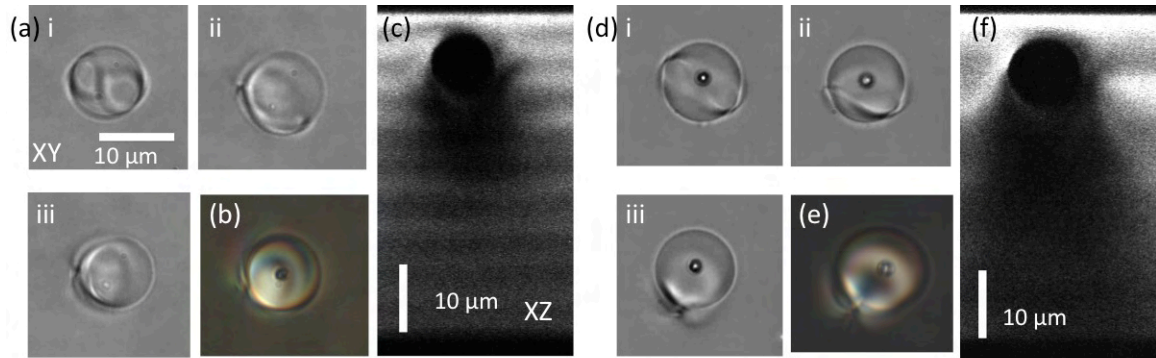


**Fig. 5.1.** Structure of defect around a colloid in cholesteric LC. (a) LC around a particle is locally melted using optical tweezers. Upon quenching, in a time-sequence of images, we see a twisted ring defect transform into a point defect for a 10- $\mu\text{m}$  diameter particle in 12- $\mu\text{m}$  pitch cholesteric LC. (b) The defect under crossed polarizers. (c) Layer distortion due to the particle in vertical cross-section using 3PEF. (d-f) Similar set of images for a particle 10  $\mu\text{m}$  in diameter, dispersed in a cholesteric LC with 25  $\mu\text{m}$  pitch.

The intriguing nature of the resulting “chiral dipole” in which one additional plane of symmetry (chiral) is broken (as compared to dipoles found in pure nematic LCs), can lead to a rich variety of colloidal interactions. We find that is indeed the case and provide a brief account of them in the next section.

### 5.3 Elastically- and Defect-bound assemblies

We observe colloidal interaction, which can be classified into two broad categories as those involving only elastic deformations and those involving disclination loops. Due to inversion symmetry of  $\mathbf{n}(\mathbf{r})$ , i.e.,  $\mathbf{n}(\mathbf{r}) \equiv -\mathbf{n}(\mathbf{r})$ , the in-plane

component of the elastic dipoles for particles confined within the same cholesteric layer can be either parallel or anti-parallel. We find that the nature of the interaction can be robustly controlled by selecting the interacting particles to have parallel or anti-parallel in-plane dipole moment. Each possibility of initial configuration leads to a different set of colloidal assembly having different geometry bound by different strengths of interaction. The final picture is rich with various controllable interactions, which can be combined to create complex 3D colloidal architectures.

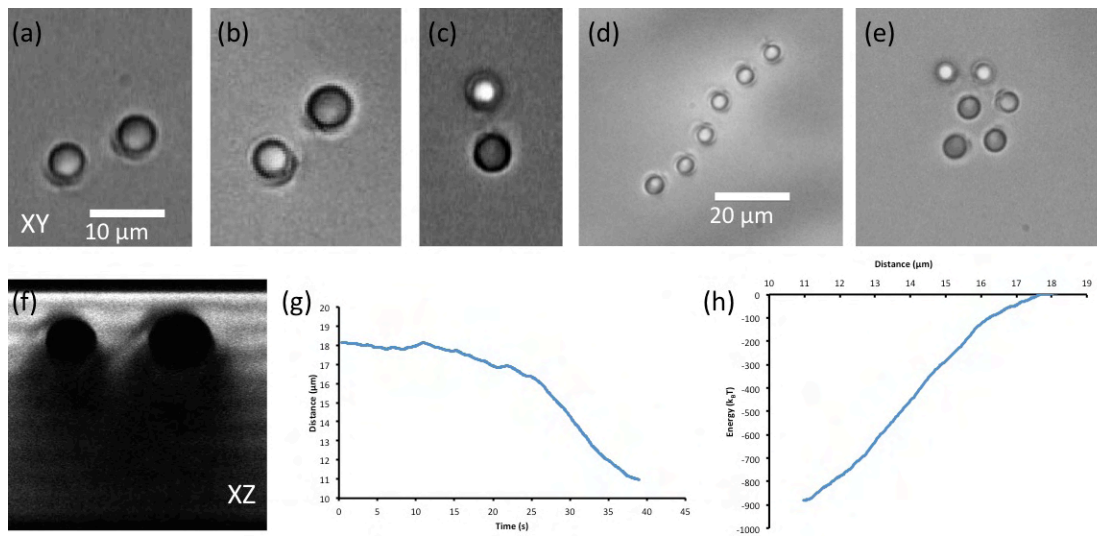


**Fig. 5.2.** Elastically bound particle assemblies. (a-c) Chiral dipolar particles form assemblies under attractive elastic interaction as shown. These assemblies are not only confined to the same cholesteric layer as in (a) but also formed when the particles are separated along the helical axis by  $\approx p/4$  (b) or  $\approx p/2$  (c). (d) An inplane assembly of multiple chiral dipolar particles, in the shape of a curved chain. (e) An assembly formed by several particles at different depths along the helical axis. (f) Interparticle separation as a function of time, as the particles are attracted towards each other to form the in-plane assembly in (a). (g) The interaction energy of the assembly in (a) as a function of interparticle separation.

We first explore elastic-only interactions between these chiral-dipolar colloids. As shown in three different scenarios in Fig. 5.2 (a-c), we have various possible end-configurations of colloids interacting in the same cholesteric layer or

separated by up to  $p/2$  along the helical axis. For this we have used  $4\ \mu\text{m}$  silica particles (treated to give homeotropic anchoring) in  $5\ \mu\text{m}$  pitch cholesteric LC. We note that for these elastically bound pairs of particles, the interparticle separation of the end configuration is  $\approx 2.75R$ , and it was experimentally observed that there is a strong repulsion in closer range than this. In-plane interaction results in a curved chain-like structure, i.e., the length of the chain and the direction of a participant dipole do not coincide, Fig. 5.2(a). We see the same structure in Fig. 5.2(f) in a cross-sectional images taken using 3PEF, showing the layer distortions. Figure 5.2(g) shows the interparticle distance as a function of time, as the particles placed apart attract each other. Fig.5.2(h) gives the interaction energy (in  $k_B T$ 's) of this pair as a function of their separation. We see that the magnitude of the interaction energy of the final configuration is about  $\sim 800k_B T$ , and hence it is thermally very stable. We also study the angular dependence of this elastic interaction between two particles confined within the same cholesteric layer, Fig. 5.3. From the plot of relative displacements, we see that the elastically bound pair is tilted with respect to each dipolar axis. Since the particle is free to move along the helical axis of the cholesteric (and thus rotate the direction of its dipole moment), most initial configurations result in an elastically stable assembly. There is indeed a weak repulsion at angular separation of  $0^\circ$ , but even in this case, due to perturbations in the initial conditions, we sometimes obtain elastically bound pair. At  $90^\circ$ , we obtain one of the two possible configurations shown in the inset, depending on the slight misalignment of dipole moments in the initial condition.

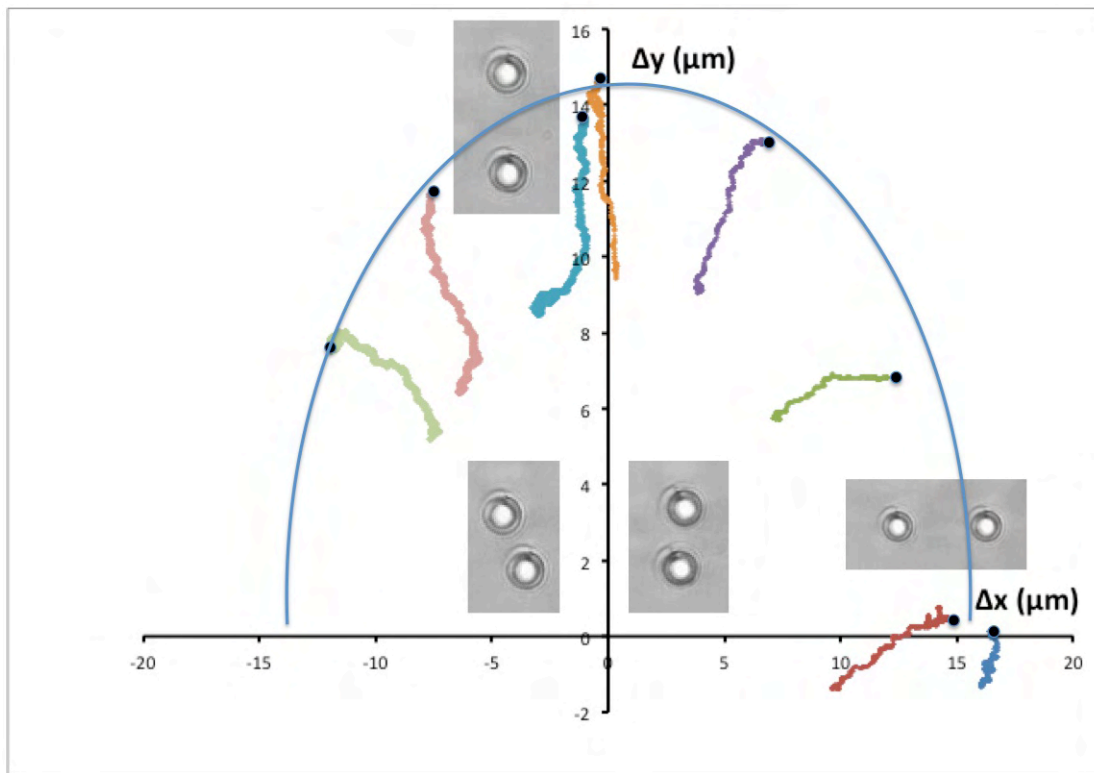


**Fig. 5.3.** Angular dependence of the elastic interaction. Interaction between two particles with parallel in-plane dipole moments is measured as a function of angular separation. The trajectories showing relative separation is displayed in different colors for different initial configuration. The initial positions are marked with a black dot.

In Fig. 5.2(b,c) we also see other two possible end-configurations elastically bound to each other but now the particles are displaced along the helical axis with respect to each other: by  $\sim p/4$  in Fig. 5.2(b) and  $\sim p/2$  in Fig. 5.2(c). In these cases, the strength of interaction is slightly less ( $600\text{-}800k_B T$ ). By controlling the vertical positions of the particles (and thus their initial conditions) we can make use of different kinds of elastic interactions to result in various colloidal assemblies as seen in Fig. 5.2(d,e). Figure 5.2(d) shows an in-plane structure akin to a curved chain formed by particles confined within the same cholesteric layer. In Fig. 5.2(e),

we see particles separated along the helical axis are elastically bound to each other, forming a stable assembly.

In addition to elastic interactions observed above, we find that the colloids interact with each other such that they result in an end-configuration bound by defect lines. The particles interact to result in an end-configuration bound by a disclination loop, when initially their in-plane dipole moments are anti-parallel. This is an interesting class of interactions that offers multiple arrangements for optically switchable 3D assembly. Some of these (two-dimensional) configurations share their structures with those observed earlier [54]. It is especially interesting in this case, as the original defect on the particle is point-like, which opens up to a loop when it is brought close to another particle, to connect both of them with a single loop of a line defect. Fig. 5.4(a) we see two particles bound by a loop of disclination, significantly displaced with respect to each other along the helical axis. The assembly is much more strongly bound (compared to the configurations we encountered earlier in Fig. 5.2), as seen in Fig. 5.4(e), giving interaction energy close to  $6,500k_B T$ . In Fig. 5.5, we see how the type of the defect configuration binding the particles can be robustly controlled by the initial separation of the particles, thus providing us with a control mechanism to optically guide the assembly process. Whether the particle associated defects are facing towards or away from each other, determines resultant interaction and selects the defect-bound configuration.

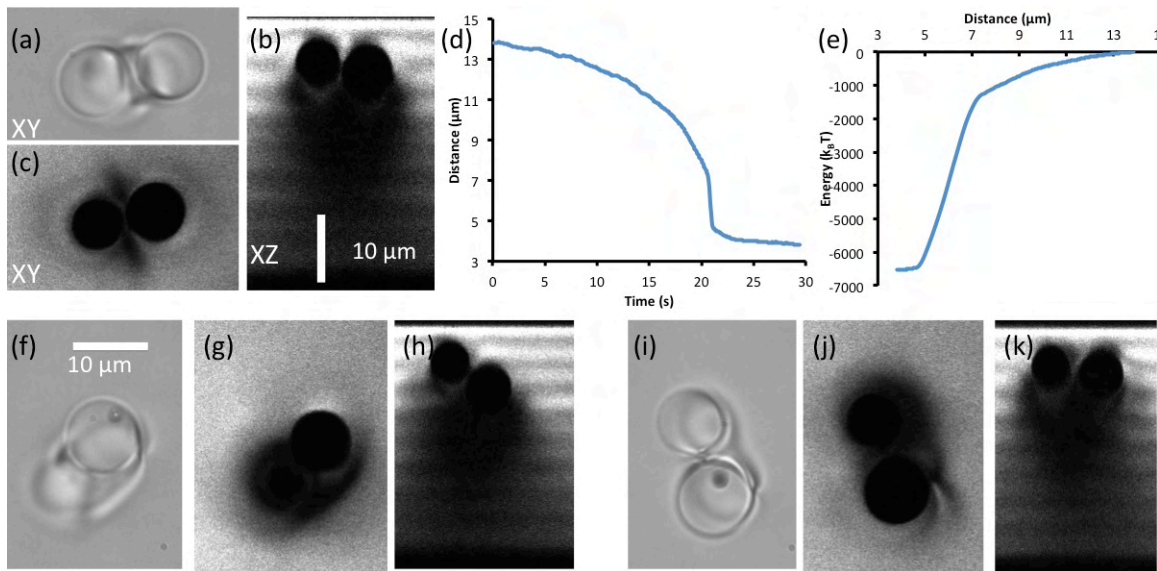


**Fig. 5.4.** Defect-bound particle assemblies. 10  $\mu\text{m}$  diameter particles in 12  $\mu\text{m}$  pitch cholesteric. We can optically form and switch between several types of in-plane or out-of-plane assemblies. (a,b,c) transmission micrograph, 3PEF in-plane section, and 3PEF vertical cross-section, respectively for one type of in-plane assembly. (f,g,h) similar set of images for out-of-plane defect-bound assembly. (i,j,k) Similar set of images for another type of in-plane assembly. (d) Interparticle separation vs. time during formation of assembly shown in (f). (e) Interaction energy vs. distance between particles as it forms assembly in (f).

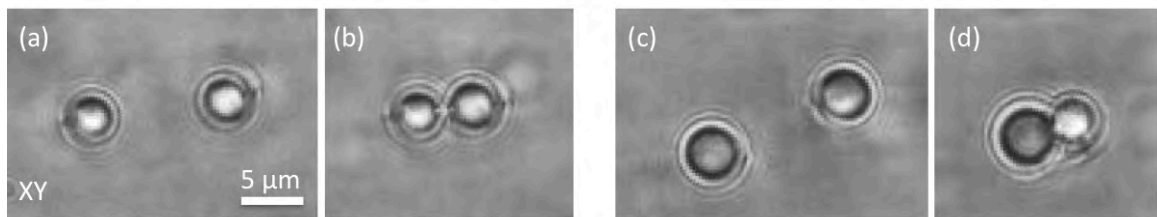


**Fig. 5.5.** Formation of defect-bound assemblies. The defect-bound assemblies are formed by a pair of particles with anti-parallel in-plane dipole moments. Depending on the mutual orientation of the dipoles, we end up with either an assembly confined within the same cholesteric layer (a,b), or one wherein particle are separated along the helical axis, (c,d).

Once this out-of-plane, two-particle assembly is formed, it can be optically manipulated to switch it into one of the other ones shown in Fig.5.4(f,g,h) and Fig.

5.4(i,j,k). Both of these configurations are confined to the same cholesteric layer but are formed as a result of completely different defect loop topology.

We see similar defect-bound configurations for the same size particles (10  $\mu\text{m}$  diameter) dispersed in a longer pitch cholesteric LC ( $\sim 25 \mu\text{m}$ ), Fig. 5.4. In this case though, we observe one more kind of assembly, which is reminiscent of a connected dipolar chain in nematic LCs, Fig. 5.6(e-h).

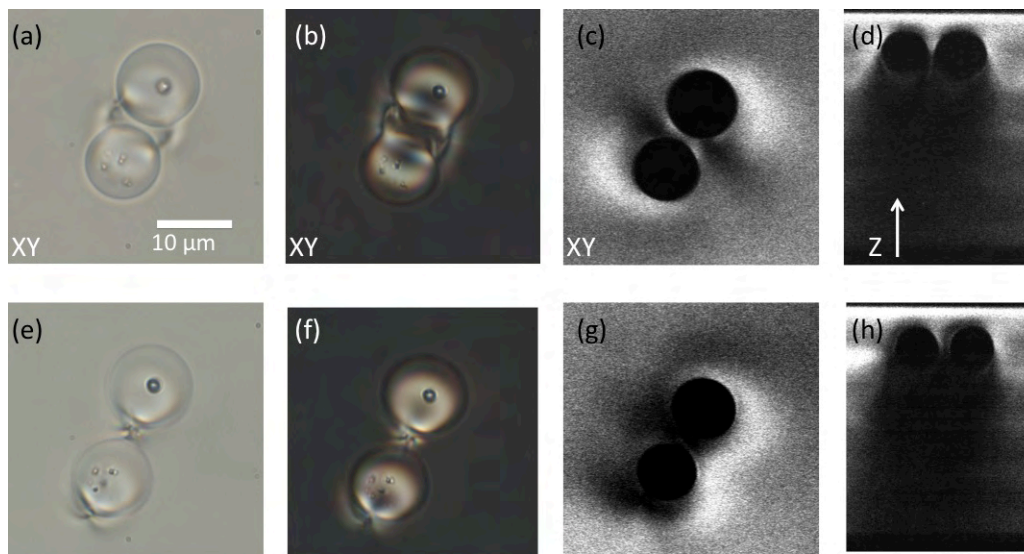


**Fig. 5.6.** Defect-bound particle assemblies of 10  $\mu\text{m}$  diameter particles in 25  $\mu\text{m}$  pitch cholesteric. (a-d) The in-plane assembly is depicted with the help of transmission micrograph (a), cross-polarized micrograph (b), 3PEF in-plane image (c), and 3PEF vertical cross-section (d). (e-h) Similar set of images for a different type of particle assembly. This configuration is similar to the chains formed by dipolar particles in nematic LCs.

We have thus seen multiple kinds of structures, which can be formed as a result of colloidal assemblies involving defect loops. These various two-particle assemblies (which can be formed within the same cholesteric layer, or across them) can be used as building blocks to form much larger colloidal assemblies, as demonstrated in Fig. 5.7.

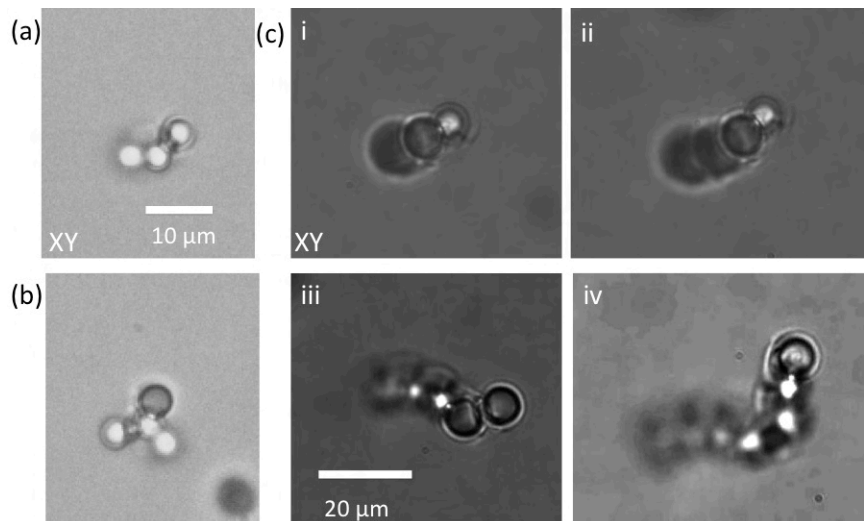


**Fig. 5.7.** 3D defect-bound multi-particle assemblies. 4  $\mu\text{m}$  diameter particles dispersed in 5  $\mu\text{m}$  pitch cholesteric. (a) Assemblies formed by three (a), and four particles (b). (c) A large 3D assembly formed of eight particles, created by bringing in one particle at a time, as shown with the help of selected frames at the end of different steps.

Figure 5.7(a,b) show three- and four-particle assemblies formed in 3D, utilizing different kinds of defect-coupled formations between the constituent particles. In Fig. 5.7(c), we see a sequence of images leading to formation of a large structure spanning  $\sim 10 \mu\text{m}$  along the helical axis and similarly in the lateral plane. The structure is formed by bringing in and “beading” one particle at a time.

#### 5.4 Summary

We have demonstrated here that the introduction of chirality to nematic LCs has a tremendous effect on the richness of resultant topological defect structures and consequent interactions between colloids. This can be exploited to form a complex variety of two- and three-dimensional assemblies of colloids with the help of very robust optical control and switching. The landscape for these interactions

can be expanded by varying the ratio of particle size to the pitch of the cholesteric LC; or by introducing particles with various shapes and surface anchoring. We can select from a variety of type of interactions observed, in-plane or out-of-plane interactions mediated by elastic deformations surrounding the particles (interaction energy few hundred  $k_B T$ ) or interactions that lead to defect-bound closely-packed assemblies (interaction energy few thousands of  $k_B T$ ). The type of desired assembly can be switched optically with the help of laser tweezers, as can the height of the interacting particles be adjusted. The type and strength of interactions, and the geometry of the particle-configurations formed can be varied by introducing colloids of multiple sizes in the same host cholesteric medium. Since the type (chiral dipole or twisted Saturn-ring) of defect around a particle depends on its size relative to the cholesteric pitch, we can generate a wide variety of structures by this means. Nanoparticles are observed to get elastically trapped inside the hedgehog point defect [115] in a nematic liquid crystal. The chiral dipolar particles and their assemblies can thus act as templates for 3D self-assembly of nanoparticles inside the matrix created by micron-sized colloids.

## Chapter 6

### Outlook and Conclusions

Towards the goal of achieving experimental capability of optically manipulating complex assemblies comprising defects and particles at microscale with an unprecedented control, and to visualize the associated molecular director patterns, we have developed an integrated optical system. We have designed and implemented system composed of 3D holographic optical manipulation and multimodal optical imaging of molecular director (in modalities such as confocal fluorescence, multi-photon fluorescence, multi-harmonic generation, CARS, etc.) and used it extensively to explore a vast number of LC based systems.

We have demonstrated the immense utility of optical manipulation in quantifying elasticity- and defect-mediated colloidal interactions in LCs [17-21]. Combining HOT with high-resolution 3D multi-particle tracking system with designed point spread function enables precise real-time 3D localization of the trapped colloids [47]. This would consequently help determine the map of interaction forces in 3D, in, e.g., self-assembly of many-particle system. HOT also allows for generation of beams with phase singularities (LG beams), which have proved to play an important role in precise control of LC defects [27]. Exploiting the full potential of the SLM in generating unconventional intensity profiles for the excitation beam, such as knotted and linked light beams [103,104] may enable

generation of analogous topological defect structures in LCs, highly interesting from both fundamental and technological point of view.

Integrating trapping with 3D orientational optical imaging techniques has been critical in revealing highly complicated director structures associated with multitude of defects encountered here and in visualizing colloids. The combined capabilities of multimodal 3D optical imaging, with non-contact 3D optical manipulation have facilitated design of novel composite soft-materials and chemical-sensitive characterization of the underlying self-organization processes. We have achieved this by implementing various imaging modalities. FCPM is successfully integrated with optical manipulation and used to image LC director patterns. Realizing that it requires doping LCs with specific dyes, which for some LC molecules (such as biaxial LCs) and composite systems is nearly impossible, we have implemented MNOPM. We have shown its capabilities in performing simultaneous multi-modal imaging of different constituents according to their chemical properties. Moreover, the PCF-based implementation for broadband CARS allows for micro-spectroscopy in a wide vibrational spectrum ( $800\text{-}3500\text{ cm}^{-1}$ ) and chemical bond-specific imaging by selecting appropriate chemical bonds of the constituent molecules. The imaging modalities can be further buttressed in several ways: with the help of a SLM in shaping the Stokes excitation spectrum to perform programmable CARS imaging of different vibrational modes simultaneously; by modifying the excitation system to include imaging modality such as Stimulated Raman Scattering (SRS) having much higher signal-to-noise ratio. Another major advantage of this integrated system lies in its ability to be extended to the study of

multitudes of other soft-matter systems involving nanoparticles, lipids, DNA and other biological materials-based LCs, polymer dispersed LCs, etc. This is because of the system's capability to robustly handle chemical complexity of biological systems as well as near-IR excitation (deeper penetration, lower absorption and hence lower thermal effects, etc.)

We demonstrate here robust optical generation of Torons with optical/electrical switching, which has great potential for setting the pathway to create soft-matter based structuring of multistable photonic structures. Understanding the structure of Torons has wide ranging implications: Skyrmionic excitations in chiral magnets, Understanding of elementary particles as Skyrmions in continuous nuclear field, etc. We observe that the size of Torons is not diffraction-limited as its generation is intensity-thresholded. This increases technological significance of Torons in potential applications such as all-optical devices, photonic architectures, optically tunable diffraction gratings, etc. Exploring their role in helping self-organization of immersed foreign inclusions (colloids, nanoparticles, etc.) may expand the range of their application in self-assembly of photonic crystals and probing many-body interactions. Photo-polymerizing or polymer-stabilizing arrays of Torons may lead to robust fabrication of polymer-stabilized diffraction gratings, flexible displays, etc.

We have explored at micro-scale and at individual defect-particle level, the interactions and assemblies of defects and colloids, that has resulted in novel colloidal architectures, hitherto not achieved. Most colloidal self-assembly approaches have relied on typically short-range screened electrostatic and other

interactions to form colloidal-crystals. We have demonstrated here formation of sparsely spaced controlled arrangements of colloids in cholesteric LCs that utilize elastic interactions mediated by defects. These assemblies are stabilized by strong energetic barriers ( $\gg k_B T$ ) for transformation and annihilation of defects caused by presence of particles. By introducing kinks in dislocations and oily streaks, interactions between colloids can be tuned from attractive to repulsive, offering powerful means to control sparsely spaced colloidal assemblies. Acting as elastic “bonds” connecting particles, these highly controlled defect networks also offer the means to design elastic properties of new LC-colloidal composites. The nature of interactions and the intra-defect assemblies are scale-invariant and hence can be controlled by changing the cholesteric pitch. Since the nature of defects and elasticity in other lamellar systems are similar to the ones studied here, our approach of using defects for sparse arrangement of colloids can be extended to other lamellar hosts such as diblock copolymers, DNA condensates, and various smectic LCs. Importantly, the behavior of colloids depends only on the boundary conditions for  $\mathbf{n}(\mathbf{r})$  at their surfaces, i.e., one can use particles of different material compositions (e.g., plasmonic nanoparticles). Stable self-assembled arrangements of elastically bound particles in the cores of dislocation and oily streaks are thus of great interest for photonic applications such as nano-antennas. Using LCs with positive or negative dielectric anisotropy further enriches the control capabilities, enabling tuning of line tension of linear defects (allowing one to even achieve negative tension values in materials with positive dielectric anisotropy). One can expect that observed interactions would be highly dependent on the shape of used

particles, potentially enabling selective shape-dependent localization of particles into different disclinations within the defect cores.

We then continue to explore the effects of chirality to nematic LCs on the nature of topological defects coupled to colloidal particles and consequent interactions between colloids. The vast richness of the defects/interactions found can be exploited to form a complex variety of two- and three-dimensional assemblies of colloids with the help of very robust optical control and switching. Studying these interactions allows us to expand their landscape by multiple means: by varying the ratio of particle size to the pitch of the cholesteric LC; by introducing particles with various shapes and surface anchoring; or by introducing colloids of multiple sizes in the same host cholesteric medium. The chiral dipolar particles and their assemblies can also act as elastic-potential templates for 3D self-assembly of nanoparticles inside the matrix created by micron-sized colloids. The nature of interactions can be selected/switched with the help of optical tweezers, between interactions mediated by elastic deformations surrounding the particles (interaction energy  $\sim 100k_B T$ ), or those leading to defect-bound closely-packed assemblies (interaction energy  $\sim 1000k_B T$ ).

## Bibliography

- [1] Chaikin P M, Lubensky T C. *Principles of Condensed Matter Physics*, Cambridge University Press, Cambridge, UK (1995)
- [2] de Gennes P-G, Prost J. *The Physics of Liquid Crystals*, Clarendon, Oxford, 2nd Ed. (1993)
- [3] Woltman S J, Jay D G, and Crawford G P. Liquid-crystal materials find a new order in biomedical applications. *Nature Mater.* **6**, 929-938 (2010)
- [4] H. Finkelmann, S. T. Kim, A. Muñoz, P. Palffy-Muhoray, and B. Taheri. Tunable mirrorless lasing in cholesteric liquid crystalline elastomers. *Advanced Mater.* **13**, 1069-1072 (2001)
- [5] Camacho-Lopez M, Finkelmann H, Palffy-Muhoray P, and Shelley M. Fast liquid-crystal elastomer swims into the dark. *Nature Mater.* **3**, 307-310 (2004)
- [6] Armitage D, Thackara J I, Clark N A, and Handschy M A. Ferroelectric liquid crystal spatial Light modulator. *Mol. Cryst. Liq. Cryst.* **144**, 309-316 (1987)
- [7] Clark N A, and Lagerwall S T. Submicrosecond bistable electro-optic switching in liquid crystals. *Appl. Phys. Lett.* **36**, 899-991 (1980)
- [8] Yang D K, Doane J W, Yaniv Z, and Glasser J. Cholesteric reflective display: Drive scheme and contrast. *Appl. Phys. Lett.* **64**, 1905-1907 (1994)

- [9] Kim, J -H, Yoneya M, and Yokoyama H. Tristable nematic liquid-crystal device using micropatterned surface alignment. *Nature* **420**, 159-162 (2002)
- [10] van Oosten C L, Baastiansen C W M, and Broer D J. Printed artificial cilia from liquid-crystal network actuators modularly driven by light. *Nature Mater.* **8** 677-682 (2009)
- [11] Yamamoto J, and Tanaka H. Dynamic control of the photonic smectic order of membranes. *Nature Mater.* **4**, 75-80 (2005)
- [12] Liu Q, Cui Y, Gardner D, Li X, He S, and Smalyukh I I. Self-alignment of plasmonic gold nanorods in reconfigurable anisotropic fluids for tunable bulk metamaterial applications. *Nano Lett.* **10**, 1347 (2010)
- [13] Pratibha R, Park W, and Smalyukh I I. Colloidal gold nanosphere dispersions in smectic liquid crystals and thin nanoparticle-decorated smectic films. *Jour. Appl. Phys.* **107**, 063511 (2010)
- [14] Pratibha R, Park W, and Smalyukh I I. Tunable optical metamaterial based on liquid crystal-gold nanosphere composite. *Opt. Express* **17**, 19459-19469 (2009)
- [15] Caillaud B, Dupont L, Gautier P, de Bougrenet de la Tocnaye J-L, Rudquist P, Engström D, Jägemalm P, and Lagerwall S T. A new application of ferroelectric liquid crystals: fast electrooptic helmet visors for pulsed welding applications. *Ferroelectrics* **364** pp. 66 – 71 (2008)
- [16] Engström D, O'Callaghan M J, Walker C, and Handschy M A. Fast beam steering with a ferroelectric-liquid-crystal optical phased array. *Applied Optics* **48** (9), 1721 – 1726 (2009)

- [17] Hällstig E, Öhgren J, Allard L, Sjöqvist L, Engström D, Hård S, Ågren D, Junique S, Wang Q, and Noharet B. Retrocommunication utilizing electroabsorption modulators and nonmechanical beam steering. *Optical Engineering* **44** (4), 45001 (2005)
- [18] Smalyukh I I, Butler J, Shrout J D, Parsek M R and Wong G C L. Elasticity-mediated nematic-like bacterial organization in model extracellular DNA matrix. *Phys. Rev. E* **78** 030701 (2008)
- [19] Brake J M, Daschner M K, Luk Y Y and Abbott N L. Biomolecular interactions at phospholipid-decorated surfaces of liquid crystals. *Science* **302**, 2094-2097 (2003)
- [20] Smalyukh I I, Zribi O V, Butler J C, Lavrentovich O D, and Wong G C L. Structure and dynamics of liquid crystalline pattern formation in drying droplets of DNA. *Phys. Rev. Lett.* **96**, 177801 (2006)
- [21] Hulmes D J. Building collagen molecules, fibrils, and suprafibrillar structures. *J. Structural Biology* **137**, 2-10 (2002)
- [22] Blanc N S, Senn A, Leforestier A, Livolant F and Dubochet J. DNA in human and stallion spermatozoa forms local hexagonal packing with twist and many defects. *J. Structural Biology* **134**, 76-81 (2001)
- [23] Livolant F. Ordered phases of DNA in vivo and in vitro. *Physica A* **176**, 117-137 (1991)
- [24] Nazzal S, Smalyukh I I, Lavrentovich O D and Khan M A. Preparation and in vitro characterization of a eutectic based semisolid self-nanoemulsified drug

- delivery system (SNEDDS) of ubiquinone: mechanism and progress of emulsion formation. *Intl. J. of Pharmaceutics* **235**, 247-265 (2002)
- [25] Zribi O, Kyung H, Golestanian R, Liverpool T and Wong G C L. Salt-induced condensation in actin-DNA mixtures. *Europhys. Lett.* **70**, 541-547 (2005)
- [26] Vollrath F and Knight D P. Liquid crystalline spinning of spider silk. *Nature* **410**, 541-548 (2001)
- [27] Sivakumar S, Wark K L, Gupta J K, Abbott N L & Caruso F. Liquid Crystal Emulsions as the Basis of Biological Sensors for the Optical Detection of Bacteria and Viruses. *Adv. Funct. Mater.* **19**, 2260 (2009)
- [28] Gupta V K, Skaife J J, Dubrovsky T B and Abbott N L. Optical Amplification of Ligand-Receptor Binding Using Liquid Crystals *Science* **279**, 2077 (1998)
- [29] Bowick M J, Chander L, Schiff E A, Srivastava A M. The cosmological Kibble mechanism in the laboratory: string formation in liquid crystals. *Science* **263**, 943 (1994)
- [30] Srivastava A M. String defects in condensed matter systems as optical fibers. *Phys Rev B* **50**, 5829 (1994)
- [31] Kleman M. *Points, Lines and Walls: In Liquid Crystals, Magnetic Systems and Various Ordered Media*. Wiley, New York. (1983)
- [32] Nelson D R. *Defects and Geometry in Condensed Matter Physics*. Cambridge University Press, Cambridge, UK. (2002)
- [33] Anderson V J, Lekkerkerker H N. Insights into phase transition kinetics from colloid science. *Nature* **416**, 811-815 (2002)

- [34] Schall P, Cohen I, Weitz D A, Spaepen F. Visualization of dislocation dynamics in colloidal crystals. *Science* **305**, 1944-1948 (2004)
- [35] Alsayed A M, Islam M F, Zhang J, Collings P J, Yodh A G. Premelting at defects within bulk colloidal crystals. *Science* **309**, 1207-1210 (2005)
- [36] Smalyukh I I, Lavrentovich O D. Three-dimensional director structure of defects in Grandjean-Cano wedges of cholesteric liquid crystals studied by fluorescence confocal polarizing microscopy. *Phys Rev E* **66**, 051703 (2002)
- [37] Lubensky T C. Hydrodynamics of cholesteric liquid crystals. *Phys Rev A* **6**, 452 (1972)
- [38] Lubensky T C. Low-temperature phase of infinite cholesterics. *Phys Rev Lett* **29**, 206 (1972)
- [39] Radzihovsky L, Lubensky T C. Nonlinear smectic elasticity of helical state in cholesteric liquid crystals and helimagnets. *Phys Rev E* **83**, 051701 (2011)
- [40] Iwashita Y, Tanaka H. Optical manipulation of defects in a lyotropic lamellar phase. *Phys Rev Lett* **90**, 045501 (2003)
- [41] Helfrich W. Lyotropic lamellar phases. *Jour Phys* **6**, A79 (1994)
- [42] Harrison C, Adamson D H, Cheng Z, Sebastian J M, Sethuraman S, Huse D A, Register R A, Chaikin P M. Mechanisms of ordering in striped patterns. *Science* **290**, 1558 (2000)
- [43] de Candia A, Del Gado E, Fierro A, Sator N, Tarzia M, Coniglio A. Columnar and lamellar phases in attractive colloidal systems. *Phys Rev E* **74**, 010403 (2006)

- [44] Seddon J M, Templer R H. *Polymorphism of Lipid-Water Systems, Handbook of Biological Physics: Structure and Dynamics of Membranes*, Ed: Lipowsky R, and Sackmann E. Elsevier SPC, Amsterdam (1995)
- [45] Zapotocky M, Ramos L, Poulin P, Lubensky T C, Weitz D A. Particle-stabilized defect gel in cholesteric liquid crystals. *Science* **283**, 209-212 (1999)
- [46] Ramos L, Zapotocky M, Lubensky T C, Weitz D A. Rheology of defect networks in cholesteric liquid crystals. *Phys Rev E* **66**, 031711 (2002)
- [47] Ravnik M, Alexander G P, Yeomans J M, Žumer S P. Three-dimensional colloidal crystals in liquid crystalline blue phases. *Proc Natl Acad Sci USA* **108**, 5188 (2011)
- [48] Engström D, Trivedi R P, Persson M, Bertness K A, Goksör M, Smalyukh I I. Three-dimensional imaging of liquid crystal structures and defects by means of holographic manipulation of colloidal nanowires with faceted sidewalls. *Soft Matter* **7**, 6304-6312 (2011)
- [49] Pires D, Fleury J-P, Galerne Y. Colloid particles in the interaction field of a disclination line in a nematic phase. *Phys Rev Lett* **98**, 247801 (2007)
- [50] Škarabot M, Ravnik M, Žumer S, Tkaleč U, Poberaj I, Babič D, Mušević I. Hierarchical self-assembly of nematic colloidal superstructures. *Phys Rev E* **77**, 061706 (2008)
- [51] Ravnik M, Alexander G P, Yeomans J M, Zumer S. Mesoscopic modeling of colloids in chiral nematics. *Faraday Discussions* **144**, 159-169 (2010)

- [52] Hijnen N, Wood T A, Wilson D, Clegg P S. Self-organization of particles with planar surface anchoring in a cholesteric liquid crystal. *Langmuir* **26**, 13502-13510 (2010)
- [53] Tkaleč U, Ravnik M, Čopar S, Žumer S, Muševič I. Reconfigurable knots and links in chiral nematic colloids. *Science* **33**, 62-65 (2011)
- [54] Jampani V S R, Škarabot M, Ravnik M, Čopar S, Žumer S, Muševič I. Colloidal entanglement in highly twisted chiral nematic colloids: Twisted loops, Hopf links, and trefoil knots. *Phys Rev E* **84**, 031703 (2011)
- [55] Lintuvuori J S, Stratford K, Cates M E, Marenduzzo D. Colloids in cholesterics: size-dependent defects and non-Stokesian microrheology. *Phys Rev Lett* **105**, 178302 (2010)
- [56] Ashkin, A. History of optical trapping and manipulation of small-neutral particle, atoms, and molecules. *IEEE Jour. Selected Top. Quant. Electr.* **6**, 841-856 (2000)
- [57] Grier D G. A revolution in optical manipulation. *Nature* **424**, 810–816 (2003)
- [58] Schutze K, Posl H and Lahr G. Laser micromanipulation systems as universal tools in cellular and molecular biology and in medicine. *Cell. and Mol. Biol.* **44**, 735 (1998)
- [59] Korda P T, Spalding G C and Grier D G. Evolution of a colloidal critical state in an optical pinning potential landscape. *Phys. Rev. B* **66**, 024504 (2002)
- [60] Curtis J E and Grier D G. Structure of Optical Vortices. *Phys. Rev. Lett.* **90**, 133901 (2003)

- [61] Smalyukh I I, Shiyanovskii S V, and Lavrentovich O D. Three-dimensional imaging of orientational order by fluorescence confocal polarizing microscopy. *Chem. Phys. Lett.* **336**, 88-96 (2001).
- [62] Smalyukh I I, and Lavrentovich O D. Three-dimensional director structures of defects in Grandjean-Cano wedges of cholesteric liquid crystals studied by fluorescence confocal polarizing microscopy," *Phys. Rev. E* **66**, 051703 (2002).
- [63] Smalyukh I I, et al. Electric-field-induced nematic-cholesteric transition and three-dimensional director structures in homeotropic cells. *Phys. Rev. E* **72**, 061707 (2005).
- [64] Higgins D A, and Luther B J. Watching molecules reorient in liquid crystal droplets with multiphoton-excited fluorescence microscopy. *J. Chem. Phys.* **119**, 3935 (2003).
- [65] Yoshiki K, Hashimoto M, and Araki T. Second-Harmonic-Generation Microscopy Using Excitation Beam with Controlled Polarization Pattern to Determine Three-Dimensional Molecular Orientation. *Japan. J. Appl. Phys.* **44** 1066-1068 (2005).
- [66] Pillai R S, Oh-e M, Yokoyama H, Brakenhoff C J, and Muller M. Imaging colloidal particle induced topological defects in a nematic liquid crystal using third harmonic generation microscopy. *Opt. Express* **14**, 12976-12983 (2006).
- [67] Chen B -C, and Lim S -H. Three-dimensional imaging of director field orientations in liquid crystals by polarized four-wave mixing microscopy. *Appl. Phys. Lett.* **94**, 171911 (2009).

- [68] Kachynski A V, Kuzmin A N, Prasad P N, and Smalyukh I I. Coherent anti-Stokes Raman scattering polarized microscopy of 3-D director structures in liquid crystals. *Appl. Phys. Lett.* **91**, 151905 (2007).
- [69] Kachynski A V, Kuzmin A N, Prasad P N, and Smalyukh I I. Realignment-enhanced coherent anti-Stokes Raman scattering and three-dimensional imaging in anisotropic fluids. *Optics Express* **16**, 10617-10632 (2008).
- [70] Saar B G, Park H -S, Xie X S, and Lavrentovich O D. Three-dimensional imaging of chemical bond orientation in liquid crystals by coherent anti-Stokes Raman scattering microscopy. *Opt. Express* **15**, 13585-13596 (2007).
- [71] Potma E O, Xie X S. Coherent Anti-Stokes Raman Scattering (CARS) Microscopy: Instrumentation and Applications" in *Handbook of Biomedical Nonlinear Optical Microscopy*, edited by Masters B R and Peter T. C. So (p164-186). Oxford University Press, New York, New York, (2008)
- [72] Anand S, Trivedi R P, Stockdale G, and Smalyukh I I. Non-contact optical control of multiple particles and defects using holographic optical trapping with phase-only liquid crystal spatial light modulator. *SPIE Proc.* **7232**, 723208 (2009)
- [73] Trivedi R P, Engstrom D, and Smalyukh I I. Optical manipulation of colloids and defect structures in anisotropic media. *Jour. Opt.* **13**, 044001 (2011)
- [74] Lee T, Trivedi R P, and Smalyukh I I. Multimodal nonlinear optical polarizing microscopy of long-range molecular order in liquid crystals. *Opt. Lett.* **35**, 3447-3449 (2010)

- [75] Trivedi R P, Lee T, Bertness K A, and Smalyukh I I. Three dimensional optical manipulation and structural imaging of soft materials by use of laser tweezers and multimodal nonlinear microscopy. *Opt. Exp.* **18**, 27658-27669 (2010)
- [76] Petit-Garrido N, Trivedi R P, Iñes-Mullol J, Claret J, Lapointe C, Sagues F, and Smalyukh I I. Healing of defects at the interface of nematic liquid crystals and structured Langmuir-Blodgett monolayers. *Phys. Rev. Lett.* **107**, 177801 (2011)
- [77] Engstrom D, Trivedi R P, Persson M, Bertness K A, Goksor M, and Smalyukh I I. Three-dimensional long-range order and defect core structures in anisotropic fluids probed by nanoparticles. *Soft Matter* **7**, 6304 (2011)
- [78] Engström D, Varney M C M, Persson M, Trivedi R P, Bertness K A, Goksör M, and Smalyukh I I. Unconventional structure-assisted optical manipulation of high-index nanowires in liquid crystals. *Opt. Exp.* **20**, 7741 (2012)
- [79] Yada M, Yamamoto J, and Yokoyama H. Direct observation of anisotropic interparticle forces in nematic colloids with optical tweezers. *Phys. Rev. Lett.* **92**, 18550 (2004).
- [80] Smalyukh I I, et al. Elasticity-mediated self-organization and colloidal interactions of solid spheres with tangential anchoring in a nematic liquid crystal. *Phys. Rev. Lett.* **95**, 157801 (2005).
- [81] Lapointe C, Mason T, and Smalyukh I I. Shape-controlled colloidal interactions in nematic liquid crystals. *Science* **326**, 1083-1086 (2009).

- [82] Škarabot M, et al. Laser trapping of low refractive index colloids in a nematic liquid crystal. *Phys. Rev. E* **73**, 021705 (2006).
- [83] Smalyukh I I, Kachynski A V, Kuzmin A N, and Prasad P N. Laser trapping in anisotropic fluids and polarization controlled particle dynamics. *Proc. Nat. Acad. Sci. U.S.A.* **103**, 18048-18053 (2006).
- [84] Smalyukh I I, Kuzmin A N, Kachynskii A V, Prasad P N, and Lavrentovich O D. Optical trapping of colloidal particles and measurement of the defect line tension and colloidal forces in a thermotropic nematic liquid crystal. *Appl. Phys. Lett.* **86**, 021913 (2005).
- [85] Smalyukh I I, Kaputa D S, Kachynski A V, Kuzmin A N, and Prasad P N. Optical trapping of director structures and defects in liquid crystals using laser tweezers. *Opt. Express* **15**, 4359 (2007).
- [86] Smalyukh I I, et al. Optical trapping, manipulation, and 3D imaging of disclinations in liquid crystals and measurement of their line tension. *Mol. Cryst. Liq. Cryst.* **450**, 79 (2006).
- [87] Murazawa N, Juodkazis S, and Misawa H. Laser manipulation based on a light-induced molecular reordering. *Opt. Express* **14**, 2481 (2006).
- [88] Brasselet E, Balcinuas T, Murazawa N, Juodkazis S, and Misawa H. Light-induced nonlinear rotations of nematic liquid crystal droplets trapped in laser tweezers. *Mol. Cryst. Liq. Cryst.* **512**, 143- 151(2009).
- [89] Gleeson H F, Wood T A, and Dickinson M. Laser manipulation in liquid crystals: an approach to microfluidics and micromachines. *Phil. Trans. R. Soc. A* **364** 2789-2805 (2006).

- [90] Conkey D B, Trivedi R P, Pavani S R P, Smalyukh I I, and Piestun R. Three-dimensional parallel particle manipulation and tracking by integrating holographic optical tweezers and engineered point spread functions. *Opt. Exp.* **19**, 3835-3842 (2011)
- [91] Shi K, Li P, and Liu Z. Broadband coherent anti-Stokes Raman scattering spectroscopy in supercontinuum optical trap. *Appl. Phys. Lett.* **90**, 141116 (2007).
- [92] Smalyukh I I, Pratibha R, Madhusudana N V, and Lavrentovich O D. Selective imaging of 3-D director fields and study of defects in biaxial smectic A liquid crystals. *Eur. Phys. J. E* **16**, 179-192 (2005).
- [93] Kano H, and Hamaguchi H. Femtosecond coherent anti-Stokes Raman scattering spectroscopy using supercontinuum generated from a photonic crystal fiber. *Appl. Phys. Lett.* **85**, 4298 (2004).
- [94] Cheng J X, and Xie X S. Coherent anti-Stokes Raman scattering microscopy: Instrumentation, Theory, and applications. *J. Phys. Chem B* **108**, 827-840 (2004).
- [95] Cizmar T, Mazilu M, and Dholakia K. In situ wavefront correction and its application to micromanipulation. *Nature Photon.* **4**, 388 (2010)
- [96] Voeltz G K, and Prinz W A. Sheets, ribbons and tubules — how organelles get their shape. *Nature Rev. Molec. Cell Biol.* **8**, 258-264 (2007).
- [97] Smalyukh I I, Lansac Y, Clark N A, and Trivedi R P. Three-dimensional structure and multistable optical switching of triple-twist particle-like excitations in anisotropic fluids. *Nature Mater.* **9**, 139-145 (2010)

- [98] Muhlbauer, S. et al. Skyrmion lattice in a chiral magnet. *Science* **323**, 915–919 (2009).
- [99] Fukuda J I, Zumer S. Quasi-two-dimensional Skyrmion lattices in a chiral nematic liquid crystal. *Nature Commun.* **2**, 246 (2011)
- [100] Dubois-Violette E. & Pansu B. Frustration and related topology of blue phases. *Mol. Cryst. Liq. Cryst.* **165**, 151–182 (1988).
- [101] Hung W.-C. et al. Surface plasmon enhanced diffraction in cholesteric liquid crystals. *Appl. Phys. Lett.* **90**, 183115 (2007).
- [102] Kang S -W and Chien L -C. Field-induced and polymer-stabilized two-dimensional cholesteric liquid crystal gratings. *Appl. Phys. Lett.* **90**, 221110 (2007).
- [103] Leach J, Dennis M R, Courtial J, and Padgett M J. Laser beams: Knotted threads of darkness. *Nature* **432**, 165 (2004).
- [104] Irvine W T M, and Bouwmeester D. Linked and knotted beams of light. *Nature Phys.* **4**, 716–720 (2008).
- [105] Kulic I M, Andrienko D, and Deserno M. Twist-bend instability for toroidal DNA condensates. *Europhys. Lett.* **67**, 418–424 (2004).
- [106] Oswald P, Baudry J & Pirkl S. Static and dynamic properties of cholesteric fingers in electric field. *Phys. Rep.* **337**, 67–96 (2000).
- [107] Oswald P, and Pieranski P. *Nematic and Cholesteric Liquid Crystals*. Taylor and Francis, Boca Raton, FL. (2005)

- [108] Trivedi R P, Klevets I I, Senyuk B I, Lee T, and Smalyukh I I. Multi-scale interactions and three-dimensional patterning of colloidal particles and defects in lamellar soft media. *Proc. Natl. Acad. Sci. USA* **109**, 4744 (2012)
- [109] Poulin P, Cabuil V, Weitz D A (1997) Direct measurement of colloidal forces in an anisotropic solvent. *Phys Rev Lett* **79**: 4862
- [110] Wood T A, Lintuvuori J S, Schofield A B, Marenduzzo D, Poon W C K. A self-quenched defect glass in a colloid-nematic liquid crystal composite. *Science* **334**, 79-83 (2011)
- [111] Osterman N, Kotar J, Terentjev E M, Cicuta P. Relaxation kinetics of stretched disclination lines in a nematic liquid crystal. *Phys Rev E* **81**: 061701 (2010)
- [112] Poulin P, Stark H, Lubensky T C, and Weitz D A. Novel colloidal interactions in anisotropic fluids. *Science* **275**, 1770 (1997)
- [113] Terentjev E M. Disclination loops, standing alone and around solid particles, in nematic liquid crystals. *Phys. Rev. E* **51**, 167 (1999)
- [114] Mušević I, Škarabot M, Tkaleč U, Ravnik M, and Žumer S. Two-dimensional nematic colloidal crystals self-assembled by topological defects. *Science* **313**, 954 (2006)
- [115] Senyuk et al. Shape-dependent oriented trapping and scaffolding of plasmonic nanoparticles by topological defects for self-assembly of colloidal dimers in liquid crystals. *Nano Lett.* **12**, 955 (2012)